Jordan Journal of
PHYSICS
An International Peer-Reviewed Research Journal

Volume 14, No. 3, September 2021, Safar 1443 H

Jordan Journal of Physics (*JJP*): An International Peer-Reviewed Research Journal funded by the Scientific Research Support Fund, Jordan, and published quarterly by the Deanship of Research and Graduate Studies, Yarmouk University, Irbid, Jordan.

EDITOR-IN-CHIEF:
Ibrahim O. Abu Al-Jarayesh
Department of Physics, Yarmouk University, Irbid, Jordan.
ijaraysh@yu.edu.jo

EDITORIAL BOARD:

Prof. Nabil Y. Ayoub
President, American University of Madaba, Madaba, Jordan.
nabil.ayoub@gju.edu.jo

Prof. Jamil M. Khalifeh (May God have mercy on him)
Department of Physics, University of Jordan, Amman, Jordan.
jkalifa@ju.edu.jo

Prof. Tareq F. Hussein
Department of Physics, The University of Jordan, Amman, Jordan.
t.hussein@ju.edu.jo

Prof. Marwan S. Mousa
Department of Physics, Mu'tah University, Al-Karak, Jordan.
mmousa@mutah.edu.jo

Prof. Mohammad Al-Sugheir
Department of Physics, The HashemiteUniversity, Zarqa, Jordan.
msugh@hu.edu.jo

Prof. Abdalmajeid M. Alyassin
Department of Physics, Yarmouk University, Irbid, Jordan.
alyassin@yu.edu.jo

Prof. M-Ali H. Al-Akhras (AL-Omari)
Department of Physics, Jordan University of Science & Technology, Irbid, Jordan.
alakmoh@just.edu.jo

Prof. Ibrahim A. Bsoul
Department of Physics, Al al-Bayt University, Mafraq, Jordan.
Ibrahimbsoul@yahoo.com

ASSOCIATE EDITORIAL BOARD

Prof. Mark Hagmann
Desert Electronics Research Corporation, 762 Lacey Way, North Salt Lake 84064, Utah, U. S. A.
MHagmann@NewPathResearch.Com.

Dr. Richard G. Forbes
Dept. of Electrical and Electronic Engineering, University of Surrey, Advanced Technology Institute and Guildford, Surrey GU2 7XH, UK.
r.forbes@surrey.ac.uk

Prof. Roy Chantrell
Physics Department, The University of York, York, YO10 5DD, UK.
roy.chantrell@york.ac.uk

Prof. Susamu Taketomi
2-35-8 Higashisakamoto, Kagoshima City, 892-0861, Japan.
staketomi@hotmail.com

Editorial Secretary: Majdi Al-Shannaq.
Languages Editor: Haider Al-Momani

Manuscripts should be submitted to:

Prof. Ibrahim O. Abu Al-Jarayesh
Editor-in-Chief, Jordan Journal of Physics
Deanship of Research and Graduate Studies
Yarmouk University-Irbid-Jordan
Tel. 00 962 2 7211111 Ext. 2075
E-mail: *jjp@yu.edu.jo*
Website: *http://Journals.yu.edu.jo/jjp*

Jordan Journal of

PHYSICS

An International Peer-Reviewed Research Journal

Volume 14, No. 3, September 2021, Safar 1443 H

INTERNATIONAL ADVISORY BOARD

Prof. Dr. Ahmad Saleh
Department of Physics, Yarmouk University, Irbid, Jordan.
salema@yu.edu.jo

Prof. Dr. Aurore Savoy-Navarro
LPNHE Universite de Paris 6/IN2P3-CNRS, Tour 33, RdC 4, Place Jussieu, F 75252, Paris Cedex 05, France.
auore@Ipnhep.in2p3.fr

Prof. Dr. Bernard Barbara
Laboratoire Louis Neel, Salle/Room: D 108, 25, Avenue des Martyrs BP 166, 38042-Grenoble Cedex 9, France.
Barbara@grenoble.cnrs.fr

Prof. Dr. Bruno Guiderdoni
Observatoire Astronomique de Lyon, g, avenue Ch. Antre-F-69561, Saint Genis Laval Cedex, France.
Bruno.guiderdoni@olos.univ-lyon1.fr

Prof. Dr. Buford Price
Physics Department, University of California, Berkeley, CA 94720, U. S. A.
bprice@berkeley.edu

Prof. Dr. Colin Cough
School of Physics and Astronomy, University of Birmingham, B15 2TT, U. K.
c.gough@bham.ac.uk

Prof. Dr. Desmond Cook
Department of Physics, Condensed Matter and Materials Physics Research Group, Old Dominion University, Norfolk, Virginia 23529, U. S. A.
Dcook@physics.odu.edu

Prof. Dr. Evgeny Sheshin
MIPT, Institutskij per. 9, Dogoprudnyi 141700, Russia.
sheshin@lafeet.mipt.ru

Prof. Dr. Hans Ott
Laboratorium Fuer Festkorperphysik, ETH Honggerberg, CH-8093 Zurich, Switzerland.
ott@solid.phys.ethz.ch

Prof. Dr. Herwig Schopper
President SESAME Council, Chairman Scientific Board UNESCO IBSP Programme, CERN, 1211 Geneva, Switzerland.
Herwig.Schopper@cern.ch

Prof. Dr. Humam Ghassib
Department of Physics, The University of Jordan, Amman 11942, Jordan.
humamg@ju.edu.jo

Prof. Dr. Khalid Touqan
Chairman of Jordan Atomic Energy Commission, Amman, Jordan.

Prof. Dr. Nasr Zubeidey
President*: Al-Zaytoonah University of Jordan, Amman, Jordan.*
President@alzaytoonah.edu.jo

Prof. Dr. Patrick Roudeau
Laboratoire de l'Accelerateur, Lineaire (LAL), Universite Paris-Sud 11, Batiment 200, 91898 Orsay Cedex, France.
roudeau@mail.cern.ch

Prof. Dr. Paul Chu
Department of Physics, University of Houston, Houston, Texas 77204-5005, U. S. A.
Ching-Wu.Chu@mail.uh.edu

Prof. Dr. Peter Dowben
Nebraska Center for Materials and Nanoscience, Department of Physics and Astronomy, 255 Behlen Laboratory (10th and R Streets), 116 Brace Lab., P. O. Box 880111, Lincoln, NE 68588-0111, U. S. A.
pdowben@unl.edu

Prof. Dr. Peter Mulser
Instiute fuer Physik, T.U. Darmstadt, Hochschulstr. 4a, 64289 Darmstadt, Germany.
Peter.mulser@physik.tu-darmstadt.de

Prof. Dr. Rasheed Azzam
Department of Electrical Engineering, University of New Orleans New Orleans, Louisiana 70148, U. S. A.
razzam@uno.edu

Prof. Dr. Shawqi Al-Dallal
Department of Physics, Faculty of Science, University of Bahrain, Manamah, Kingdom of Bahrain.

Prof. Dr. Wolfgang Nolting
Institute of Physics / Chair: Solid State Theory, Humboldt-University at Berlin, Newtonstr. 15 D-12489 Berlin, Germany
Wolfgang.nolting@physik.hu-berlin.de

Prof. Dr. Ingo Hofmann
GSI Darmstadt, Planckstr. 1, 64291, Darmstadt, Germany.
i.hofmann@gsi.de

Prof. Dr. Jozef Lipka
Department of Nuclear Physics and Technology, Slovak University of Technology, Bratislava, llkovicova 3, 812 19 Bratislava, Slovakia.
Lipka@elf.stuba.sk

The Hashemite Kingdom of Jordan

Yarmouk University

Jordan Journal of
PHYSICS

An International Peer-Reviewed Research Journal
Funded by the Scientific Research Support Fund

Volume 14, No. 3, September 2021, Safar 1443 H

Instructions to Authors

Instructions to authors concerning manuscript organization and format apply to hardcopy submission by mail, and also to electronic online submission via the Journal homepage website (http://jjp.yu.edu.jo).

Manuscript Submission

1- **E-mail to** : jjp@yu.edu.jo

2- **Online**: Follow the instructions at the journal homepage website.

Original *Research Articles*, *Communications* and *Technical Notes* are subject to critical review by minimum of two competent referees. Authors are encouraged to suggest names of competent reviewers. *Feature Articles* in active Physics research fields, in which the author's own contribution and its relationship to other work in the field constitute the main body of the article, appear as a result of an invitation from the Editorial Board, and will be so designated. The author of a *Feature Article* will be asked to provide a clear, concise and critical status report of the field as an introduction to the article. *Review Articles* on active and rapidly changing Physics research fields will also be published. Authors of *Review Articles* are encouraged to submit two-page proposals to the Editor-in-Chief for approval. Manuscripts submitted in *Arabic* should be accompanied by an Abstract and Keywords in English.

Organization of the Manuscript

Manuscripts should be typed double spaced on one side of A4 sheets (21.6 x 27.9 cm) with 3.71 cm margins, using Microsoft Word 2000 or a later version thereof. The author should adhere to the following order of presentation: Article Title, Author(s), Full Address and E-mail, Abstract, PACS and Keywords, Main Text, Acknowledgment. Only the first letters of words in the Title, Headings and Subheadings are capitalized. Headings should be in **bold** while subheadings in *italic* fonts.

Title Page: Includes the title of the article, authors' first names, middle initials and surnames and affiliations. The affiliation should comprise the department, institution (university or company), city, zip code and state and should be typed as a footnote to the author's name. The name and complete mailing address, telephone and fax numbers, and e-mail address of the author responsible for correspondence (designated with an asterisk) should also be included for official use. The title should be carefully, concisely and clearly constructed to highlight the emphasis and content of the manuscript, which is very important for information retrieval.

Abstract: A one paragraph abstract not exceeding 200 words is required, which should be arranged to highlight the purpose, methods used, results and major findings**.**

Keywords: A list of 4-6 keywords, which expresses the precise content of the manuscript for indexing purposes, should follow the abstract.

PACS: Authors should supply one or more relevant PACS-2006 classification codes, (available at http://www.aip.org/pacs/pacs06/pacs06-toc.html)

Introduction: Should present the purpose of the submitted work and its relationship to earlier work in the field, but it should not be an extensive review of the literature (e.g., should not exceed 1 ½ typed pages).

Experimental Methods: Should be sufficiently informative to allow competent reproduction of the experimental procedures presented; yet concise enough not to be repetitive of earlier published procedures.

Results: should present the results clearly and concisely.

Discussion: Should be concise and focus on the interpretation of the results.

Conclusion: Should be a brief account of the major findings of the study not exceeding one typed page.

Acknowledgments: Including those for grant and financial support if any, should be typed in one paragraph directly preceding the References.

References: References should be typed double spaced and numbered sequentially in the order in which they are cited in the text. References should be cited in the text by the appropriate Arabic numerals, enclosed in square brackets. Titles of journals are abbreviated according to list of scientific periodicals. The style and punctuation should conform to the following examples:

1. Journal Article:

- a) Heisenberg, W., Z. Phys. 49 (1928) 619.
- b) Bednorz, J. G. and Müller, K. A., Z. Phys. B64 (1986) 189
- c) Bardeen, J., Cooper, L.N. and Schrieffer, J. R., Phys. Rev. 106 (1957) 162.
- d) Asad, J. H., Hijjawi, R. S., Sakaji, A. and Khalifeh, J. M., Int. J. Theor. Phys. 44(4) (2005), 3977.

2. Books with Authors, but no Editors:

- a) Kittel, C., "Introduction to Solid State Physics", 8th Ed. (John Wiley and Sons, New York, 2005), chapter 16.
- b) Chikazumi, S., C. D. Graham, JR, "Physics of Ferromagnetism", 2nd Ed. (Oxford University Press, Oxford, 1997).

3. Books with Authors and Editors:

- a) Allen, P. B. "Dynamical Properties of Solids", Ed. (1), G. K. Horton and A. A. Maradudin (North-Holland, Amsterdam, 1980), p137.
- b) Chantrell, R. W. and O'Grady, K., "Magnetic Properities of Fine Particles" Eds. J. L. Dormann and D. Fiorani (North-Holland, Amsterdam, 1992), p103.

4. Technical Report:

Purcell, J. "The Superconducting Magnet System for the 12-Foot Bubble Chamber", report ANL/HEP6813, Argonne Natt. Lab., Argonne, III, (1968).

5. Patent:

Bigham, C. B., Schneider, H. R., US patent 3 925 676 (1975).

6. Thesis:

Mahmood, S. H., Ph.D. Thesis, Michigan State University, (1986), USA (Unpublished).

7. Conference or Symposium Proceedings:

Blandin, A. and Lederer, P. Proc. Intern. Conf. on Magnetism, Nottingham (1964), P.71.

8. Internet Source:

Should include authors' names (if any), title, internet website, URL, and date of access.

9. Prepublication online articles (already accepted for publication):

Should include authors' names (if any), title of digital database, database website, URL, and date of access.

For other types of referenced works, provide sufficient information to enable readers to access them.

Tables: Tables should be numbered with Arabic numerals and referred to by number in the Text (e.g., Table 1). Each table should be typed on a separate page with the legend above the table, while explanatory footnotes, which are indicated by superscript lowercase letters, should be typed below the table.

Illustrations: Figures, drawings, diagrams, charts and photographs are to be numbered in a consecutive series of Arabic numerals in the order in which they are cited in the text. Computer-generated illustrations and good-quality digital photographic prints are accepted. They should be black and white originals (not photocopies) provided on separate pages and identified with their corresponding numbers. Actual size graphics should be provided, which need no further manipulation, with lettering (Arial or Helvetica) not smaller than 8 points, lines no thinner than 0.5 point, and each of uniform density. All colors should be removed from graphics except for those graphics to be considered for publication in color. If graphics are to be submitted digitally, they should conform to the following minimum resolution requirements: 1200 dpi for black and white line art, 600 dpi for grayscale art, and 300 dpi for color art. All graphic files must be saved as TIFF images, and all illustrations must be submitted in the actual size at which they should appear in the journal. Note that good quality hardcopy original illustrations are required for both online and mail submissions of manuscripts.

Text Footnotes: The use of text footnotes is to be avoided. When their use is absolutely necessary, they should be typed at the bottom of the page to which they refer, and should be cited in the text by a superscript asterisk or multiples thereof. Place a line above the footnote, so that it is set off from the text.

Supplementary Material: Authors are encouraged to provide all supplementary materials that may facilitate the review process, including any detailed mathematical derivations that may not appear in whole in the manuscript.

Revised Manuscript and Computer Disks

Following the acceptance of a manuscript for publication and the incorporation of all required revisions, authors should submit an original and one more copy of the final disk containing the complete manuscript typed double spaced in Microsoft Word for Windows 2000 or a later version thereof. All graphic files must be saved as PDF, JPG, or TIFF images.

Allen, P.B., "…………….", in: Horton, G.K., and Muradudin, A. A., (eds.), "Dynamical…….", (North……..), pp….

Reprints

Twenty (20) reprints free of charge are provided to the corresponding author. For orders of more reprints, a reprint order form and prices will be sent with the article proofs, which should be returned directly to the Editor for processing.

Copyright

Submission is an admission by the authors that the manuscript has neither been previously published nor is being considered for publication elsewhere. A statement transferring copyright from the authors to Yarmouk University is required before the manuscript can be accepted for publication. The necessary form for such transfer is supplied by the Editor-in-Chief. Reproduction of any part of the contents of a published work is forbidden without a written permission by the Editor-in-Chief.

Disclaimer

Opinions expressed in this Journal are those of the authors and neither necessarily reflects the opinions of the Editorial Board or the University, nor the policy of the Higher Scientific Research Committee or the Ministry of Higher Education and Scientific Research. The publisher shoulders no responsibility or liability whatsoever for the use or misuse of the information published by JJP.

Indexing

JJP is currently indexing in:

Scopus	ULRICHSWEB™ GLOBAL SERIALS DIRECTORY

Jordan Journal of
PHYSICS
An International Peer-Reviewed Research Journal

Volume 14, No. 3, September 2021, Safar 1443 H

Table of Contents:

Volume 14, Number 3, 2021. pp. 193-200

Jordan Journal of Physics

ARTICLE

Calculation of Excess Stability Functions of Four Binary Alloys

O. W. Abodunrin and **A. A Ajayi**

Department of Mathematical and Physical Sciences, Afe Babalola University, Ekiti State, Nigeria.

Doi: **https://doi.org/10.47011/14.3.1**

Received on: 27/01/2020; *Accepted on: 29/9/2020*

Abstract: The thermodynamic model based on cluster of two atoms is considered with the view to obtaining Scc(0) and the excess stability function of Scc(0). Concentration-concentration fluctuation; Scc(0) of four binary molten alloys was calculated. The thermodynamic properties of these alloys are evaluated based on cluster of two atoms (A & B) or (B & A). Each system has the view of obtaining concentration-concentration fluctuation; Scc(0) enumerating the low-order atomic correlation in the nearest neighbour shell of liquid binary alloys.The highlights of excess stability functions(ES) of Scc(0) of these alloys were reported. The values of Scc(0) for all these alloys are higher than the ideal solution values. The values of Scc(0) for Bi-Cd alloy is close to the ideal Scc (0). The indication of the excess stability of Scc(0) for some alloys is in support of homocoordination. The Scc(0) and excess stability function of Scc (0) for the four alloys are presented.

Keywords: Concentration-concentration fluctuation, Excess stability function, Ordering energy.

Introduction

The neutron diffraction experiment in particular is a very useful tool to obtaining structural information and thermodynamic properties of binary liquid alloys [1]. In most cases, obtaining the experimental data needed for the calculation of specific thermodynamic properties is not a problem (except in some uncommon cases where the experimental data for some alloys may not be available due to cumbersome task involved and experimental difficulties). In principle, Short Range Order (SRO) which has a relationship with Concentration-Concentration Fluctuation in the long wave length limit (Scc (0)) in the literature can be experimentally determined from the knowledge of concentration-concentration partial structural factor, S_{cc} (q) and the number-number partial structural factor S_{NN}(q) [2]. However, these structures are not easily measurable in most diffraction experiments. Hence, SRO is usually computed without necessarily making reference to its experimental values. Additionally, a direct experimental determination of Scc (0) is often avoided due to complexities involved. For this reason, the option of thermodynamic model which is readily used was employed.

In this study, ordering energy values were determined from Scc (0) [3] of which four alloys were considered and in the application of the thermodynamic model using the determined values of ordering energy, the values of Scc(0) and ES were calculated at various temperatures [4].

The calculations of the thermodynamic quantities at different temperatures involve getting the available experimental data and employing a suitable theoretical model. These four candidates (Cd-Ga, Ag-Ge, Al-Au and Bi-Cd liquid alloys) under observation are those with variations in the values of thermodynamic quantities at various temperatures. To be specific, application is therefore made to these alloys which belong to a hereocoordinated and

Corresponding Author: O. W. Abodunrin **Email**: tayoabodunrin@yahoo.com

self-coordinated group of alloys. The alloys were preferred because all of them represent the classes of metals and semiconductors.

Investigations of liquid metallic alloys on the basis of Quasi Lattice Model (QLM) and its usage for extracting values are also found in [5-7], where this model was used for the calculation of some thermodynamic properties of compounds forming binary molten alloys at their melting temperatures.

In this observation, the QLM was applied to Cd-Ga, Ag-Ge,Al-Au and Bi-Cd liquid alloys for the qualitative investigation of their thermodynamic properties. Ordering energy values determined from Scc (0) are recorded in Table 1. Programs were inscribed to generate data for thermodynamic expressions as functions of concentration, c, using ordering energy values, w, coordination number, Z, Boltzmann constant, K and temperature, T presented in Table 1.

TABLE 1. Ordering energy (w) in eV of binary alloys

Alloy	Temperature (^{o}K)	Z	W_1(eV)
Cd-Ga	700	10.0	0.1133
Ag-Ge	1250	10.0	0.0288
Al-Au	1338	10.0	0.0980
Bi-Cd	773	10.0	0.0210

Theory

The calculation of Scc(0) needs on attachment like Excess Stability Function (ES). The variation of this quantity with composition is informative. This view provides facts that shed light on monotonous behavior of excess stability function of nearly ideal solutions with values approaching zero, although it will exhibit one or more peaks for solutions with strong chemical interactions. The positions of peaks correspond to compositions in which ordering (chemical short-range or intermediate-range) will occur. For an ideal solution Scc(0) = X_1X_2, whereas for an alloy exhibiting formation, Scc(0) exhibits one or more dips with values close to zero. Consequently, a maximum in ES corresponds to a minimum in Scc(0). The width and the height of the dip in Scc(0) and the peaks in Es can be shown to be related to the degree and extent of stability of the complex entities. Thermodynamically, the relationship between short-range order parameter: SRO, concentration-concentration fluctuation, Scc(0) and other thermodynamic properties had been sighted in the literature [8-10]. Moreover, between Es and Scc(0), it is given below. The following thermodynamic expressions are from Quasi Lattice Model.

Quasi Lattice Expressions for Various Thermodynamic Functions

Concentration-Concentration Fluctuation in the Long Wavelength Limit

$$Scc(0)=\frac{c(1-c)}{(1+(\frac{Z}{2\beta})(1-\beta)} \qquad (1)$$

where $\eta=\exp(w/ZKT)$ (2)

and Z is the coordination number for the first shell, w is the ordering energy, K is the Boltzmann constant, T is the temperature, c is the concentration of atom A and 1-c is the concentration of atom B;

where $\beta=(1+4c(1-c)[(\eta)(\eta)-1])^{0.5}$ (3)

η and β are thermodynamic parameters which are interwoven.

Excess Stability Function (ES)

$$ES=\frac{RT}{Scc(0)}-\frac{RT}{c(1-c)} \qquad (4)$$

Ideal Concentration - Concentration Fluctuation in the Long Wavelength Limit

$$Scc_{cc}^{id}(0)=c(1-c) \qquad (5)$$

R is the molar gas constant.

Results

TABLE 2. Calculated experimental Scc(0) and ES of Cd-Ga alloy using experimental activity. C_{Cd} is the concentration of cadmium in the alloy at 700 ^{O}K.

C_{Cd}	Scc(0)	Scc(0)id	ES (10^{-3} J/mol)
0.0	0.0000	0.00	0
0.1	0.170	0.09	-30.4301
0.2	0.437	0.16	-23.0545
0.3	0.976	0.21	-21.7494
0.4	1.718	0.24	-20.8615
0.5	1.745	0.25	-20.0060
0.6	1.143	0.24	-19.1580
0.7	0.638	0.21	-18.5918
0.8	0.347	0.16	-19.6044
0.9	0.228	0.09	-39.1390
1.0	0.0000	0.00	0

TABLE 3. Calculated experimental Scc(0) and ES of Ag-Ge alloy using experimental activity. C_{Ag} is the concentration of silver in the alloy at 1250 ^{O}K.

C_{Ag}	Scc(0)	Scc(0)id	ES(10^{-3} J/mol)
0.0	0.0000	0.00	0
0.1	0.112	0.09	-22.6814
0.2	0.193	0.16	-11.1067
0.3	0.262	0.21	-9.8438
0.4	0.303	0.24	-9.084
0.5	0.288	0.25	-5.4856
0.6	0.222	0.24	3.5102
0.7	0.153	0.21	18.4363
0.8	0.104	0.16	37.9742
0.9	0.076	0.09	21.2714
1.0	0.0000	0.00	0

TABLE 4. Calculated experimental Scc(0) and ES of Al-Au alloy using experimental activity. C_{Al} is the concentration of Aluminum in the alloy at 1338 ^{O}K.

C_{Al}	Scc(0)	Scc(0)id	ES (10^{-3} J/mol)
0.0	0.0000	0.00	0
0.1	0.180	0.09	-61.7979
0.2	0.313	0.16	-33.9859
0.3	0.372	0.21	-23.0680
0.4	0.412	0.24	-19.3508
0.5	0.422	0.25	-17.4960
0.6	0.403	0.24	-18.6982
0.7	0.251	0.21	-8.6549
0.8	0.268	0.16	-28.0182
0.9	0.151	0.09	-49.9314
1.0	0.0000	0.00	0

TABLE 5. Calculated experimental Scc(0) and ES of Bi-Cd alloy using experimental activity. C_{Bi} is the concentration of bismuth in the alloy at 773 ^{O}K

C_{Bi}	Scc(0)	Scc(0)id	ES(10^{-3} J/mol)
0.0	0.0000	0.00	0
0.1	0.089	0.09	-0.8023
0.2	0.166	0.16	-1.4516
0.3	0.250	0.21	-4.8961
0.4	0.296	0.24	-4.6168
0.5	0.296	0.25	-3.5459
0.6	0.256	0.24	-1.6736
0.7	0.204	0.21	0.9004
0.8	0.156	0.16	1.0310
0.9	0.065	0.09	27.4645
1.0	0.0000	0.00	0

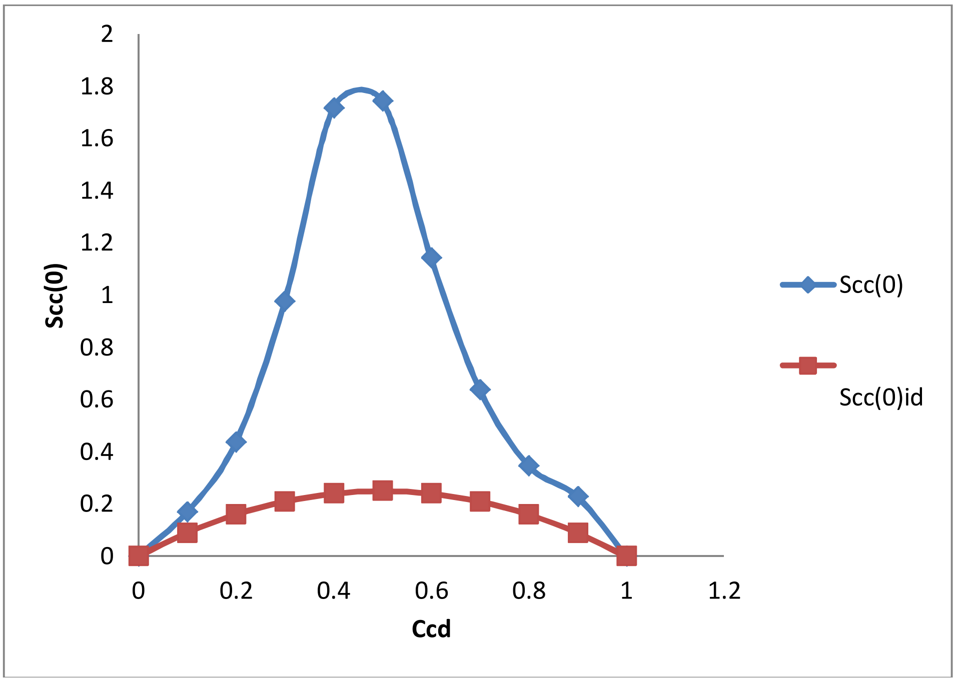

FIG. 1. Scc(0) of Cd-Ga against concentration C_{Cd}.

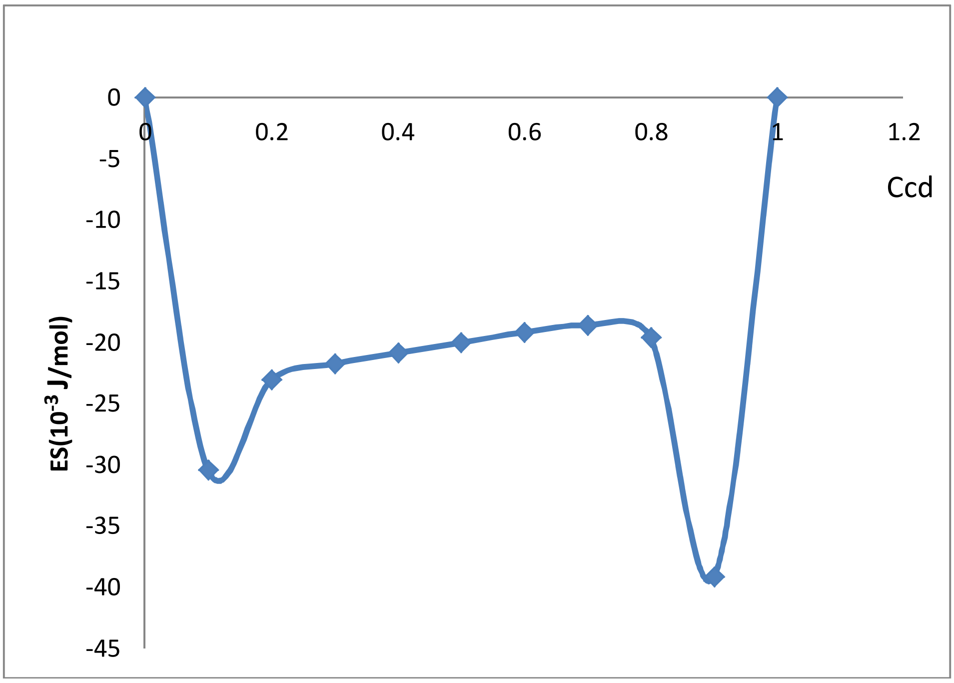

FIG. 2. ES of Cd-Ga against concentration C_{Cd}.

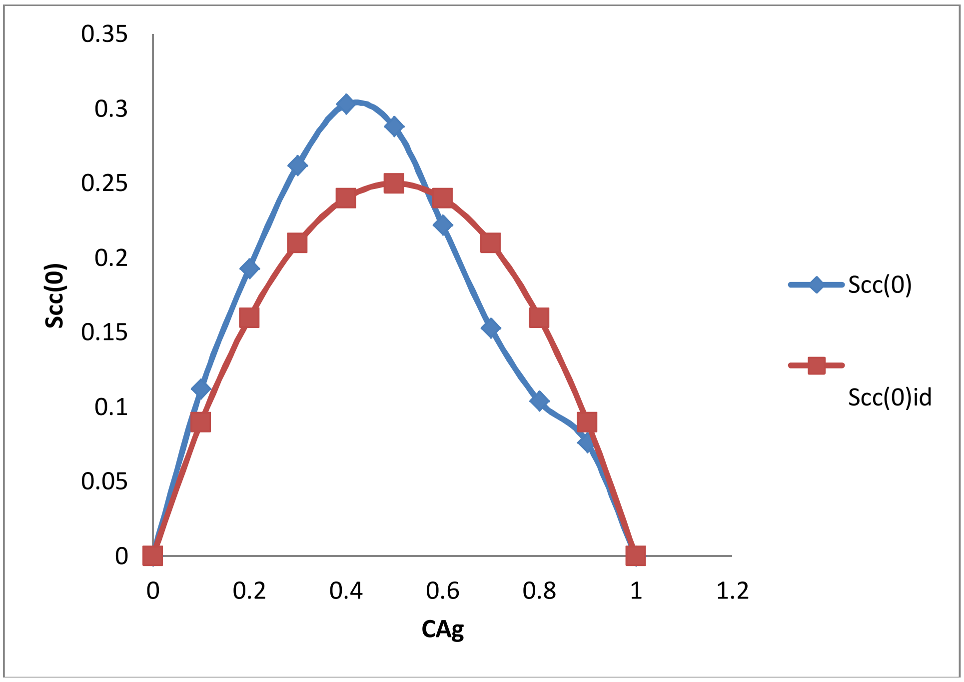

FIG. 3. Scc (0) of Ag-Ge against concentration C_{Ag}.

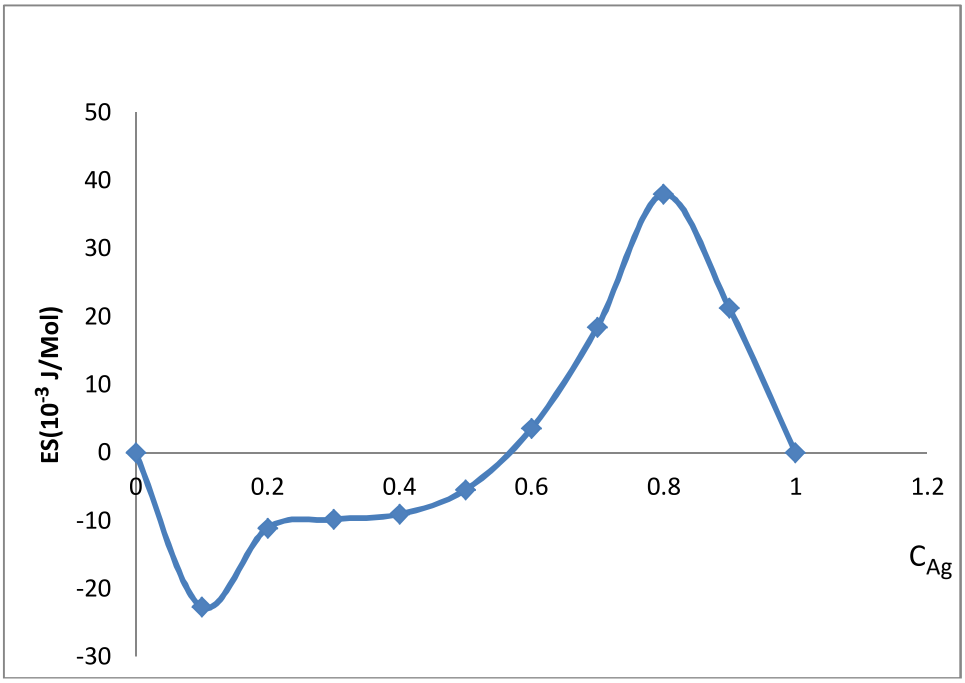

FIG. 4. ES of Ag-Ge against concentration C_{Ag}.

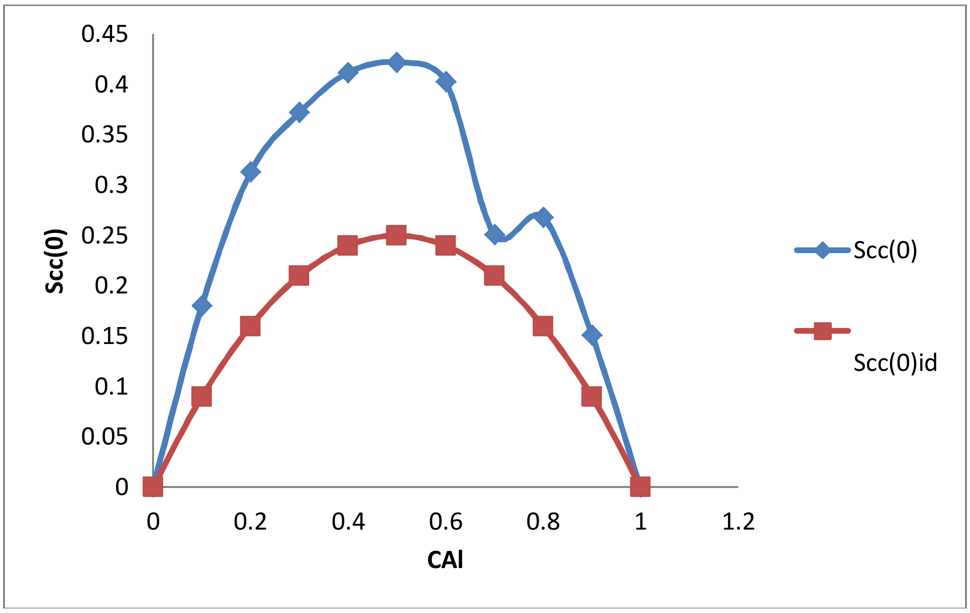

FIG. 5. Scc (0) of Al-Au alloy against concentration C_{Al}.

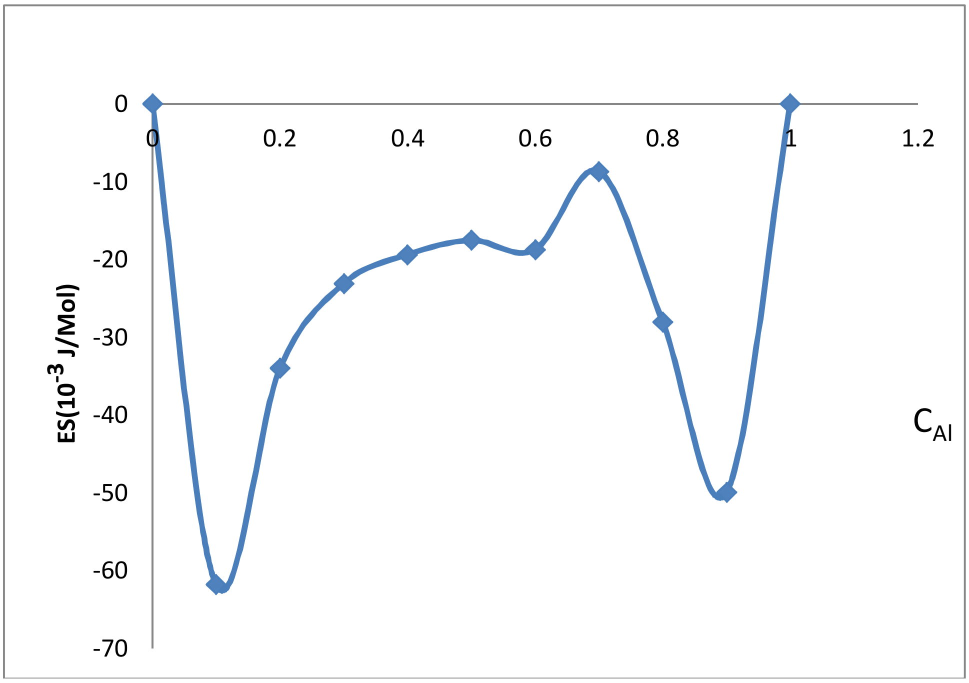

FIG. 6. ES of Al-Au alloy against concentration C_{Al}.

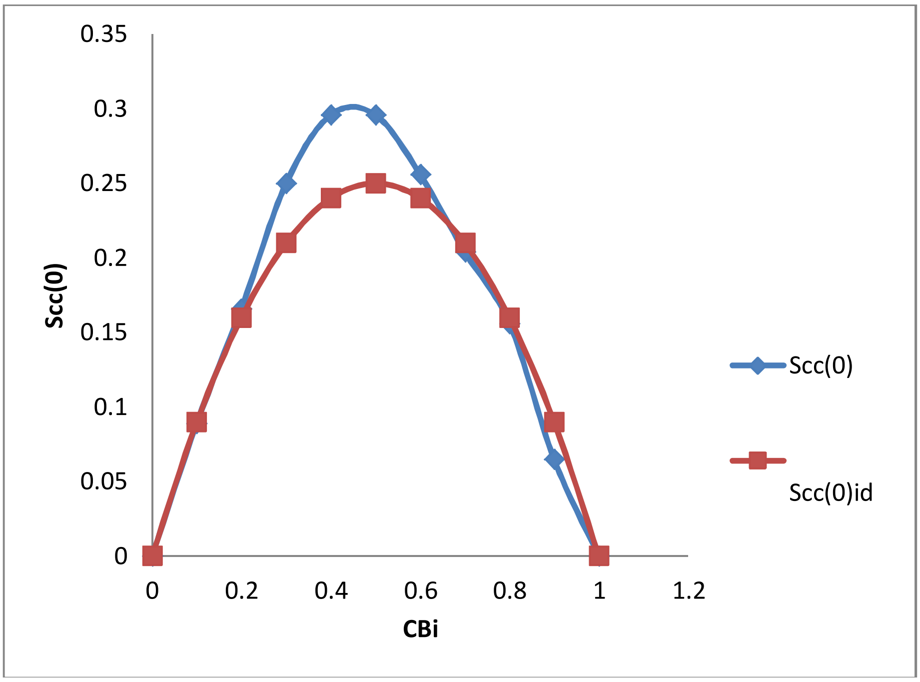

FIG. 7. Scc(0) of Bi-Cd against concentration C_{Bi}.

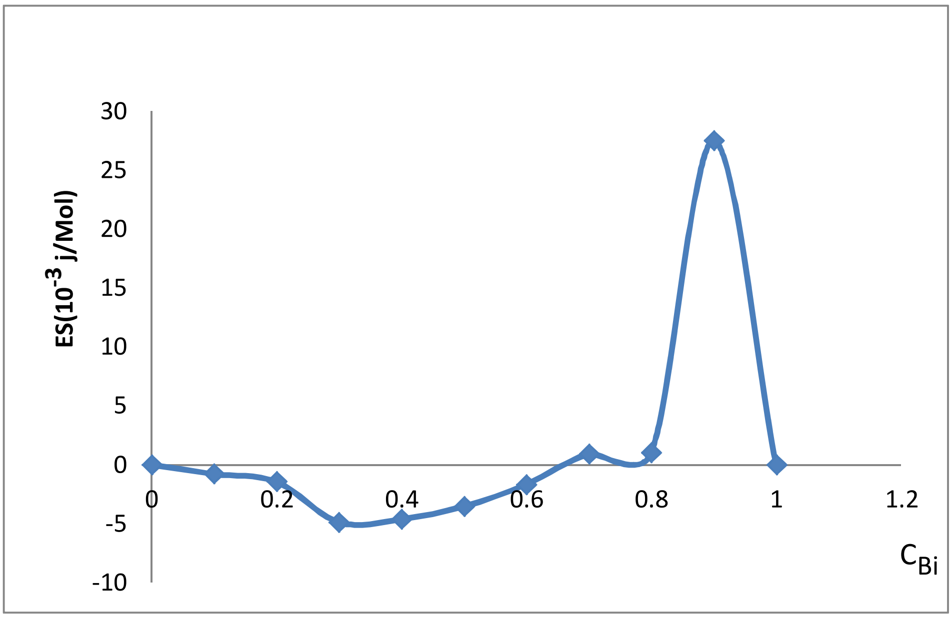

FIG. 8. ESof Bi-Cd against concentration C_{Bi}.

Discussion

Figs. 1, 3, 5 and 7 show the plots of concentration-concentration fluctuation Scc (0) against concentration of element for Cd-Ga, Ag-Ge, Al-Au and Bi-Cd liquid alloys at their melting temperatures. The Scc(0) of these alloys increases initially to a maximum (owing to the charge transfer between neighboring atoms) within the entire concentration range with distinct peaks at C_{Cd} = 0.5, C_{Ag} = 0.4 and C_{Bi} = 0.4 and the remaining liquid alloy has some depression at the right side of the curve (owing to chemical alternation of positive and negative charges with length scale approximately twice the nearest neighbor distance) at C_{Al} = 0.7. In Fig. 5, the curve of Scc (0) against C_{Al} of aluminum-gold alloy rises above the ideal solution curve (because of the topological short-range order; i.e., geometrical arrangements of atoms), indicating homocoordination (preference of like atoms as the nearest neighbors). Fig. 3 has an ideal solution curve intersecting with the curve of Scc (0) at concentration between C_{Ag} = 0.5 and 0.6 because of directional bonding. In Fig. 7, the calculated Scc (0) is in perfect agreement with ideal solution values at points C_{Bi} = 0, 0.1, 0.2, 0.7, 0.8 and 1.0, but with observed disagreement at points C_{Bi} = 0.3, 0.4, 0.5, 0.6 and 0.9. This is because there is a near cancellation of the ionic potentials, while at large distances ionic potentials were screened. Fig. 7 also has its calculated values for Scc(0) of Cd-Ga above the ideal solution values, which is in support of homocoordination or self-coordination.

Figs. 2, 4, 6 and 8 show the plots of excess stability function *versus* concentration of element. The display in Fig. 2 shows an initial decrease in the curve to a minimum (possibly when the disordered potential is too large) with a corresponding gradual increase and some fluctuations with concentration. The excess stability function has negative values; it falls downward to concentration C_{Cd} = 0.1 before ascending in a straight line between C_{Cd} = 0.2 and 0.8 eventually with a repetition of what was displayed at C_{Cd} = 0.1 being also displayed at C_{Cd} = 0.9 with minimum excess stability function between C_{Cd} = 0.8 and 1.0 which was lower than what was observed at the initial stage of the curve. The excess stability function displayed in Fig. 4 shows an initial decrease as the concentration increases and subsequent increase in concentration makes excess stability function reach the highest value. In Fig. 6, the display shows the short-range repulsive potential which prevented the atoms of Au and Al from reaching each other, thereby allowing the Es values to be completely negative throughout the concentration. In Fig. 8, as the concentration increases, there was a corresponding decrease in the excess stability function (due to interatomic potentials repelled by the central potential) between C_{Bi} = 0.2 and 0.6 with negative significance. A sharp increase in excess stability up to maximum value (due to pair correlation function thus formed at a distance a little greater than the effective diameter) in the concentration range C_{Bi} = 0.8-0.9 was observed before falling sharply to zero excess stability function at C_{Bi} = 1.0. Lastly, the peaks of excess stability function were obtained in the concentration range of 0.8 for Ag-Ge and 0.9 for Bi-Cd, except for Al-Au and Cd-Ga liquid alloys.

Conclusion

Ag-Ge and Bi-Cd liquid alloys are chemically strong interacting compounds with chemical short-range order. The dip in Al-Au liquid alloy is an indication of slight formation. The width and height of excess stability function at a specific concentration for Ag-Ge is a candidate of stability possibly in excess. The narrow width and considerable height of excess stability function for Bi-Cd are described with strong stability and Cd-Ga liquid alloy is a weak interacting system with an intermediate range.

References

[1] Singh, R.N., Candian Journal of Physics, 65 (3) (1987) 309.

[2] Bhatia, A.B. and Hargrove, W.H., Physical Review B, 10 (8) (1974) 3186.

[3] Lele, S. and Ramchandrarao, P., Metallurgical and Materials Transactions B, 12 (4) (1981) 659.

[4] Chatterjee, S.K. and Prasad, L.C., Indian Journal of Pure and Applied Physics, 42 (2004) 283.

[5] Adhikari, D., Singh, B.P, Jha, I.S. and Singh, B.K., Journal of Molecular Liquids, 156 (2-3) (2010) 115.

[6] Singh, P., Physical Review B, 121 (2) (1987) 243.

[7] Kotova, N., Golovata, N. and Usenko, N., Bulletin of Taras Shevchenko National University of Kyiv. Chemistry, 1 (55) (2018) 46.

[8] Khanna, K.N. and Singh, P.P., Phys. Status Solidi B, 122 (3) (1987) 233.

[9] Singh, P., Physical Review B, 124 (3) (1984) 253.

[10] Awe, O.E., Akinwale, I., Imeh, J. and Out, J., J. of Phys. Chem. of Liq., 48 (2) (2009) 243.

Volume 14, Number 3, 2021. pp. 201-208

Jordan Journal of Physics

ARTICLE

Fundamental and Harmonic Self Mode-locking in Mid IR Heavily Doped Fiber Lasers

Fadi Z. Qamar

Physics Department, Faculty of Sciences, Damascus University, Damascus, Syria.

Doi: **https://doi.org/10.47011/14.3.2**

Received on: 28/04/2020; *Accepted on: 7/9/2020*

Abstract: Harmonic self mode-locking effects are observed in heavily doped fiber lasers operating near 3 μm. The temporal profiles for the output of an Er-ZBLAN fiber laser operating at ~2.7 μm and an Ho, Pr-ZBLAN fiber laser operating at ~2.87 μm are reported. Stable second harmonic mode-locking is observed in the Er-ZBLAN fiber laser under 970nm pumping for an Er concentration of 50000 ppm, while unstable harmonic mode-locking of order of between 1-1/7 times the round cavity round trip time was observed for the higher concentration of 80000 ppm and for all pump powers. Unstable harmonic mode-locking is observed in the Ho, Pr-ZBLAN fiber laser when pumped at 1064nm, for fiber lengths up to 13m and for all pump powers. The experimental mode-locked pulse train periods are found to be consistent with theoretical analysis. The origin and properties of harmonic self mode-locking in heavily doped ZBLAN fiber lasers operated near 3 μm are discussed.

Keywords: Er-ZBLAN fiber laser, Ho, Pr-ZBLAN fiber laser, Self mode-locking, Harmonic self mode-locking.

PACS: Fiber lasers, 42.55.Wd, Mode locking, 42.60.Fc.

Introduction

Pulsed Fluoride glass fiber lasers of various configurations have exhibited both continuous wave (CW) and pulsed output at power levels in the 2W range at wavelengths in the 2.7-3 μm spectral region, that can be useful for numerous medical, industrial and research applications. These fiber lasers have potential advantages of being flexible (the laser output can easily be guided into difficult regions), compact, efficient, reliable and low cost compared with other bulk lasers. In addition to all these advantages, the temporal profile of these fibers is very rich in effects and their nonlinear properties make them attractive for ultra-short pulse production which might be useful for medical and surgery, sensing materials processing with high moisture content, textile manufacturing and general research applications. Ultrashort pulse generation in lasers generally relies on mode-locking by amplitude modulation (AM) or frequency modulation (FM) at the cavity round trip frequency. These effects can be induced actively or passively in the cavity. However, some cavities incorporate self-focusing or extra-nonlinear effects resulting in self mode-locking (SML) [1,2]. SML has been reported in gas [3], dye [4] and solid state (particularly the Ti-sapphire) and ruby lasers [2,5]. Self mode-locking in CW or pulsed operation has been reported for many fibers operating between 1 and 2 μm; these include neodymium [6,7], ytterbium [8], erbium [9 -11], thulium-silica [12 -14], thulium-holmium [15] and thulium-ZBLAN [16]. The details of the previous observations can be found in [12]. Self-locking in fiber lasers has been attributed to either the possible existence of Brillouin scattering in the output of the pulsed fiber laser [17 - 19], the

Corresponding Author: Fadi Qamar **Email**: fadiqamar@Hotmail.com

optical Kerr effect and the presence of self-phase modulation [6], frequency pulling contribution for the doped material [7] or the existence of saturable absorption in the fiber core [12] as a result of the creation of colour centres during the up-conversion lasing [16].

Harmonic mode-locking is another interesting feature which was reported in some fiber lasers where additional pulses can be observed located in-between the train of the phase-locked pulses when the fiber is passively mode-locked [20, 21]. Harmonic mode-locking is also observed in stimulated Brillouin scattering (SBS) fiber lasers due to hole burning in the spectrum of SBS in optical fibers [22]. Harmonic mode-locking can be used to scale up the repetition rate of femtosecond fiber lasers which may be very useful for some applications, although the time jitter of the harmonic mode-locked pulses around their average positions might be relatively high. The repetition rate of the harmonic mode-locking can be simply changed by variation of the pump power level to the fiber cavity [23]. Harmonic mode-locking is generally observed in soliton fiber laser with negative group velocity dispersion [24] and is interpreted as being due to a repulsive force between the pulses that is generated by phase effects in saturable absorption [25], as well as the recovery dynamics in the saturated gain medium [26]. Additionally, the interaction of the soliton pulses with a small oscillating continuum in the cavity can produce repulsive and attractive forces between the pulses leading to harmonic mode-locking. Acoustic resonance of the fiber at subgigahertz frequencies leads to further stabilization of the harmonically mode-locked train and particularly can reduce the time jitter to very small values [27, 28].

In this study, harmonic self-locking is observed in fibers emitting near 3μm. Self-mode locking has not been reported previously in fibers emitting in the 3μm spectral region and harmonic mode-locking in general has not so far been observed in any fibers which incorporate self mode-locking. The repetition rate and the stability of the mode-locking are established to be dependent on the concentration of the dopant as well as the length of the fiber, while no significant dependence is observed on the strength and condition (CW or pulsed) of the pump on stability and the repetition rate of the harmonic self-locking.

Experimental Techniques and Measurements

The following fiber lasers were used for these studies:

1) A double-clad Er-doped ZBLAN fiber laser that has a rectangular-shape to match the shape of the pump beam of a high power 970 nm diode laser and promote cladding-to-core coupling, 40 mm diameter core which supported multi transverse mode operation, core numerical aperture (NA) of 0.12, first clad NA of 0.5, a rectangular first cladding with a dimensions of 150 and 200 mm. Two different doped core concentrations have been used, 50000 ppm molar for a fiber length of 7.3 m and 80000 ppm molar for a fiber length of 11.3 m.
2) A single-clad Ho, Pr doped- fluoride fiber with concentrations of 30000 ppm molar Ho and 3000 ppm molar Pr, a core diameter of 15μm, a numerical aperture of 0.13, an intrinsic loss of ~30 dB/km at 800 nm and supported single mode operation. Laser action in this fiber had been previously demonstrated [29, 30].

Observations of Harmonic-Locking in Double-Clad Er-Doped ZBLAN Fiber Lasers

The experimental arrangement is shown in Fig. 1.

The Er-doped fiber laser was pumped by a 30 W diode laser operating at 970 nm. The diode provided both CW and square pulse pumping with minimum duration and period of 1 ms. The pump was launched to fiber *via* objective lens with numerical aperture (NA) of 0.25. The fiber was butted to the mirror, highly reflecting at the lasing wavelength and with high transmittance at the pump wavelength. The distal facet of the fiber was butted to a Ge filter to reflect the pump wavelength, as well as to provide feedback to the cavity. The temporal behaviour of the output was monitored by an InGaAs photodiode (Hamamatsu G8423-03) with a cut-off frequency of 60 MHz and a rise time of ~ 6 ns. The photodiode has a cut-off wavelength of 2.6 μm and was used as a two-photon absorption detector; however, a Ca_2F lens was used to focus the light into the detector and thus increase the gain.

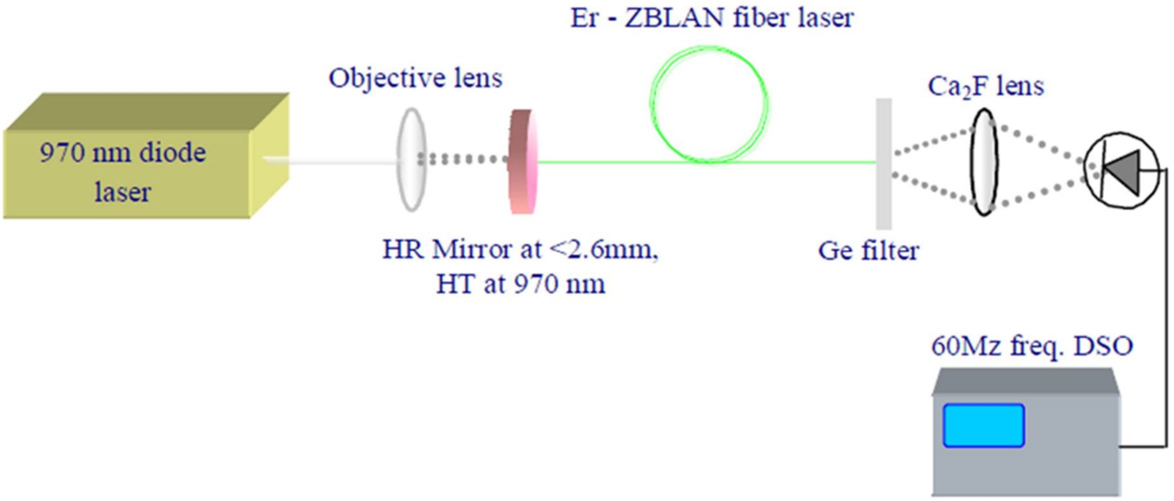

FIG. 1. Experimental arrangement for diode pumped Er-doped ZBLAN fiber laser. (DSO-digital sampling oscilloscope).

Cutback experiments showed that more than 82 % of the pump light was launched into the fiber, which resulted in a maximum power of 300 mW with ~18 % slope efficiency after the threshold of 100 mW launched power, for a fiber length of 7.6 m with a dopant concentration of 50000 ppm. A maximum power of 190 mW with ~11% slope efficiency after the threshold of 300 mW was produced for a fiber length of 11.3 m with a dopant concentration of 80000 ppm. The temporal output for the 50000 ppm Er-doped fiber showed that at low pump power, near the threshold, the output was self-pulsing with a chaotic pulse burst; each of these pulses consisted of a train of small pulses with a time period between pulses of 37.5 ns, which is equal to half the cavity lifetime T_R. At higher pump power, the output changed into CW and a train of small pulses was also observed within the output at the same repetition rate. Thus, there was no significant effect of pump power on the generation of the train of short pulses or on changes in its repetition rate, where the pulse train appeared to be almost stable for all pump powers, as shown in Fig. 2.

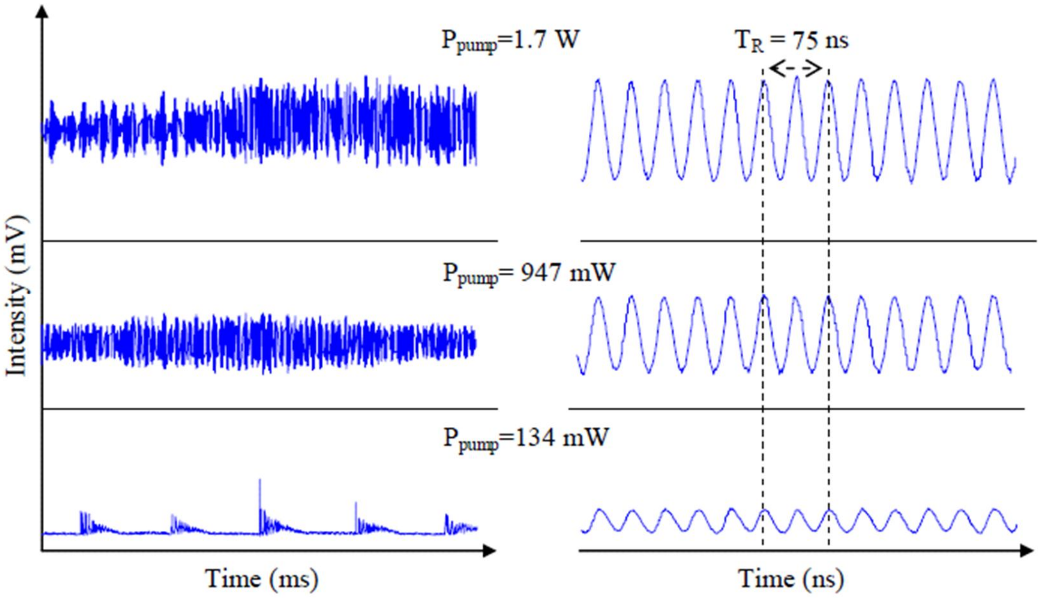

FIG. 2. Self-locking observations in the output of Er-doped ZBLAN fiber laser with a concentration of 50000 ppm molar, at various pump powers. The fiber length was 7.3 m and the self mode-locking occurred at half the cavity round trip time T_R.

More investigations were carried out using a longer fiber of about 11.3 m, with a higher concentration of 80000 ppm molar. The temporal output showed similar observation to the first experiment, but with an unstable train of short pulses and with more harmonic order. Fig. 3 shows that for all pump powers down to the threshold, the train of short pulses mainly consisted of a train of short pulses with a time interval between pulses matching the cavity round trip time T_R, and after a short time, more pulses started to develop in between the main pulses resulting in a train of short pulses with period time varying between T_R and 1/4 T_R and pulses became weaker for time periods between 1/5 T_R and 1/7 T_R.

However, the train of short pulses was also seen in the pulsed output of the fiber when pulsed pumped with 1ms on- and 1ms off-pulses, as in Fig. 4.

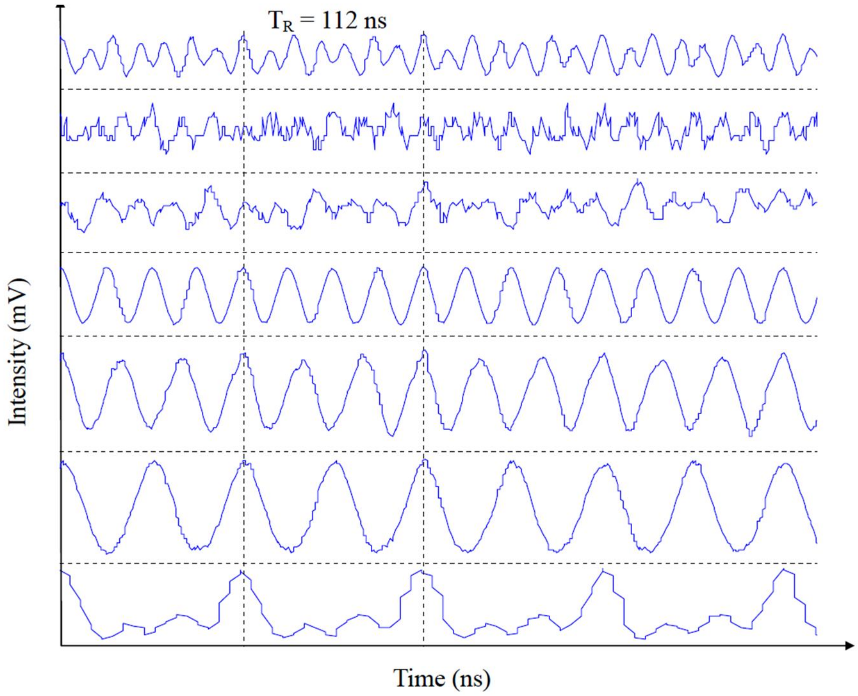

FIG. 3. Self-locking observations in the output of 11.3 m, Er-doped ZBLAN fiber laser with a concentration of 80000 ppm molar. The self locking occurred at different harmonics of the round trip cavity time T_R, ranging between 1 and 1/7.

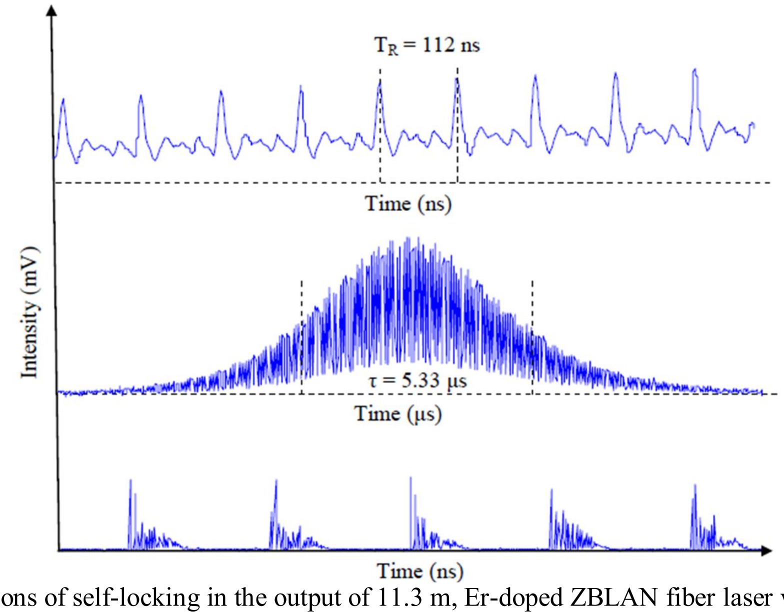

FIG. 4. Observations of self-locking in the output of 11.3 m, Er-doped ZBLAN fiber laser when pulse pumped by a modulated input, 1ms on and 1ms off, from 970 nm diode laser. The peak power of the high intensity laser pulse was 2.1W.

Observations of Harmonic-Locking in Single-Clad Ho, Pr-Doped ZBLAN Fiber Lasers

Fig. 5 shows the experimental arrangement for this study.

The fiber was pumped by a single-mode vertically polarized Nd: YAG laser operating at 1064 nm. An objective lens with a NA of 0.25 was used to launch the pump laser light reflected from a 45° dichroic mirror into the fiber. The mirror was 99 % HR at the pump wavelength and 97% HT with an antireflection coating at the lasing wavelength. The end facet of the fiber was butted against an HR mirror at both the pump and lasing wavelengths, so that the cavity consisted of Fresnel reflection and a highly reflecting mirror. Cut-back measurements were carried out in which the launch and the slope efficiencies and optimum length of the fiber were determined. It was found that approximately 85% of the incident power could be launched into the fiber resulting in more than 600 mW output power at a slope efficiency of ~ 9% for the near optimum length of the fiber laser of 9.2 m. The detection of the output was carried out using an InGaAs photodiode.

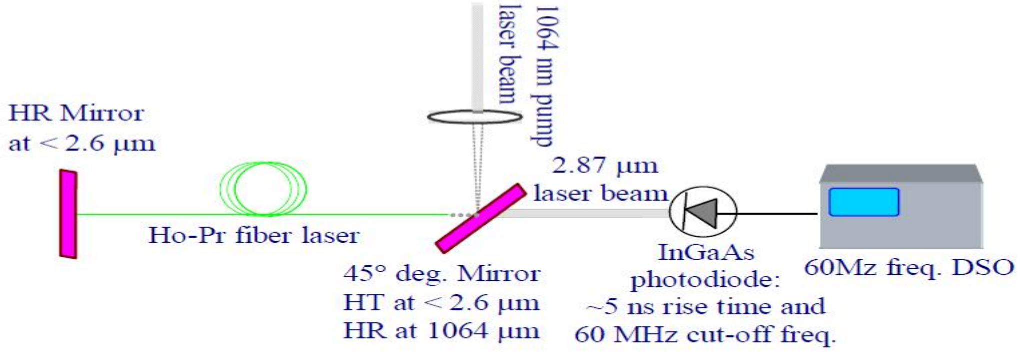

FIG. 5. Experimental arrangement for Ho, Pr-doped ZBLAN fiber laser pumped by an Nd: YAG laser.

The temporal profiles of the output for several lengths of the fiber: 8.84 m, 9.2 m, 9.75 m, 10.6 m and 13.25 m, were investigated. The output consisted of a train of short pulses with a time interval which fluctuated between T_R and 1/3 T_R for fiber lengths > 9.2 m and was fixed at the around cavity round trip time for 8.8m, as shown in Fig. 6.

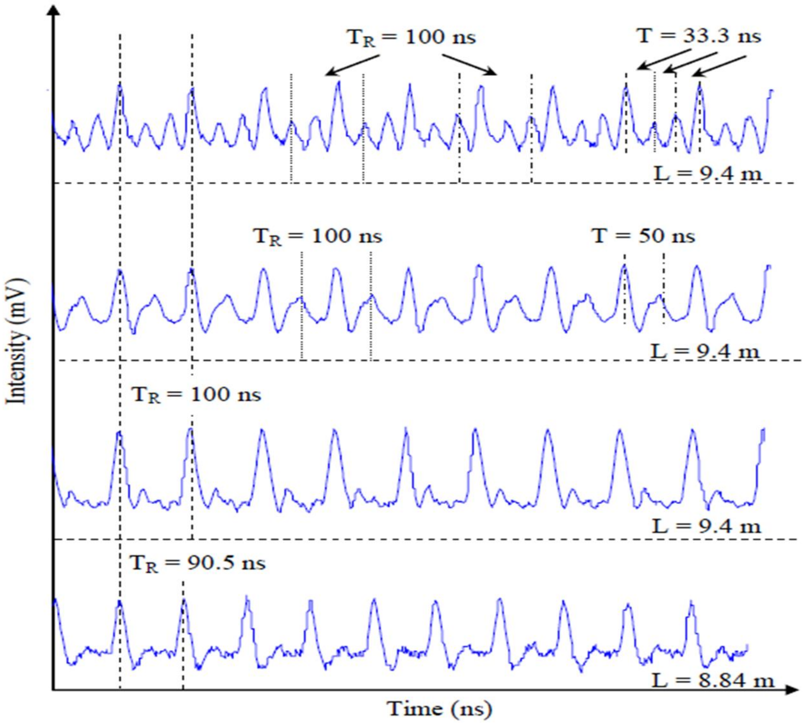

FIG. 6. Observation of self-locking in the output of Ho, Pr-doped ZBLAN fiber laser. For a fiber length of 9.4 m, the self-locking was unstable and the period between the pulses varied between 1 and 1/3 T_R (cavity round trip time). For shorter fiber length, 8.84 m, the self-mode-locking time was fixed at the cavity round trip time T_R.

Similar to the observations on the Er fiber, no effect was found on the strength of the pump power on the temporal behaviour of the fiber; the train of short pulses was observed for all powers down to the threshold, as shown in Fig. 7.

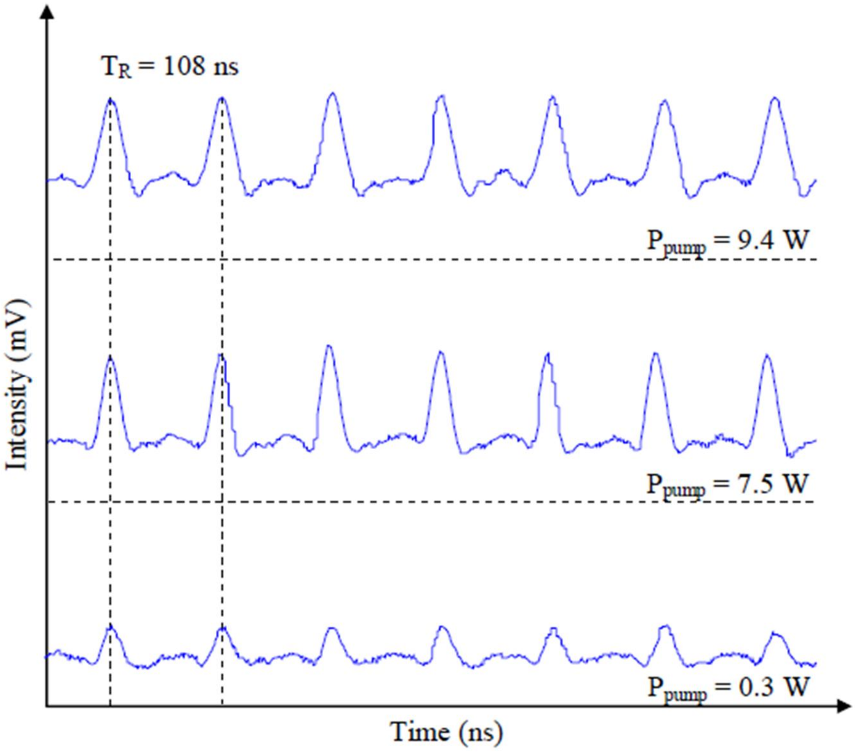

FIG. 7. Self-locking observations in the output of the Ho, Pr-doped ZBLAN fiber laser at various pump powers for a fiber length of 10.6 m. The period between the pulses varied between 1 and 1/3 T_R (cavity round trip time); for the purpose of comparison, the train of pulses which locked at the time equal to the cavity round trip is shown in this figure.

The period between the two main pulses was measured for several lengths of the fiber and matched the round trip cavity time which can be calculated from T = 2nl/c, where n is the refractive index of the fiber, L is the length of the cavity and c is the velocity of light. Fig. 8 shows a perfect match between the experimental results and theoretical values for the single-clad Ho^{3+}, Pr^{3+}-doped ZBLAN fiber laser considering n ~ 1.52 for this fiber.

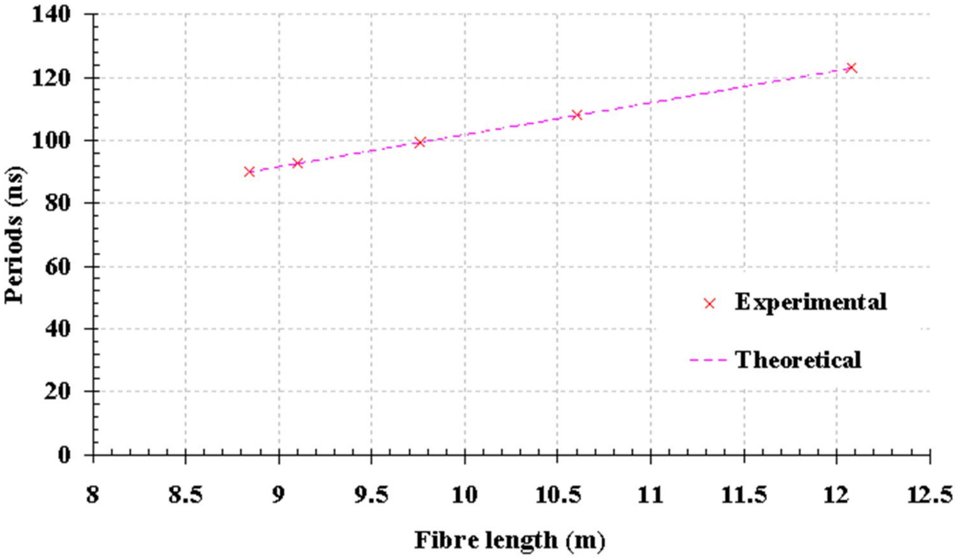

FIG. 8. Comparison between the experimental results and theoretical values of the self-locking at cavity round trip time, observed in the output of Ho, Pr-doped ZBLAN fiber laser.

Discussion

The experimental observations showed that the output of the heavily fluoride fiber laser emitting near 3 μm consisted of a train of short pulses. For true mode-locking, the period between two main pulses should match the round trip cavity time, TR =2nl/c, where n is the refractive index of the fiber, l is the length of the cavity and c is the velocity of light. Fig. 8 shows a perfect match between the experimental and theoretical values for the single-clad Ho, Pr-doped ZBLAN fiber laser assuming n~1.52 for this fiber. The same match has also been found between the experimental results (75 ns and 113ns) and theoretical values (74.6ns, 112.8 ns) for the 50000 and 80000 ppm double-clad Er-doped ZBLAN fibers considering the fiber refractive index n~1.47. The harmonics of the theoretical values match the harmonics of the experimental results. This suggests that the fiber is self-locked at the harmonics of the round trip cavity. This self-locked output was accompanied by CW emission which indicated that not all the longitudinal modes are locked and this may be because the fiber is a high-gain medium and very strong locking should apply. Also, from previous observations, it was demonstrated experimentally that the key elements required to generate stable and perhaps full CW mode-locking with 100 % modulation depth are the length of the fiber as well as the dopant concentration. According to our previous studies [12, 13], the origin of the mode-locking effect in heavily doped fiber lasers may be considered to be due to the following mechanisms:

a) The un-pumped far end of the fiber re-absorbed the laser beam and thus acted as an internal passive saturable absorber. The modulation depth and recovery time of this passive saturable absorber increases with the length of the fiber. For a very long fiber, the modulation by saturable absorber becomes strong enough to lock some of the longitudinal modes on a time scale shorter than the round trip cavity [18 -25].
b) The frequency pulling contribution for the heavily doped material is strong enough to lock some of the longitudinal modes to match the round trip cavity time and possibly for the more heavily doped fiber, as was seen for the Er-doped ZBLAN fiber. This frequency becomes large enough to lock some of the modes on a time scale shorter than the round trip cavity time. Also, the interactions between ions in the heavily doped fiber at certain dopant levels become larger, as the ion-ion distance is smaller. This leads to huge fluctuations in the self-locking of the output; i.e., continuous changing of the locked pulse repetition frequency.
c) Another possible explanation is that the self-locking is due to the Stark levels within the $^{13}I_2$ and $^5I_7$ energy levels in Er- and Ho, Pr-doped fluoride fiber lasers [31]. The self-locking is considered to result from ion-pair interaction, leading to fast movement between the Stark levels in the lower lasing energy level of the $^{13}I_2$ in Er and $^5I_7$ in Ho, thus acting like a fast saturable absorber. The ion-pair interaction increases with the longer fiber as the effective area of the saturable absorber increases for the longer fiber length, resulting in stronger absorption effects and thus stronger modulation. This interaction can be increased by increasing the concentration of the dopant material. Strong ion-pair interaction between the Stark levels can lead to a very fast recovery time and strong modulation in the laser cavity, which in turn can be responsible for locking the modes in a time shorter than the cavity round trip.

Conclusion

The temporal profiles of the output of an Er-ZBLAN fiber operating at ~2.7 μm and an Ho, Pr-ZBLAN fiber operating at ~2.87 μm have been investigated. The temporal profiles of the output of these fiber lasers are found to be self mode-locked. The self mode-locking was stable for short fibers or for low concentrations. For the Er-doped ZBLAN fiber, the output was locked at half the round trip cavity time for a fiber with a concentration of 50000 ppm or at harmonics of the round trip cavity time for a fiber of 80000 ppm, with interpulse periods up to 1/7 T_R. The output from the Ho, Pr-doped ZBLAN fiber was locked at the cavity round trip time for a fiber of 8.8 m length, while it was locked at harmonics of this time for longer fibers. The length and concentration of the doped material have a major effect on the repetition rate and stability of the self mode-locking in these fibers, while no dependence was found on the pump strength in the self-locking behaviour. The origin of the harmonic self mode-locking in heavily doped 3μm fiber lasers is attributed to the existence of saturable absorption in the fiber core, frequency pulling contribution for the doped material or ion-pair interactions leading to fast movement between the Stark levels in the lower lasing energy levels.

References

[1] Smith, D.P.W., Proceedings of the IEEE, 58 (1970) 1342.

[2] Spence, D.E., Kean, P.N. and. Sibbett, W, Opt. Lett., 16 (1991) 42.

[3] Baker, H.J. and King, T.A., J. Phys. D. (Appl. Phys), 6 (1973) 395.

[4] Sorokin, P.P., Lankard, J.R. and Moruzzi, V.L., Appl. Phys. Lett., 15 (1969) 179.

[5] Modru, H.W. and Collins, R.I., Appl. Phys. Lett., 7 (1965) 270.

[6] Hool, Y.C. and Ahmad, H.B., Opt. & Las. Tech., 28 (1996) 223.

[7] Glas, P., Naumann, M., Schirrmacher, A., Daweritz, L. and Hey, R., Optics Comm., 161 (1999) 345.

[8] Jian-zhong, L., Yi-mei, H., Die-chi, S., Hong-bing, Y., Shu-jian, W. and You-xing, Liu, Chin. J. of Las., A29 (2002) 865.

[9] Nakazawa, M., Suzuki, K., Kubota, H. and Kimura, Y., Opt. Lett., 18 (1993) 613.

[10] Zhou, D., Wei, L. and Liu, W., Apl. Opt., 51 (2012) 2554.

[11] Zhang, X., Shu, S., Cai, K., Wang, Y. and Tonga, C., Optics & Laser Tech., 129 (2020) 106285.

[12] Qamar, F.Z. and King, T.A., J. of Mod. Opt., 52 (2005) 1053.

[13] Qamar, F.Z. and King, T.A., J. of Mod. Opt., 52 (2005) 1031.

[14] Swiderski, J. and Michalska, M., Opt. Lett., 38 (2013) 1624.

[15] Eichhorn, M. and Jackson, S.D., Opt. Lett., 33 (2008) 1044.

[16] Booth, J., Mackechnie, C.J. and Ventrudo, B.F., IEEE J. Quant. Electron., 32 (1996) 118.

[17] Agrawal, G.P., “Nonlinear Fiber Optics”, Second edition, (Academic Press, San Diego, 1995).

[18] Smith, R.G., Appl. Opt., 11 (1972) 2484.

[19] Floch, S.L. and Cambon, P., J. Opt Soc. of Am. A, 20 (2003) 1132.

[20] Wang, J., Bu, X., Wang, R., Zhang, L., Zhu, J., Teng, H., Han, H. and Wei, Z., Opt. Lett., 53 (2014) 5088.

[21] Li, X., Zou, W. and Chen, J., Opt. Exp., 23 (2015) 21424.

[22] Kovalev, V.I. and Harrison, R.G., Opt. Commun., 204 (2002) 349.

[23] Fermann, M.E. and Minelly, J.D., Opt. Lett., 21 (1996) 970.

[24] Grudinin, A.B. and Gray, S., J. of Opt. Soc. of Am. B, 14 (1997) 144.

[25] Gray, S. and Grudinin, A.B., Opt. Lett., 21 (1996) 207.

[26] Collings, B.C., Bergman, K. and Knox, W.H., Opt. Lett., 23 (1998) 123.

[27] Gray, S., Grudinin, A.B., Loh, W.H. and Payne, D.N., Opt. Lett., 20 (1995) 189.

[28] Pilipetskii, A.N., Golovchenko, E.A. and Menyuk, C.R., Opt. Lett., 20 (1995) 907.

[29] Jackson, S.D., Opt. Lett., 29 (2004) 334.

[30] Qamar, F.Z., King, T.A., Jackson, S.D. and Tsang, Y.H., J. Lightwave Tech., 23 (2005) 4315.

[31] Dieke, G.H. and Crosswhite, H.M., Appl. Opt., 2 (1963) 675.

Volume 14, Number 3, 2021. pp. 209-220

Jordan Journal of Physics

ARTICLE

Passively Q - Switched Linear Cavity IR Fibre Laser *via* Nonlinear Polarization Rotation

Fadi Z. Qamar

Physics Department, Faculty of Sciences, Damascus University, Damascus, Syria.

Doi: **https://doi.org/10.47011/14.3.3**

Received on: 29/04/2020; Accepted on: 22/8/2020

Abstract: Setup for self-starting passive Q-switch operation of IR fibre laser *via* nonlinear polarization rotation (NPR) was demonstrated for the first time for linear cavity. A Q-switched pulse duration of ~ 600 ns, a maximum peak power of ~16 W and an average power of 408 mW have been obtained at 223 kHz repetition rate for 5.1 W pump power from 1319 nm CW Nd: YAG laser launched to ~ 2.78 m unidirectional single-clad Tm-doped silica fibre linear cavity using only flat polarizer and feedback mirror to induce NPR. The dependence of the fibre laser output characteristics on the polarization angle of the polarizer is also reported. However, self induced passive Q-switching in linear fibre laser cavities is only observed in fibres with angled cleaved ends and with lengths that are around the optimum length for CW operation.

Keywords: IR fibre laser, Passive Q-switching, Nonlinear polarization rotation, Linear cavity, Ring cavity.

PACS: Fiber lasers, 42.55.Wd, Q-switching, 42.60.Gd.

Introduction

Continuous wave (CW) and pulsed operations for fibre lasers operated near or amid IR have been demonstrated in various studies. The Q-switched fibre laser can be achieved actively or passively by various methods. These are by inserting: an acoustic optic or an electro-optic modulator inside the cavity of the laser [1 - 3] for actively Q-switched regimes or a saturable absorber (SA), such as transition metal doped crystal [4], FIrpic thin film [5], Europium Oxide (Eu_2O_3) [6] and semiconductor saturable absorber mirror [7], to achieve passive Q-switching operation. Q-switched fibre lasers using fibre-based SAs, such as carbon nano-tube [8 - 11], graphene [12], mismatch of mode field areas and a saturable-amplifier pump switch [13] and unpumped active fibre [14], have been also reported. Nonlinear polarization rotation (NPR) effect in fibre laser ring cavities with different designs has also been widely used to initiate and shape the pulses in Er-doped fibre lasers [16 - 18]. In fact, the NPR technique can produce intensity-dependent optical transmission by a self-phase modulation mechanism, thus providing an artificial saturable absorption effect in fibre lasers' cavity [17]. The saturable absorption strength can be adjusted by simply rotating a polarization wave plate. The NPR can also induce spectral filtering effect to achieve wave length tuneable passively mode-locked pulse [16]. Recently, a passively Q-switched all-fibre ring laser operating at 1949 nm, which is based on a nonlinear polarization rotation (NPR) technique using a 2 m long thulium-doped fibre and a 15 m long thulium-ytterbium co-doped fibre as active media, was reported [18]. However, self-start Q-switch operation *via* nonlinear polarization rotation (NPR) has not been achieved yet, to the best of our knowledge, in linear cavity fibre lasers.

Corresponding Author: Fadi Z. Qamar **Email**: fadiqamar@Hotmail.com

In this paper, a complete novel experimental demonstration and theoretical explanation of self-start Q-switching in linear fibre laser cavities were presented. A new and simple method to obtain stable self-start Q-switched output of a Tm^{3+}- doped silica fibre laser in linear cavity is illustrated. This method is based on inserting a plane polarizer inside the fibre cavity. The dynamic behaviour of the output, in this case, depends on the polarization angle of the polarizer and can vary between unstable self-pulsing to stable CW and finally to the requirement-stable self-start passive Q-switching by rotating the polarizer.

Experimental Techniques and Details

The experimental arrangement of the PQS is shown in Fig. 1.

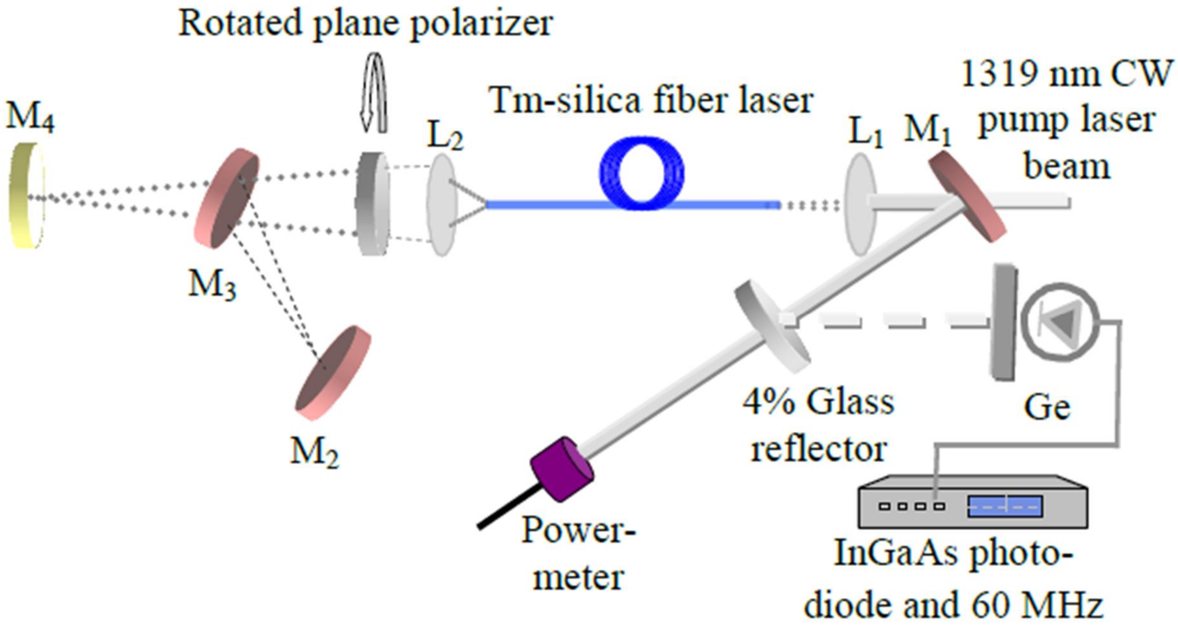

FIG. 1. PQS experimental arrangement of fibre laser pumped by solid-state laser, where M_1 is a 95 % T at 1.319 µm mirror, M_2 is a 45 deg. mirror that is HR at 1.8 - 2.1 µm and HT at 1.3 µm, M_3 is HR at 1.8 - 2.1 µm, M_4 is HR at 1.3 µm for feedback mirror and L_1 and L_2 are objective lenses.

The active medium of the cavity was a Tm-silica fibre laser cavity which operated at 2µm. The silica fibre had a core diameter of 16 µm and NA of 0.25 and was Tm-doped with a concentration of 1.1 % w. t. (7000 ppm molar). The silica fibre laser was pumped by 1.319 µm CW TEM_{00}, which is the output of Nd: YAG laser. A 7.5 mm focal length objective lens of NA = 0.25 was used to launch the pump light into the fibre. The measured launch efficiency was greater than 60 %. The cavity contained three high reflectance (HR) mirrors, M_1, M_2 and M_3. M_1 Mirror is highly transmitting (HT) at 1.3 µm and highly reflecting (HR) over the wavelength range of 1.8 - 2.1 µm. The mirror was positioned at 45 degrees to the beam axis and was used to separate the 2 µm beam from the pump. Another objective lens was used to re-launch the laser light reflected from the M_2 and M_3 mirrors into the distal facet of the fibre, where the mirror M_2 is HR over 1.8 - 2.1 µm and with high transmission (HT) at 1.3 µm, positioned at 45 degrees to the beam axis and mirror M_3 is 99 % HR over 1.8 - 2.1 µm. Therefore, the cavity was effectively formed by 4 % Fresnel reflection and two HR mirrors at 2 µm. Another mirror M_4, HR at 1.3 µm, was used to reflect back the pump light into the cavity in order to increase the cavity gain. A CaF_2 plane polarizer fixed to a rotation stage was inserted in-between the objective lens and the mirror M_2 to control the losses inside the cavity. The polarizer has a maximum transmission of ~80% at lasing wavelength and can operate over a wavelength range of 1- 2.4 µm with the degree of polarization > 98% at 2µm. The maximum power available was ~ 5.1 W and it reduced to ~ 4.8 W after the input mirror M_1 and the objective lens. The power launched into the fibre was ~ 3 W and the lasing threshold was about ~ 0.6 W. The maximum power available without the polarizer in the cavity was 523 mW without feedback from M_4 and ~ 600 mW with feedback, while the output dropped to 450mW when the polarizer was present in the cavity and feedback applied. Various fibre lengths were used of 1.95, 2.78 and 5.67 m and it was found that the optimum length for output power was in the range between 2.7 and 2.9 m. Careful cleaving of the ends of the fibre and accurate alignment have been adopted to achieve maximum power from the system. The operating parameters were measured, such as the relation between the input and the output powers, from which the launch efficiency, laser threshold and slope efficiency have been determined. The output with a centre wavelength of 1.95 µm was detected by a photodiode (Hamamatsu G8422 - 05) with a cut-off frequency of 80 MHz and a rise time of 4.37 ns.

Passive Q-Switching Operation in Linear Cavity

The temporal profile of the output of the 2.78 m Tm doped fibre laser without the polarizer placed in the cavity showed that the output was a stable CW when the un-pumped end of the fibre was cleaved normally with respect to the fibre optical axis (Fig. 2a), while the output became quasi-CW when the fibre was angled cleaved with $\theta \approx 8$ deg. with respect to the normal on the optical axis of the fibre (Fig. 2b). The maximum output power for both cases was 530 mW. When feedback from M_4 mirror was applied, the quasi-CW output changed to self-pulsing with a maximum power of 572 mW for both angled cleaved fibre (Fig. 2c) and normally cleaved fibre (Fig. 2d).

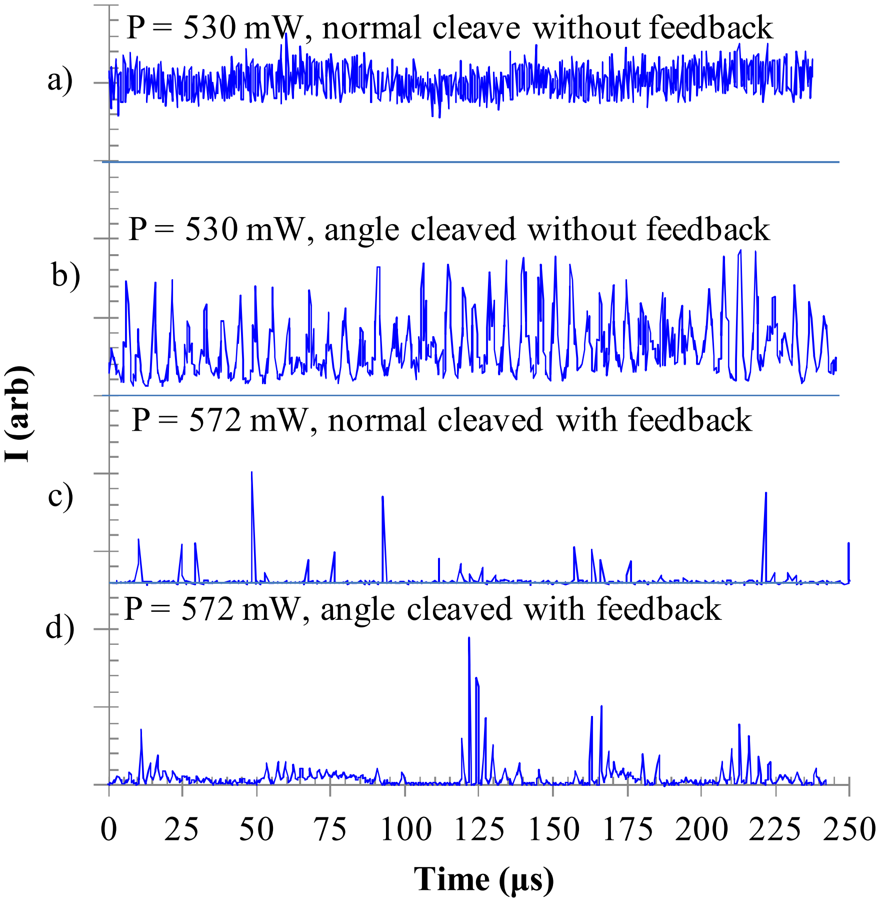

FIG. 2. Temporal behaviour for several cavity arrangements without in-cavity polarizer: a) normal cleaved fibre, blocked feedback pumping from mirror M_4 b) angled-cleaved fibre, blocked feedback pumping from mirror M_4, c) feedback from mirror M_4 for angle cleaved fibre d) feedback from mirror M_4 for normally cleaved fibre.

With the normally cleaved fibre, the two Fresnel reflections for both ends of the fibre (i.e., 4 % reflections) were enough to create about 220 mW self-lasing output in the fibre, which increased to 530 mW when feedback was provided from both the high-reflectance mirrors M_2 and M_3. This output power varied between a minimum power of 267 mW followed by a maximum power of 442 mW and then another minimum of 358 mW when in-cavity polarizer was set at angles of θ = 0, 45 ° and 90°. The temporal profile of the output beam in Fig. 3 shows no significant changes in CW operation related to the changes in the rotation angle of the polarizer. However, it is clear from Fig. 3 that the fluctuation of the CW temporal profile is output power-dependent.

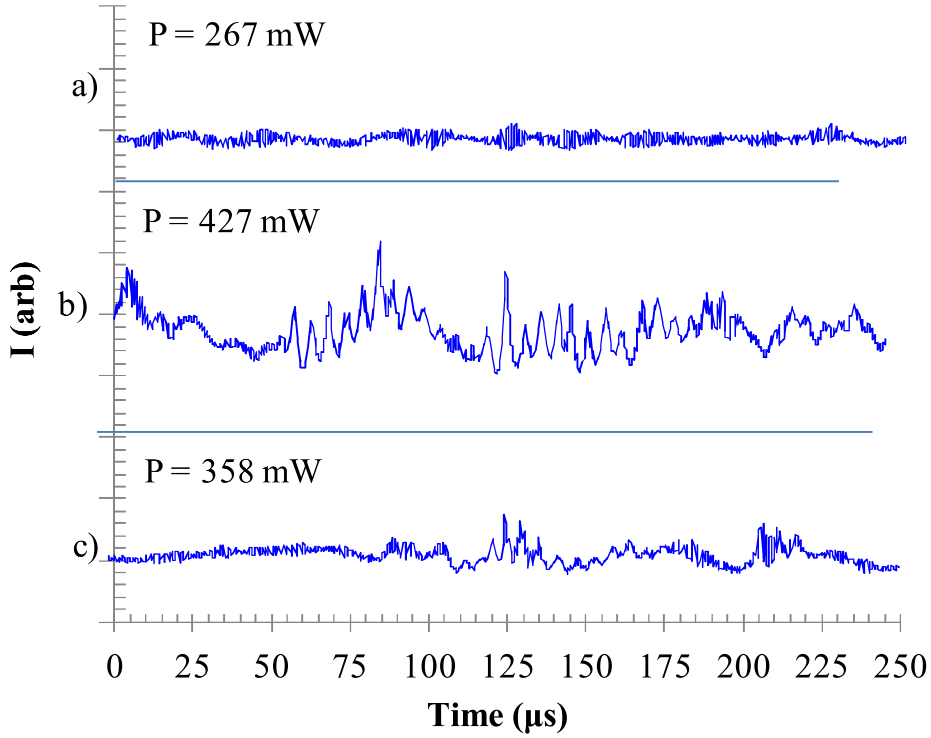

FIG. 3. Laser intensity time dependence for normally cleaved fibre for 3 orientation angles Φ of the intra-cavity polarizer. a) Φ = 0˚, b) Φ = 45˚, c) Φ = 90˚.

When the fibre was angled cleaved at an angle equal to ~ 8°, feedback from M_2 and M_3 mirrors was required in order to generate laser action in the cavity. With the cube polarizer in the cavity and set to give minimum output power, a power of 109 mW CW was obtained, Fig. 4a. Rotating the polarizer resulted in an increase of the output power, while no significant change was found in the temporal behaviour of the laser output until the output increased to 356 mW and the temporal behaviour now was quasi - CW, Fig. 4b. Further rotation of the polarizer leads to further increase in output power and the temporal dynamics of the output are now unstable with a self-pulsing output power of 409 mW, Fig. 4c. Increasing the rotation angle further, the output power reduced again, but became more stable; i.e., CW output with a maximum power of 405 mW, Fig. 4d. A minimum value of output power of 300 mW was obtained and the output at this power was unstable self-pulsing, Fig. 4e. The output power increased on further rotation of the polarizer until it reached a maximum power of ~ 435 mW and the output was now a stable passive Q-switched pulse train with a peak power of 12.7 W and a pulse duration of 733 ns at 211 kHz repetition rate, Fig. 4f. Further rotation of the polarizer decreased the output power again until another minimum was reached and the output became unstable self-pulsing.

Setting the polarizer to achieve the maximum power gave a temporal profile of the output which was passive Q-switching. The input power was varied down to the threshold lasing of the system. Fig. 5 shows that self-Q-switching occurred at all applied pump powers.

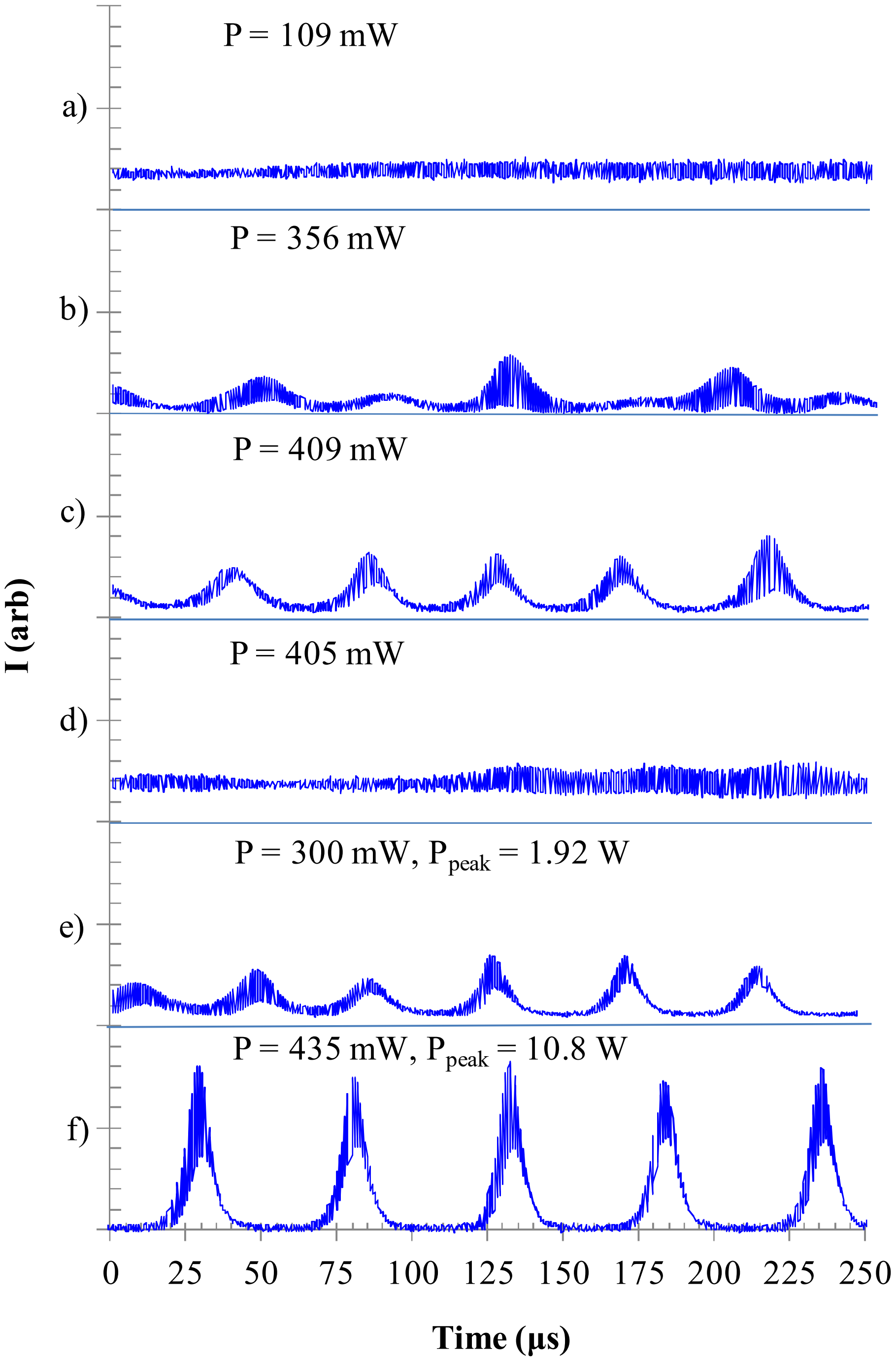

FIG. 4. Dynamics of normally cleaved fibre end with different orientation angles of the intra-cavity polarizer, resulting in: a) CW operation at minimum output power, b) Quasi-CW operation at higher power, c) Self-pulsation at maximum power, d) CW when the power is decreased, e) Chaotic self-pulsation when the output power decreased to the minimum, f) Self-Q-switching when the power is increased to maximum again.

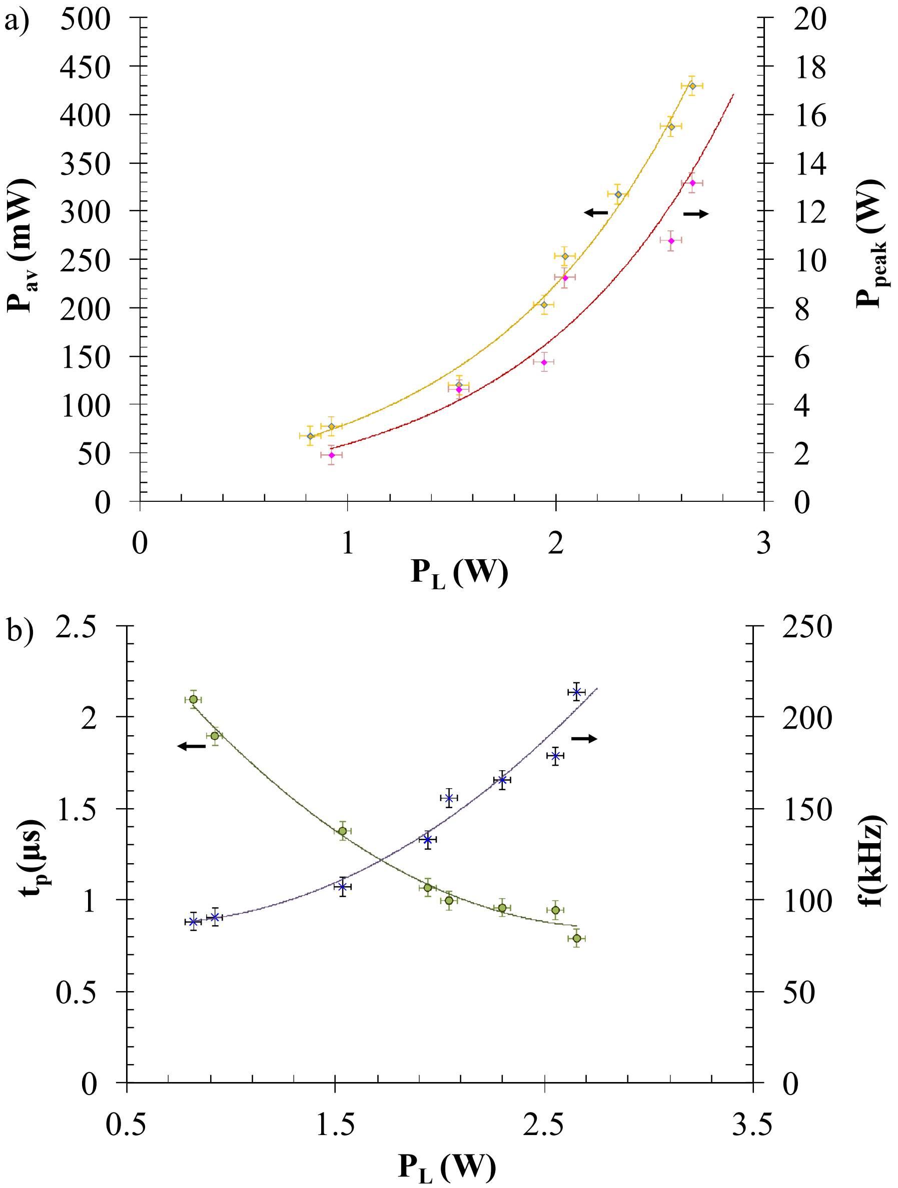

FIG. 5. Self-Q-switching for various pump powers down to the threshold pumping.

The relation between the average output power and the peak power of the Q-switched pulses as a function of launched power is shown in Fig. 6a. Both average power and peak power increased with increase in the launched power. Additionally, Fig. 6b shows that the frequency of the self-start Q-switched pulses increased while the pulse duration decreased for increase in launched power. These results agreed with ones represented in a previous work that has been done in ring cavity for the same wavelength [18].

The dependences of the passive Q-switched profile and the dynamics of the fibre output on the fibre length were investigated. For a short fibre, 1.95 m (Fig. 7a), the dynamics was quasi -CW when the polarizer has been adjusted to give maximum power extracted from the cavity. However, self-start Q-switching or stable CW has not been observed at any rotation angle of the polarizer. Similarly, a long fibre of 5.67 m showed no effect of rotating the angle of the polarizer on the dynamic behavior (Fig. 7c). The output in this case was CW at any rotation angle of the polarizer. In contrary, a ~16 W maximum peak power and 408 mW average power self-start Q-switching pulse train with duration up to ~ 600 ns at ~ 223 kHz repetition rate (i.e., 4.48 µs time interval between the pulses) had been observed for an optimum fibre length of 2.78 m when the system was operated in Q-switch regime (Fig. 7b). Self-mode-locking with ~ 100 % modulation depth was also perceived within the observed Q-switching pulses.

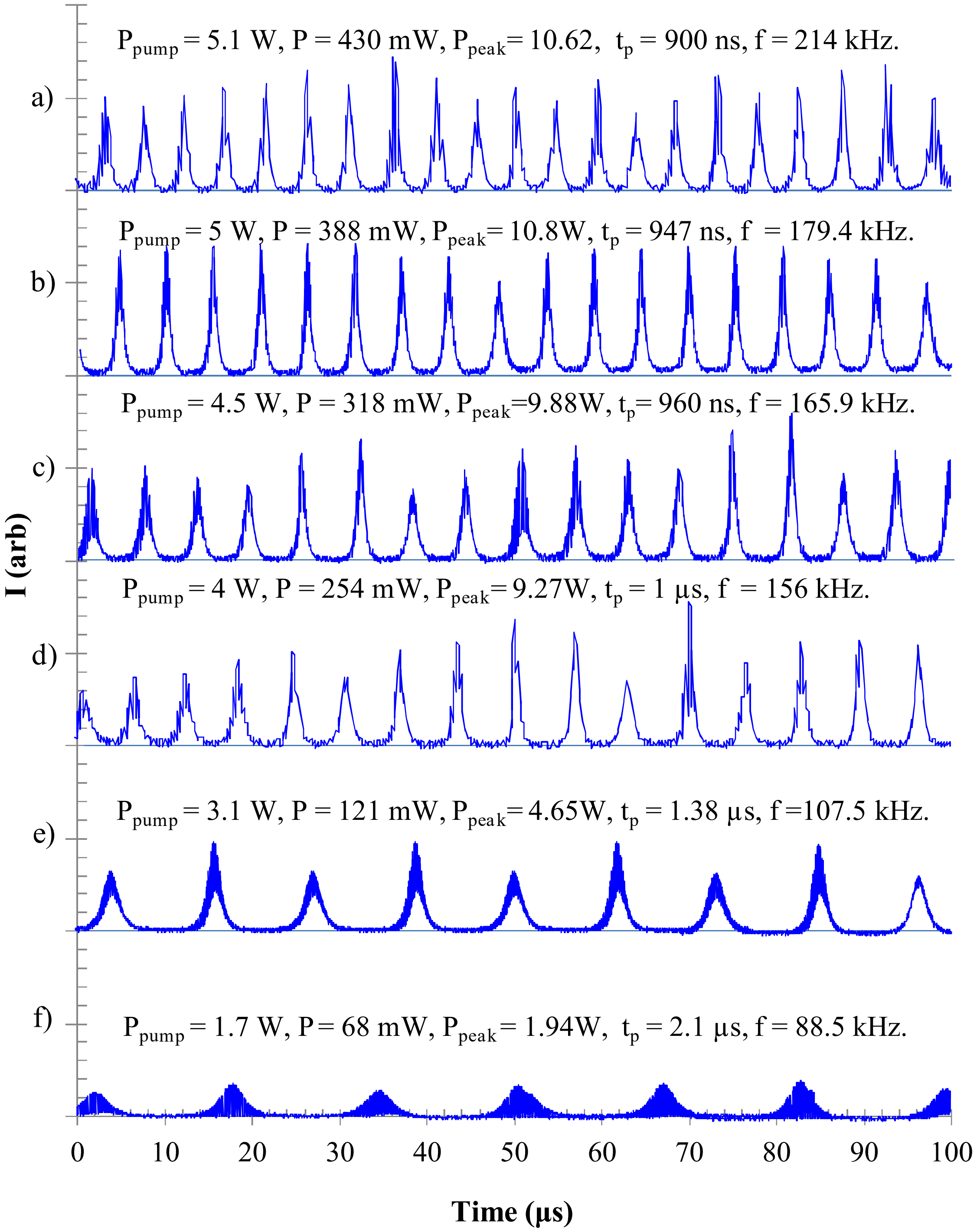

FIG. 6. Output characterization for increasing launched power in the self-start Q-switched regime. a) Average output power and individual peak pulse power as a function of launched pump power, b) The frequency and the pulse duration as a function of launched pump power for fibre length of = 2.78 m.

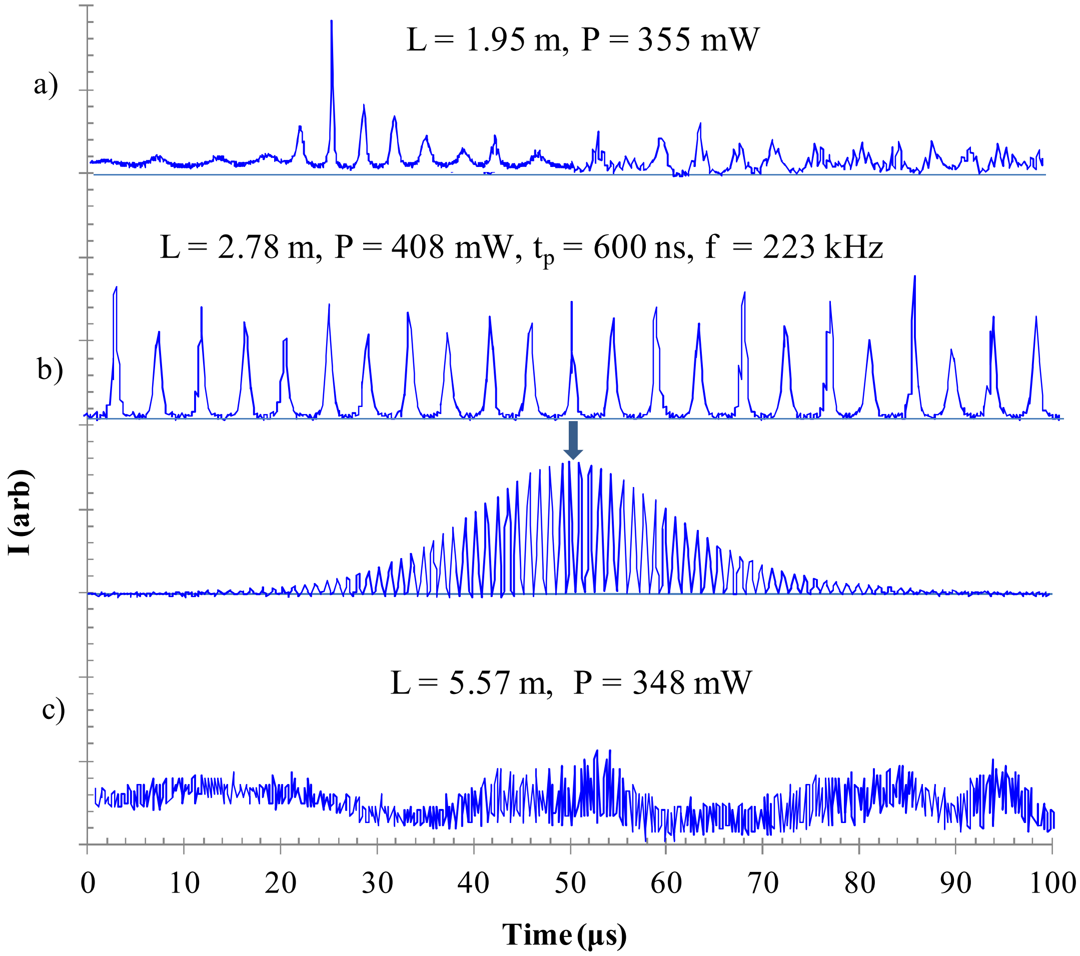

FIG. 7. Temporal evolution of the intensity for: a) Minimum output from 1.95 m fibre, b) Maximum output from 2.78 m fibre and the self-mode-locking inside the pulse, c) Minimum output from 5.67 m fibre.

The dependence of the dynamics of the output on the orientation angle of the polarizer in this investigation is summarized in Fig. 8. However, the two consecutive lower peaks in all parts of Fig. 8 have different amplitudes, which indicates that the intra-cavity laser light beam is more likely elliptically polarized with large and small components (radii) parallel to the axis of the fibre. However, it can be deduced from Fig. 8 that at an orientation angle of the polarizer equal to 90°, only one component (i.e., the larger component as the low peak in this case is higher than the lower next one) passes through the polarizer and is launched back to the fibre and because it was already parallel to one axis of the fibre, only one polarization will propagate inside the fibre resulting in CW output. The same scenario will repeat after 90° (i.e., for an orientation angle of the polarizer at 180°), while the smallest will pass through the polarizer to launch back to the fibre resulting in CW output, but with lower power compared with the previous case. In contrast, if the polarization angle of the launched back beam is not parallel to the one axis of the fibre (i.e., the orientation angle of the polarizer should be between m π° and (2m+1) π/2°, where m is an integer number), the linear polarization will split into two components when it propagates inside the fibre and the beam becomes elliptically polarized with a different angle than the initial one, resulting in NPR. The effect of NPR increases as the orientation angle of the polarizer increases until reaching the maximum effect at an angle equal to m π/4, where the two components of linear polarization of the launched back beam on the entrance face of the fibre become equal. The output in this case is more likely QS.

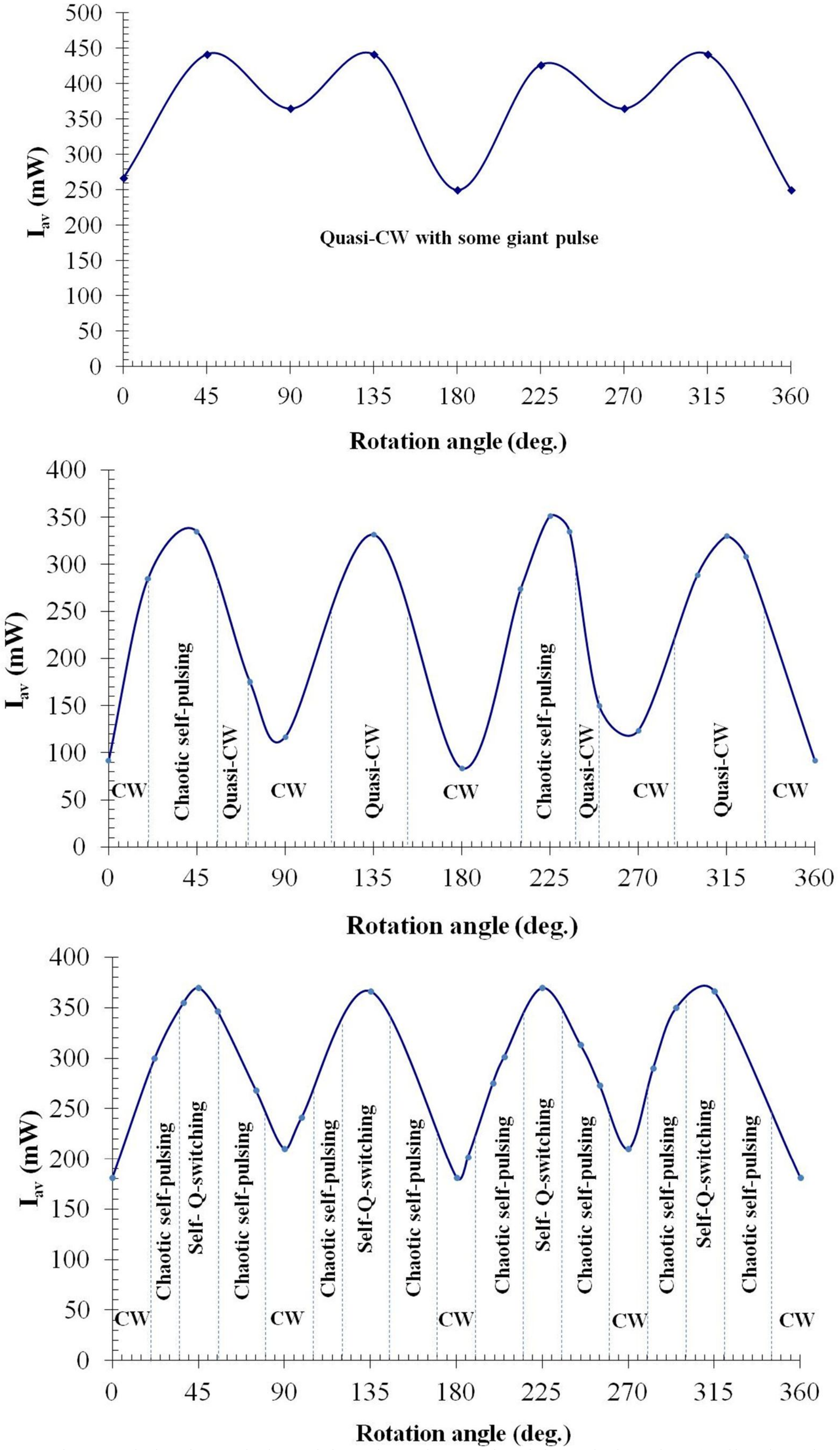

FIG. 8. Output characteristics for variation of the orientation angle of the polarizer for: a) Fibre length of ~ 2.9 m (which resulted in optimum output power) with flat cleaved end, b) Fibre length of 2.5 m with angled cleaved end. c) Fibre length of ~ 2.8 m (which resulted in optimum output power) with angled cleaved end.

Discussion

NPR is a phenomenon that results from the changes in the direction of light polarization inside the laser cavity. These changes are due to self-phase modulation (SPM) and cross-phase modulation (XPM) in addition to some birefringence of the fibre [19]. Those nonlinear effects which cause rotation of light in fibre were exploited to enable intensity modulation mechanism in the laser cavity. The NPR - based Erbium - doped fibre laser (EDFL) relies on the Kerr effect that creates inside the fibre in conjunction with an optical isolator to produce a pulse by setting the initial polarization state to elliptical. This elliptical state can be resolved into right- and left-hand circular polarization components of different intensities when launched to the fibre. As a result, an elliptically polarized pulse will have its x and y components experience different phase shifts, thus rotating the polarization ellipse.

The light separates inside the fibre into two orthogonal polarized lights; E_x and E_y. After passing through the fibre, both E_x and E_y accumulate nonlinear phase shift due to the SPM and XPM effects in the fibre. The angle of polarization can be changed from α_1 to α_2 as the light propagates through the fibre. Here, α_1 is the angle between the polarization direction of the laser beam and the fast axis of the fibre and α_2 is the angle between the fast axis of the fibre and the polarizer direction (Fig. 9). The beam transmission is described using the following equation [20, 21]:

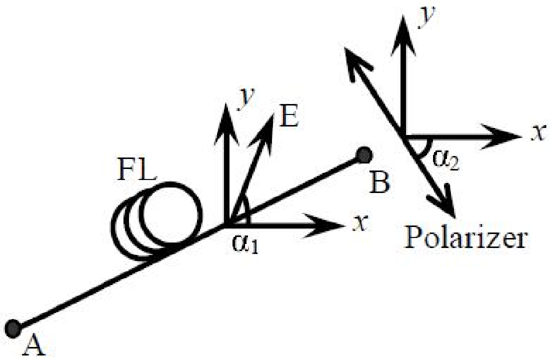

FIG. 9. Polarization directions at A and B ends of the fibre laser (FL) for NPR operation, where E: electrical vector of laser beam; x and y: fast and slow axes of the fibre, respectively [20].

$$T = cos^2\alpha_1 cos^2\alpha_2 + sin^2\alpha_1 sin^2\alpha_2 + (1/2)\, sin2\alpha_1 sin2\alpha_2 \cos(\Delta\varphi_L+\Delta\varphi_{NL}) \quad (1)$$

where $\Delta\varphi_L$ is the linear phase shift from modal birefringence and $\Delta\varphi_{NL}$ is the nonlinear phase shift contributed by both SPM and XPM effects. $\Delta\varphi_L$ *and* $\Delta\varphi_{NL}$ are calculated from:

$$\Delta\varphi_L=(2\pi L/\lambda)\ (n_y-n_x) \quad (2)$$

$$\Delta\varphi_{NL}=(2\pi n_2 PL/\lambda A_{eff})\ cos2\alpha_1 \quad (3)$$

where n_y *and* n_x are the refractive indices of the respective fast and slow axes of the optical fibre, L is the fibre length, λ is the operating wavelength, n_2 signifies the nonlinear refractive index, P is the instantaneous peak power of the input signal, while A_{eff} is the effective core area. The angle α_2 can be manipulated by rotating the polarizer to obtain the maximum modulation, which makes the system act as an artificial saturable absorber, which leads to PQS. The PQS starts to weaken and disappear if the polarization angle of the incident beam differs from π/4 in respect to fibre fast axis. The reason for this is that decreasing or increasing the rotation angle to approach 0° or π/2 will minimize the modulation term (third tem) in Eq. 1 and the output is then quasi - CW and becomes CW for a rotation angle making α_2 equal to 0° or π/2 and the third term equal to zero.

However, another experiment was carried out using Tm fibre laser linear cavity with only an internal plane polarizer to induce the self-starting of PQS operation in fibre laser. Before starting conducting the second PQS experiment, it was too important to stabilize the output of the fibre. Two different methods to stabilize the output of a Tm-doped silica laser have been developed here before doing PQS experiment. The first method relied on enhancing the feedback from the un-pumped end of a unidirectional pumped fibre by using a normally cleaved fibre end, while the second method was based on using an angled cleaved fibre and modulating, the losses inside the cavity with an intra-cavity polarizer. The 4 % reflection from the fibre end created self-lasing in the fibre even without using any HR coupler. This self-lasing helped stabilize the output and make any extra losses in the external cavity formed by an intra-cavity polarizer or any other sources insufficient to affect the dynamic behaviour of the output.

The self-lasing power perhaps plays the same role as using resonant pumping [22] to stabilize the output of the fibre laser. However, re-launching the pump power again to the cavity using mirror M_4 enhances both the saturable absorber effects in the un-pumped end of the fibre and the pump noise which might be reasons for unstable self-pulsing operation of the laser [23, 24]. Angled cleaving of the distal facet of the fibre suppresses any feedback and stabilizes the output and as a consequence the output becomes unstable-self-pulsing. With an angled cleaved fibre, the cavity is more sensitive to any extra modulation that occurs in the cavity by external modulations. When the polarizer is placed in the angled cleaved fibre cavity, the loss in the cavity is increased; these losses are due to two factors, a) the transmission losses of the polarizer substrate material, b) polarization losses dependent on the angle between the polarizer and intra-cavity laser, assuming that the laser output generated by the fibre is generally partially polarized. The unequal lower peaks in Fig. 8 indicate that this fibre is birefringent and the fast axis is in y direction (i.e., at $\pi/2^\circ$). However, the horizontal polarization is more enhanced when the fibre end angle is cleaved, which will improve more with an angle closer to Brewster's angle. On the other hand, when the partially polarized beam exiting from the far end of the fibre cavity passes through the polarizer, it becames perfectly polarized at $\pi/4^\circ$. The beam is then reflected back to the polarizer by the 2 rear mirrors and can pass through the polarizer without any change, as there is no change in the polarization direction. The polarized beam is then launched back to the fibre and because of the polarization direction at $\pi/4^\circ$ in respect to fibre axis, the beam splits inside the fibre to two equal perpendicular components. As before in the ring cavity, for an angle of $\pi/4^\circ$, the transmission from Eq. 1 will be:

$$T= - (1+ (1/2) \cos (\Delta\varphi_L + \Delta\varphi_{NL})) \quad (4)$$

This equation indicates that the modulation in this case is maximum, which induces PQS operation. Since the PQS operation depends only on the rotation angle phenomenon, it will be pump power-independent and that is what the experimental studies confirm in Fig. 5. Rotating the polarizer by another $\pi/4^\circ$ deg. (i.e., the direction of the polarizer in this case is at 0 or $\pi/2^\circ$) allows the polarization to transmit through the polarizer after second path (i.e., after being reflected from the rare mirror) with a direction at an angle of 0 or $\pi/2^\circ$, which will be parallel or perpendicular to the optical fibre axis and therefore only one beam propagates inside the fibre and the modulation term in Eq. 3 will equal zero resulting in pure CW. The temporal evolution of the output then favours an unstable output, ranging between quasi - CW and self-pulsing, depending on the angle between the laser and the plane surface of the polarizer, as shown in Fig. 8b and c. It is clear that the scenario repeats itself with the rotation of the polarizer by $\pi/2^\circ$ degrees and again the output changes depending on the interference from CW to quasi - CW with chaotic self-pulsing and PQS to quasi - CW with chaotic to CW again. In contrast with the first experiment, self-lasing occurs in this type of fibre for flat cleaved end. Fig. 8a shows no PQS for this case and indicates that it is important to eliminate any scattering and self - lasing beams to be created in the cavity in order to achieve the polarization rotation state that is necessary to produce PQS. This can be done by angle cleaved fibre laser end. However, self-start passive Q-switched pulsed output was obtained at nearly optimum length of the fibre, as the very long fibre will affect the polarization direction and lead to more un-polarized beam at its far end, while high dynamics in the short one due to strong pumping will also affect the polarization state of the beam and prevent complete modulation. Finally, no PQS is obtained when a horizontally polarized 1064 nm laser pumped this fibre. Pumping the fibre with polarized 1064 nm laser light resulted in stable CW output even with an angled cleaved fibre. Thus, it can be deduced that pumping with polarized light or adjusting the polarization in the linear cavity so that only one polarization propagates inside the fibre, might play a role in reducing any loss due to Brillouin scattering or any other scattering effects in the fibre that prevent PQS operation (no modulation loss can take place inside the fibre).

Conclusion

NPR technique was applied to create a PQS train pulse in linear fibre laser cavity. A train of pulses with time duration of 4.48 μs, pulse width of around 600 ns, average power of 408 mW at 1.9 μm from Tm-DFL pumped by 1319 nm a Nd: YAG laser was obtained using NPR by means of only a plane polarizer. The comparison between the two techniques confirmed that starting PQS process depends on loss variation following nearly the same scenario depending on the polarizer or half-wave plate angle. It was demonstrated that, at a polarizer or half-wave plate angle of π/4° in respect to fibre axis, the elliptical polarization of the re-entering beam will rotate inside the fibre causing strong losses of modulation that lead to start PQS. However, other regimes like chaotic self-pulsation, quasi - CW or CW will take place for other rotation angles.

References

[1] Delgado-Pinar, M., Diez, A., Cruz, J. L. and Andres, M.V., Laser Phys. Lett., 6 (2009) 139.

[2] Kuznetsov, A.G. and Babin, S.A., Laser Phys., 20 (2010) 1266.

[3] Chen, N.K., Feng, Z.Z. and Liaw, S.K., Laser Phys. Lett., 7 (2010) 363.

[4] Filippov, V.N., Starodumov, A.N. and Kir'yanov, A.V., Opt. Lett., 26 (2001) 343.

[5] Salam, S., Al-Masoodi, A.H.H., Al-Hiti, A.S., Al-Masoodi, Ab.H.H., Wang, P., Wong, W.R. and Harun, S.W., Optical Fiber Technology, 50 (2019) 256.

[6] Zulkipli, N.F., Jafry A.A.A., Apsari, R., Samsamnun, F.S.M., Batumalay, M., Khudus, M.I.M.A., Arof, H. and Harun, S.W., Optics & Laser Technology, 127 (2020) 106163.

[7] Huang, J.Y., Huang, S.C., Chang, H.L., Su, K.W., Chen, Y.F. and Huang, K.F., Opt. Express, 16 (2008) 3002.

[8] Zhou, D.P., Wei, L., Dong, B. and Liu, W.K., IEEE Photon. Technol. Lett., 22 (9) (2010) 9.

[9] Dong, B., Hao, J., Hu, J. and Liaw, C.Y., IEEE Photon., Technol. Lett., 22 (2010) 1853.

[10] Chernysheva, M., Mou, C., Arif, R., AlAraimi, M., Rümmeli, M., Turitsyn, S. and Rozhin, A., Scientific Reports, 6:24220 (2016) 1.

[11] Zulkifli, M.Z., Muhammad, F.D., Mohd Azri, M.F., Mohd Yusof, M.K., Hamdan, K.Z., Samsudin, S.A. and Yasin, M., Results in Physics, 16 (2020) 102949.

[12] Luo, Z., Zhou, M., Weng, J., Huang, G., Xu, H., Ye, C. and Cai, Z., Opt. Lett., 35 (2010) 3709.

[13] Tsai, T.Y., Fang, Y.C., Lee, Z.C. and Tsao, H.X., Opt., Lett., 34 (2009) 2891.

[14] Kurkov, A.S., Sadovnikova, Ya.E., Marakulin, A.V. and Sholokhov, E.M., Laser Phys. Lett., 7 (2010) 795.

[15] Luo, Z.C., Liu, J.R., Wang, H.Y., Luo, A.P. and Xu, W.C., Laser Phys., 22 (2012) 203.

[16] Hamzah, A., Paul, M.C., Awang, N.A., Ahmad, H., Pal, M., Das, S., Ismail, M.A. and Harun, S.W., Opt. Laser Tech., 47 (2013) 22.

[17] Azooz, S.M., Harun, S.W., Ahmad, H., Halder, A., Paul, M.C., Das S. and Bhadra, S.K., Ukr. J. Phys. Opt., 16 (1) (2015) 37.

[18] Qamar, F.Z., Laser Phys., 28 (2018) 6.

[19] Lin, Q. and Agrawal, G.P., IEEE J. of Quant. Electron., 40 (7) (2004) 958.

[20] Feng, X., Tam, H. and Wai, P., Optics Express, 14 (18) (2006).

[21] Luo, Z., Luo, A., Xu, W., Song, C., Gao, Y. and Chen, W., Laser Physics Letters, 6 (8) (2009) 582.

[22] Loh, W.H., Optics Letters, 21 (10) (1996) 734.

[23] Barn1enkov, Y.O. and Kir'yanov, L.A.V., Optics Express, 12 (14) (2004) 3171.

[24] Kellou, A., Amroun, D. and Sanchez, F., Journal of Modem Optics, 45 (9) (1998) 1951.

Volume 14, Number 3, 2021. pp. 221-230

Jordan Journal of Physics

ARTICLE

Investigating the Effect of Nitro Groups on the Electronic Properties of Phenanthrene Compound

Haider O. Essa[a] and **Satha M. Abbas**[b]

[a] *Biology Department, Science College, Al-Qasim Green University, Al-Qasim Town, Babylon Province, 51013, Iraq.*

[b] *Chemistry and Physiology Department, Veterinary Medicine College, Al-Qasim Green University, Al-Qasim Town, Babylon Province, 51013, Iraq.*

Doi: **https://doi.org/10.47011/14.3.4**

Received on: 13/05/2020; Accepted on: 13/9/2020

Abstract: Theoretical study for calculating the electronic structure of phenanthrene compound and its simplest derivatives with nitro groups in different positions was performed using density functional theory (DFT) based on the hybrid function of three parameters. Lee-Yang-Parr [B3LYP] with 6-31 [d, p] basis set was used to investigate the effect of nitro groups on the electronic properties of phenanthrene compound. All calculations were obtaind by employing the used method using the Gaussian 09 package of programs. The energy gaps, total energies, the energy of HOMO and LUMO, softness, dipole moment, Fermi level, molecular symmetry, electrochemical hardness, electron density, electrostatic potential surfaces and infrared spectra were calculated. The results showed that the electronic properties of phenanthrene molecule are affected by the added nitro group. The total energy, energy gap and the HOMO and LUMO energy decreased compared with the original molecule. The ionization potential (IP), electron affinity (EA) and Fermi level (Ef) are increased compared with the original molecule.

Keywords: B3LYP/DFT calculations, Phenanthrene molecule, Nitro group, Energy gap, Ionization potential.

Introduction

Polycyclic aromatic hydrocarbons (PAHs) are a large group of organic compounds with two or more combined aromatic rings. PAHs are mainly generated as a result of pyrolysis processes, especially incomplete combustion of organic matter during industrial and other human activities, such as coal and crude oil processing, natural gas combustion including for heating, waste combustion, vehicle movement, cooking and smoking, as well as in natural processes, such as carbonation [1, 2]. Cytotoxicity is one of several important biological effects of polycyclic aromatic hydrocarbons. Therefore, many intensive efforts have been made for the discovery and development of new cytotoxic molecules [3, 4]. The PAH phenanthrene was studied in this paper. Phenanthrene is the simplest non-linear polycyclic aromatic hydrocarbon with three benzene ring structure. It is a colorless crystal with luster and phenanthrene precipitated from ethanol is a colorless monoclinic crystal. It is a leaf-like crystal with a relative density of 1.179 (25/4 °C), a refractive index of 1.6450, a melting point of 101 °C and a boiling point of 340 °C. Though it can sublime, it is insoluble in water, slightly soluble in ethanol, soluble in ether, benzene, acetic acid, chloroform, carbon tetrachloride and carbon disulfide [5, 6]. Phenanthrene can be used in the manufacture of pesticides and dyes and can also be used in stabilizing high-efficiency and low-toxicity pesticides, as well as smokeless powder explosives [7]. Phenanthrene has an anti-cancer property against human colonnade

Corresponding Author: Haider O. Essa **Email**: headeromran@yahoo.com

epithelial cancer cell lines [8]. Due to the chemical and physical properties of the phenanthrene molecule, there are many studies on its electronic structure, where Ayşegül Gümüş *et al.* studied computationally a series of phenanthrene and phenanthroline derivatives to investigate their potential usage as organic solar cell components, thermally activated delayed fluorescence and nonlinear optic compounds [9]. Alan Hinchliffe *et al.* studied molecular polarizabilities for anthracene and phenanthrene [10] and P.L. de Andres *et al.* studied the electronic and geometrical structure of potassium-doped phenanthrene [11]. In the present work, we chose the effect of nitro groups, because nitro groups are organic compounds that contain one or more nitro functional groups ($-NO_2$) and are also strongly electron-withdrawing. Because of this property, C−H alpha bonds to the nitro group can be acidic [12]. Two nitro groups were used in the present work to achieve substitution patterns (Iso, Para, Meta). The main aim of this paper is to determine the effect of nitro groups on the electronic properties of phenanthrene compound by using density functional theory with 6-31G (d, p) basis set.

Theoretical Model

The electronic structure of organic compounds is essential to the realization of virtually all the properties of materials, including the arrangement of atoms and molecules, electronic properties, mechanical properties and thermodynamic properties [13]. Density functional theory (DFT) is a quantum mechanical method which can be applied to study the electronic structure for organic compounds. For the past 30 years, density functional theory has been the predominant method for the quantum mechanical simulation of periodic systems. In recent years, it has also been adopted by quantum chemists and is now widely applied for the simulation of energy surfaces in molecules [14, 15]. The electronic structure of phenanthrene compound has been studied by density functional theory (DFT).Three parameters B3LYP (Becke's three parameter exchange with Lee, Yang and Parr correlation functional) density functional theory with 6-31G (d, p) basis set [16-19] are used in this paper to perform the ground state calculations. Full geometry optimizations of phenanthrene molecule were drawn on Gauss View 5.0.8 [20] and relax using the Gaussian 09 package of programs [21], as shown in Fig. 1. The hybrid exchange-correlation functional B3LYP is very effective for computing the electronic properties of phenanthrene molecule, such as total energy, energy of HOMO and LUMO, energy gap, ionization potential (IP), electron affinity (EA), hardness (H) and softness (S) [22-24]. The total energy (E_T) clarifies the sum of potential energy and kinetic energy of the system [25, 26]. HOMO refers to the highest occupied molecular orbitals and LUMO symbolizes the lowest unoccupied molecular orbitals. The energy gap is the variation of the energies between the HOMO and LUMO levels [25, 27]. The ionization potential (IP) for a molecule is the magnitude of energy needed to separate an electron from an isolated atom or molecule; HOMO energy was also applied to calculate IP in the framework of Koopman's theorem $IP = - E_{HOMO}$ [28-30]. The LUMO energy was also applied to compute the electron affinity (EA) of a molecule according to Koopman's theorem $EA = - E_{LUMO}$ [28, 30, 31]. One of the global quantities is chemical potential (μ); it measures the escaping tendency of an electronic cloud and is defined by $\mu = (E_{HOMO} + E_{LUMO}) / 2$ [31]. The hardness (H) is a measurement of molecule resistance to the change or deformation and is defined by $H = (IP-EA)/2$ [31]. The global chemical softness (S) is a property of molecules that measures the extent of chemical reactivity. It is the inverse of hardness and is given as: $S = 1/2H$ [32, 33]:

Results and Discussion

In this section, we present the results of our work and discuss the electronic properties of phenanthrene molecule. Table 1 displays the energy gaps, electronic states such as the lowest unoccupied molecular orbital (LUMO) and the highest occupied molecular orbital (HOMO), total energies and the symmetry of structures for molecules studied.

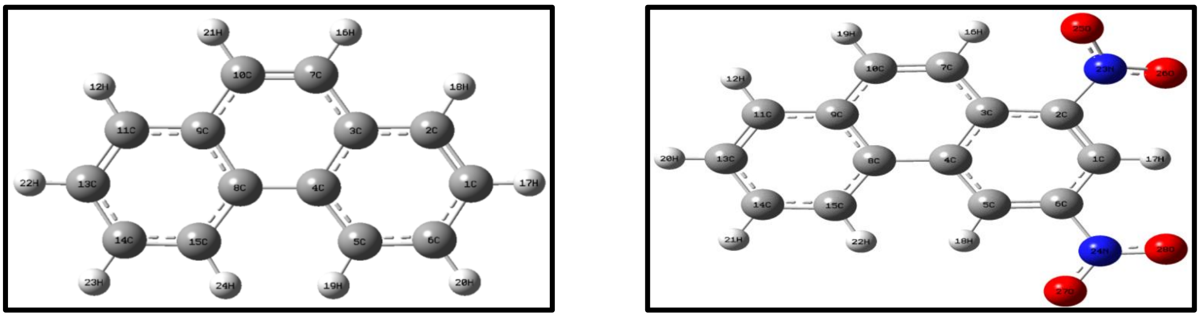

1 (Phenanthrene) **2 (2, 6 – dinitrophenanthrene)**

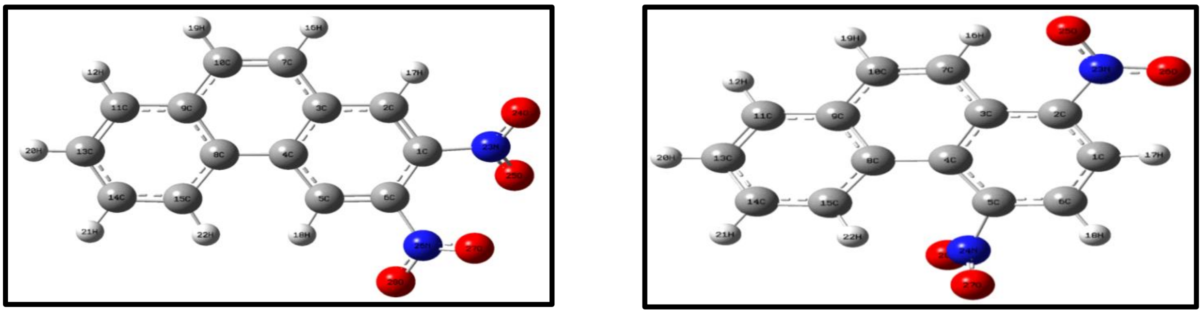

3 (1, 6 – dinitrophenanthrene) **4 (2, 5 – dinitrophenanthrene)**

FIG. 1. The optimized structures of phenanthrene molecule and its derivatives with nitro groups in different positions.

TABLE 1. Total energy, symmetry, HOMO – LUMO and energy gap for molecules.

Mol.	Total energy (a.u.)	Symmetry	HOMO (eV)	LUMO (eV)	HOMO (eV) [9]	LUMO (eV) [9]	Energy gap (eV)	Energy gap (eV) [9]
1	-539.419	C_1	-5.77118	-0.99239	–5.75	–1.01	4.778796	4.74
2	-948.247	C_1	-6.91867	-3.48382	-----	----	3.434845	----
3	-948.235	C_1	-6.90397	-3.35729	-----	------	3.546682	----
4	-948.227	C_1	-6.73799	-3.56845	-----	-----	3.169537	----

From Table 1, the electronic properties of phenanthrene molecule are affected by the addition of nitro groups, where the total energy, energy gap and the HOMO and LUMO energy decreased compared with the original molecule, as shown in Figs. (2-4), respectively. Decreasing the energy gap improves the conductivities and increases the solubility of these molecules. Also, it is clear from Table 1 that the total energy, energy gap and the HOMO and LUMO energy for all dinitrophenanthrene molecules are approximately pointing to the fact that the electronic properties are independent on the position of the nitro radical in the ring. The symmetry of the studied molecules is C1, meaning that the studied molecules have only one symmetry operation. Fig. (5) illustrates the 3-D distribution of HOMOs and LUMOs for the studied molecules.

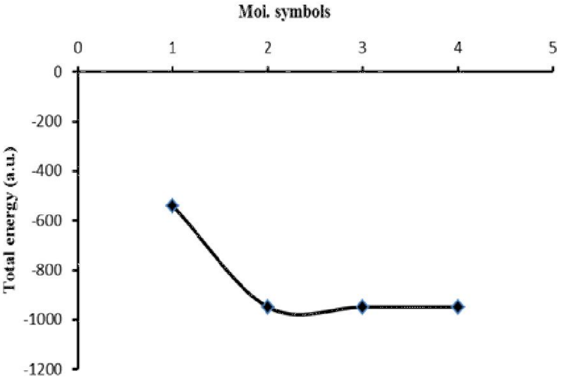

FIG. 2. The calculated total energy for molecules under study.

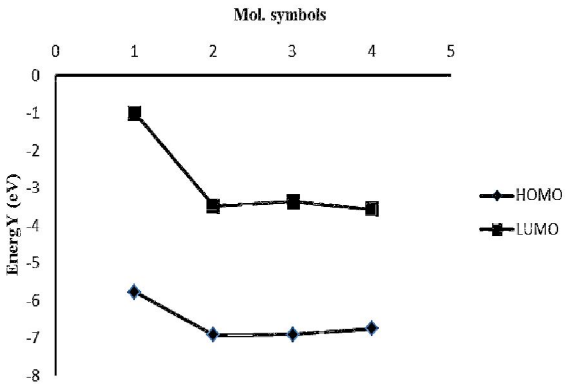

FIG. 3. The HOMO and LUMO energies for molecules under study.

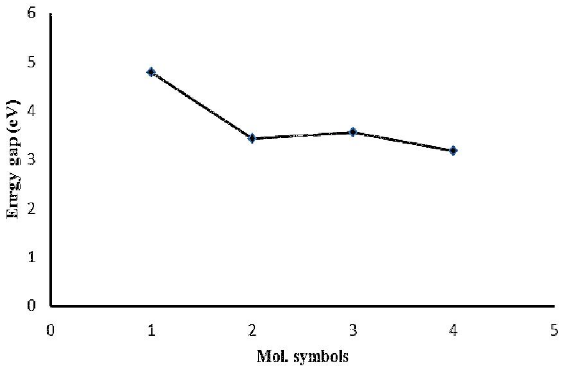

FIG. 4. The calculated energy gaps for molecules under study.

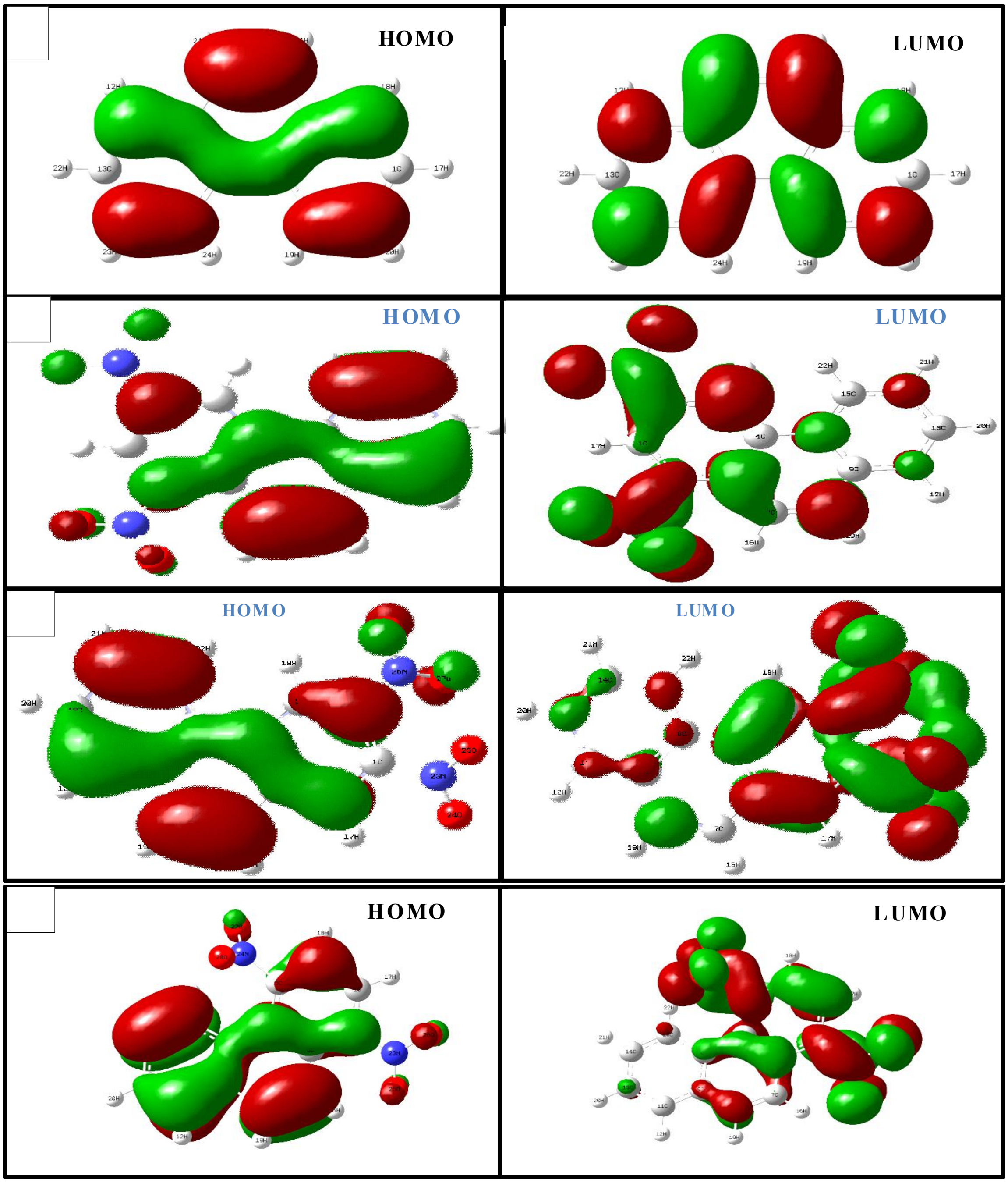

FIG. 5. HOMO and LUMO shapes of the phenanthrene and dinitrophenanthrene molecules.

Fig. 5 shows the electronic density distribution along the rings C-C. In the different parts of dinitrobiphenyl molecules, the electronic density distribution is homogeneous. It was noticed for all molecules that HOMO shows a bonding character and LUMO shows an antibonding character.

From Table 2, the ionization potential (IP), electron affinity (EA) and Fermi level (Ef) are affected by the addition of nitro groups, where they are increased compared with the original molecule, as shown in Figs. (6, 7), respectively. The ionization potential (IP), electron affinity (EA) and Fermi level (Ef) for all dinitrophenanthrene molecules are approximately the same, indicating that the electronic properties are independent on the position of the nitro radical in the ring. The softness (S) and hardness (H) values for all dinitrophenanthrene molecules are slightly lower comparable to original molecule, as shown in Fig. 8; this is because nearly all the usually used exchange-correlation functionals such as B3LYP, B3PW91 and Koopman's theorem, satisfy accuracy. Adding nitro groups leads to change the values of the dipole moment (μ), where the phenanthrene molecule has no dipole moment and is planar in space. Adding the subgroups leads to varying the symmetrical distribution of the electronic structure of the molecule, therefore changing the dipole moment, as shown in Fig. 9.

TABLE 2. The electronic properties of studied molecules.

Mol.	IP (eV)	EA(eV)	Ef (eV)	H (eV)	S (eV)	μ
1	5.771181	0.992385	6.267374	5.274988	2.637494	0.0341
2	6.918669	3.483824	8.660581	5.176757	2.588378	7.5606
3	6.903975	3.357293	8.582622	5.225328	2.612664	9.9884
4	6.737988	3.568451	8.522213	4.953763	2.476881	3.2225

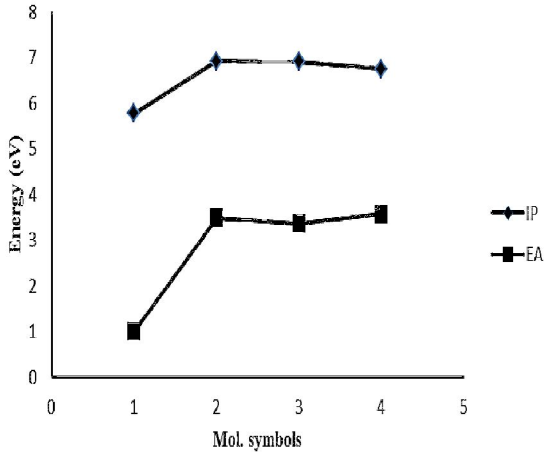

FIG. 6. The calculated ionization potential (IP) and electron affinity (EA) for molecules under study.

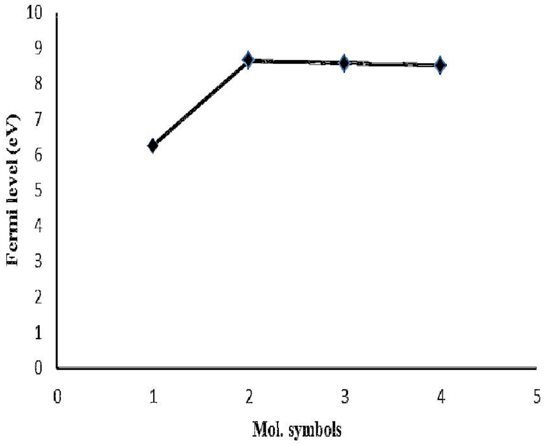

FIG. 7. The calculated Fermi level for molecules under study.

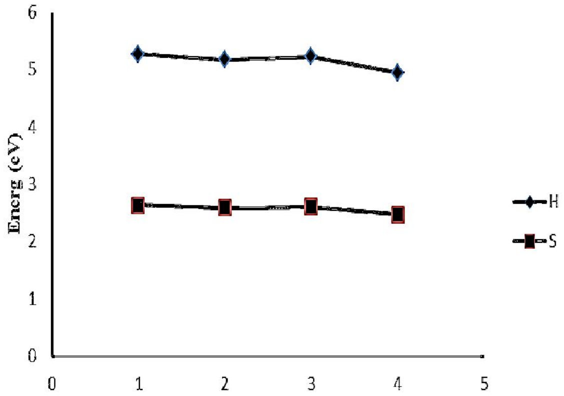

FIG. 8. The calculated hardness (H) and softness (S) for molecules under study.

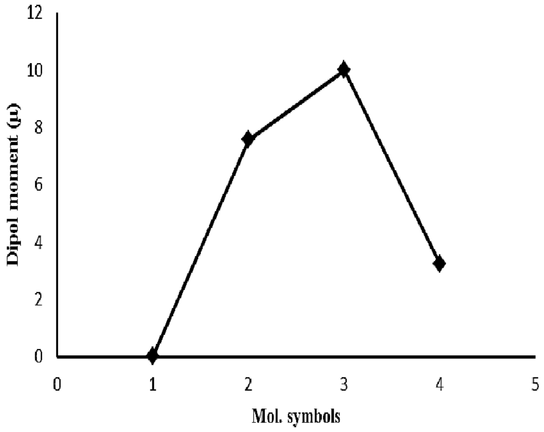

FIG. 9. The calculated dipol moment for molecules under study.

Electron Density Surface

Fig. 10 explains the three-dimensional shape of electron density distribution surface of phenanthrene and dinitrophenanthrene molecules, where the electron density was distributed due to the distribution of all atoms in the space of the complex according to the total density of the electrons in the complex. The total density is useful for understanding bonding and reactivity [34]. From this figure, it can be seen that the electron density distribution surface for the studied molecules is asymmetric, where the electron density is dragged towards the atoms of high electronegativity.

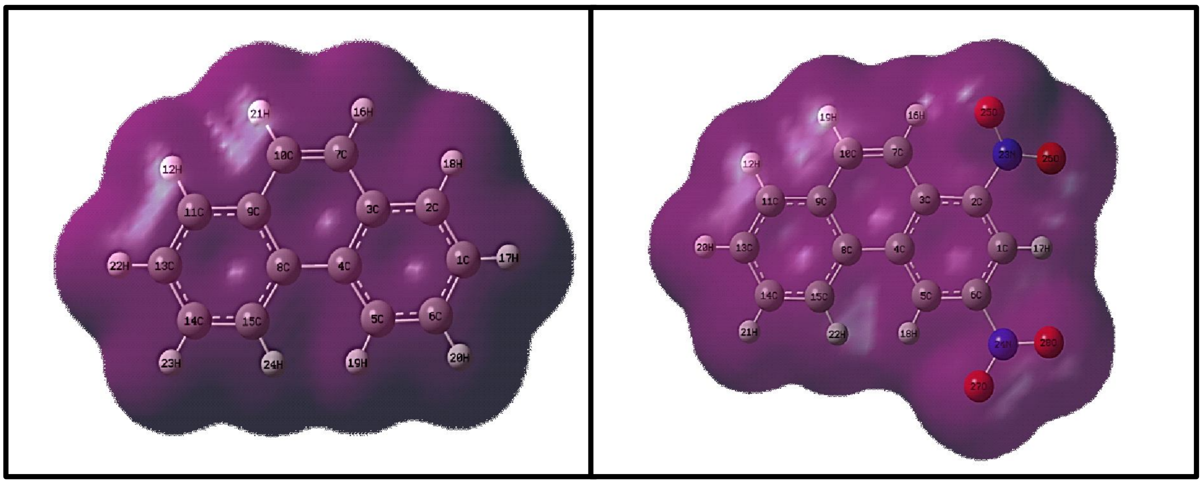

1 (Phenanthrene) **2 (2, 6 – dinitrophenanthrene)**

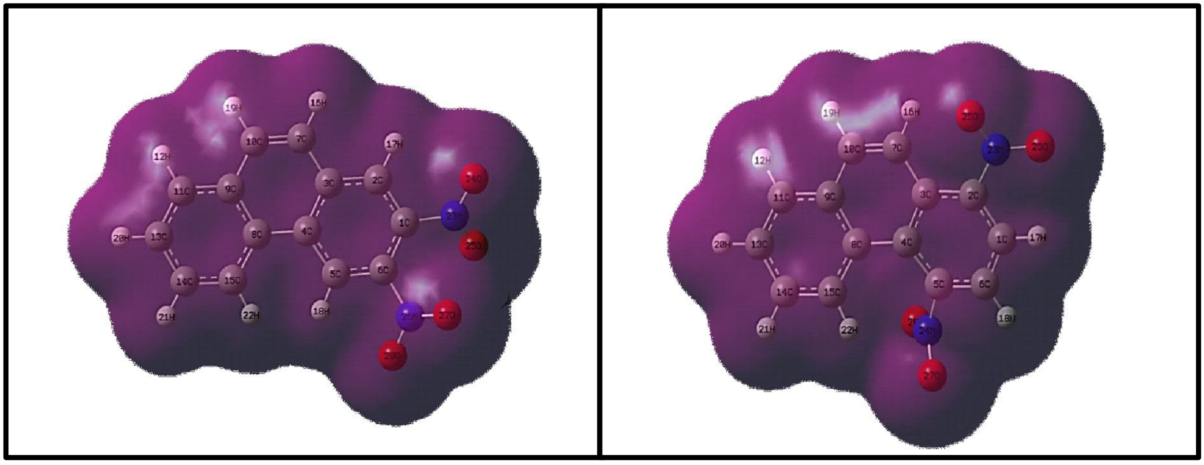

3 (1, 6 – dinitrophenanthrene) **4 (2, 5 – dinitrophenanthrene)**

FIG. 10. The electron density distribution for molecules under study.

Electrostatic Potential Surface

Fig. 11 explains the distribution of electrostatic potential, which depends on the negative and positive charges and depends also on the electronegativity of the atoms in the phenanthrene and dinitrophenanthrene molecules. In general, the electrostatic potential surfaces are dragged towards the atoms of high electronegativity.

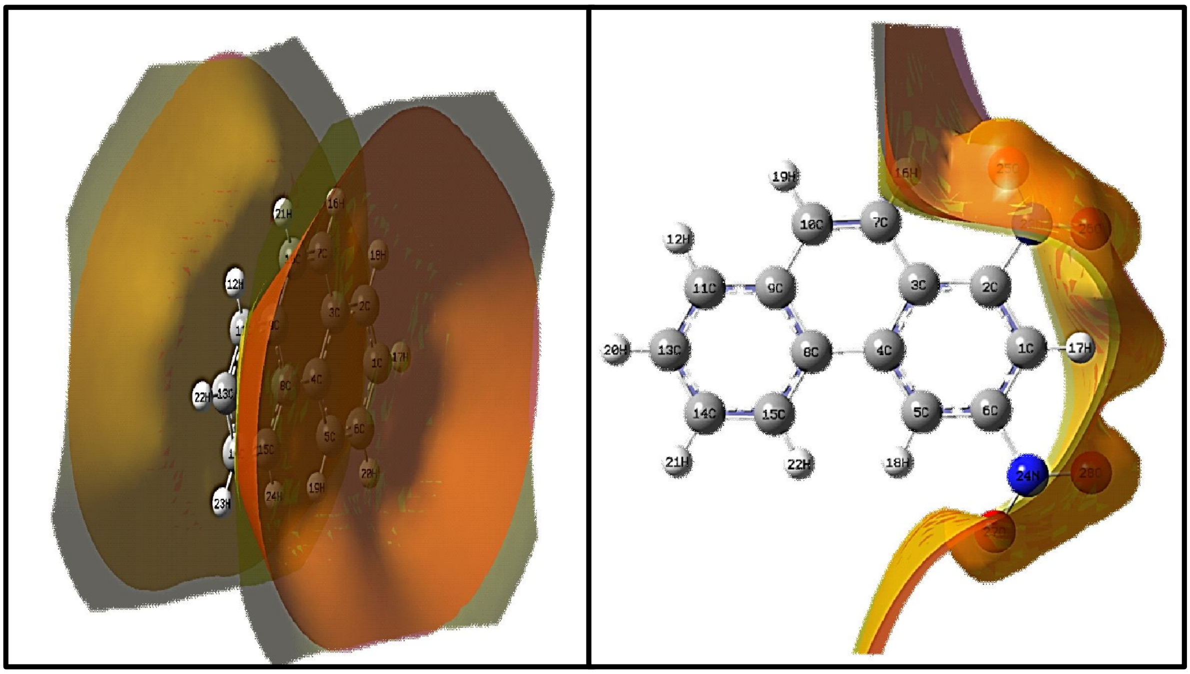

1 (Phenanthrene) **2 (2, 6 – dinitrophenanthrene)**

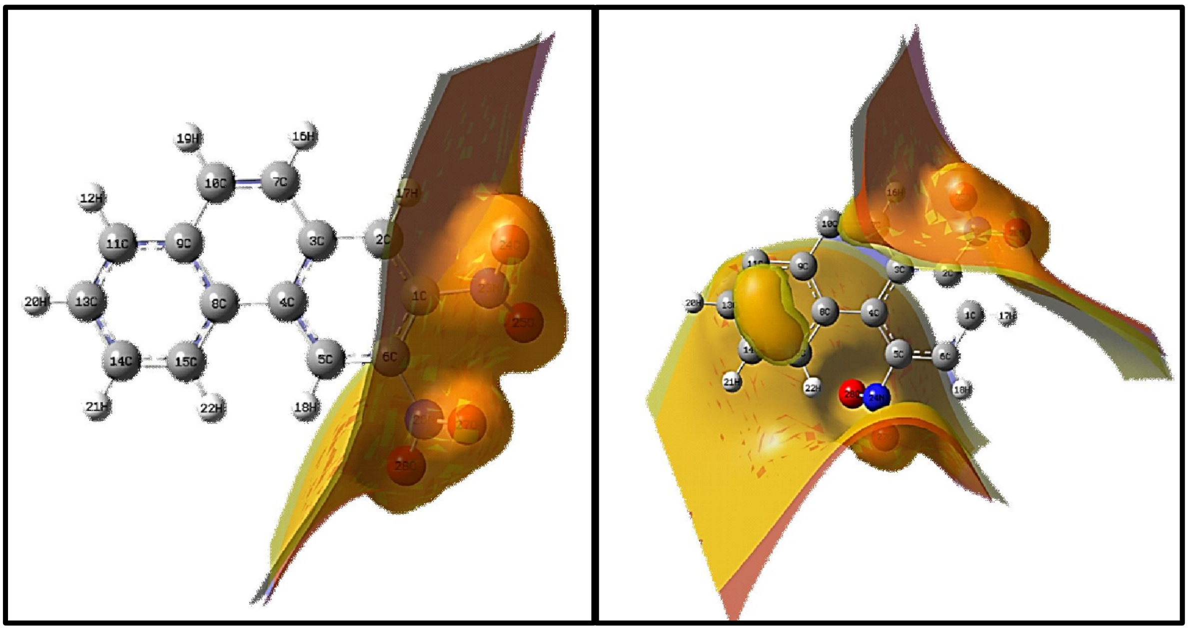

3 (1, 6 – dinitrophenanthrene) **4 (2, 5 – dinitrophenanthrene)**

FIG. 11. The electrostatic potential surfaces for molecules under study.

Infrared Spectra

Fig. 12 shows the computed IR spectra for phenanthrene and dinitrophenanthrene molecules. The harmonic vibrational frequencies were calculated for the studied molecules by using B3LYP level with a 6-31G basis set. The substitution of hydrogen atoms by NO_2 leads to increasing the number of vibrational modes. According to the rule of (3N-6), the phenanthrene molecules have 66 degrees of freedom, while the dinitrophenanthrene molecules have 78 degrees of freedom. All degrees of freedom for phenanthrene **1** and its derivatives **2-4** are represented by stretching, bending, rocking and scissoring modes. The (C – H) stretching vibrations of aromatic molecules are characteristic in the region (2900–3250) cm^{-1} which is a characteristic region for ready identification of (C – H) stretching vibrations and particularly the region (3250–3100) cm^{-1} for asymmetric stretching and (3100–2900) cm^{-1} for symmetric stretching modes of vibration [35]. For a phenanthrene molecule, the (C–H) stretching has been studied around 3197.81 cm^{-1}. The (C-C) stretching vibrations have been studied in the region 1681.13 cm^{-1}. Also, Figure (12) shows the IR spectrum of dinitrophenanthrene molecules **2-4** which has new peaks in the vibration modes in comparison with phenanthrene molecule **1,** due to the existence of stretched bonds, such as (C-N), (C-H) and (N-O) for **2-4** molecules. The stretching of (C-H) has been observed in the range of 3285.46-3293.51 cm^{-1}. The (C-N) stretching has been observed in the region 1656.08-1134.30 cm^{-1}, whilst the stretching of (C-C) bond is shown in the range of 1675.12-1661.38 cm^{-1} and the stretching of (N-O) bond is shown in the region 1493.81-1352.20 cm^{-1}.

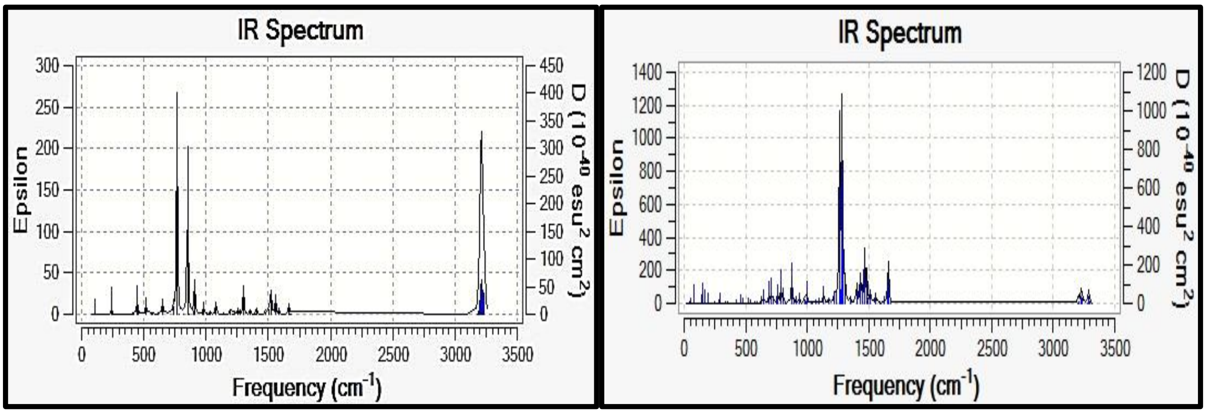

1 (Phenanthrene) **2 (2, 6 – dinitrophenanthrene)**

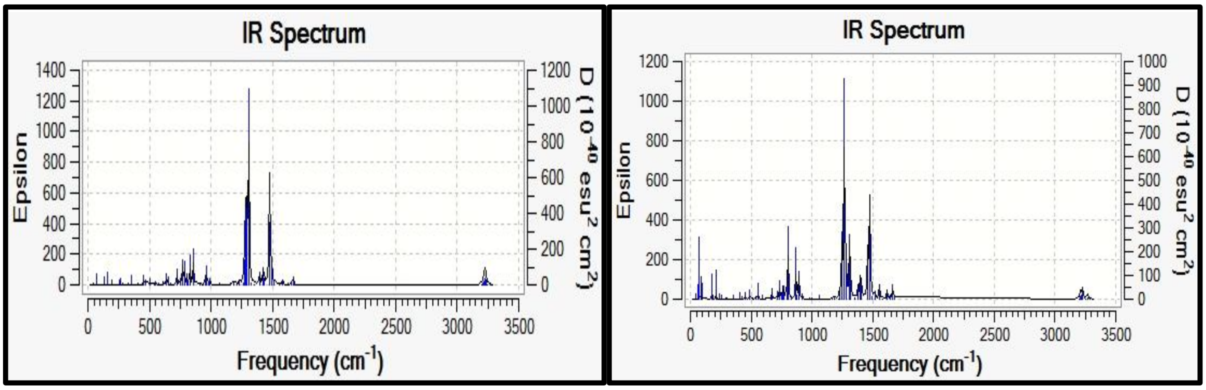

3 (1, 6 – dinitrophenanthrene) **4 (2, 5 – dinitrophenanthrene)**

FIG. 12. The calculated IR spectral frequencies for molecules under study.

Conclusions

Density functional [B3LYP/6-31 G(d, p)] theoretical methodology has been concerned with the determination of geometrical and energetic features in order to identify the factors influencing the values of ionization potential and electron affinity computed by orbital vertical theory (Koopman's theorem). Also, electronic properties, such as total energy, HOMO and LUMO energies, energy gap, chemical hardness, softness, dipole moment, electron density surface, electrostatic potential surface and spectroscopic properties such as IR spectra were investigated for the phenanthrene and dinitrophenanthrene molecules. The addition of nitro groups affected the electronic structure of phenanthrene molecule, where the total energy energy gap and the HOMO and LUMO energy, decreased compared to the original molecule and the ionization potential (IP), electron affinity (EA) and Fermi level (Ef) show an increase compared with the original molecule. The electronic properties are independent on the position of the nitro radical in the ring. Electron density and electrostatic potential surfaces are dragged towards atoms of high electronegativity. The substitution of hydrogen atoms by NO_2 led to an increase in the number of vibrational modes.

References

[1] Danzon, M.A., "Air Quality Guidelines", 2nd edition, (WHO Regional Office for Europe, Copenhagen, Denmark, 2000).

[2] Lerda, D., "Polycyclic aromatic hydrocarbons (PAHs) factsheet", 4th edition, (European Union, 2011).

[3] Zhang, H.Z., Kasibhatla, S., Kuemmerle, J., Kemnitzer, W., OllisMason, K., Qiu, L., Crogan-Grundy, C., Tseng, B., Drewe, J. and Cai, S.X., J. Med. Chem., 48 (2005) 5215.

[4] Mattson, M.P., Brain Pathol., 10 (2000) 300.

[5] Singh, L., Varshney, J.G. and Agarwal, T., Food Chemistry, 199 (2016) 768.

[6] de Azeredo, S.O.F. and Figueroa-Villar, J.D., World Journal of Pharmacy and Pharmaceutical Sciences, 3 (11) (2014).

[7] Samimi, S.V., Akbari Rad, R. and Ghanizadeh, F., Iran J. Environ. Health Sci. Eng., 6 (1) (2009) 47.

[8] Guedouar, H., Aloui, F., Beltifa, A., Ben Mansour, H. and Ben Hassine, B., C. R. Chimie, 20 (2017) 841.

[9] Gümüş, A. and Gümüş, S., Macedonian Journal of Chemistry and Chemical Engineering, 36 (2) (2017) 239.

[10] Hinchliffe, A. and Soscun Machado, H.J., Int. J. Mol. Sci., 1 (2000) 8.

[11] de Andres, P.L., Guijarro, A. and Verges, J.A., "Instituto de Ciencia de Materiales de Madrid (CSIC)", (28049 Madrid, Spain, 2018).

[12] Ju, K.-S. and Parales, R.E., Microbiol. Mol. Biol. Rev., 74 (2) (2010) 250.

[13] Irene, E.A., "Electronic Materials Science", (John Wiley & Sons, Inc., Hoboken, New Jersey, 2005).

[14] Fitts, D.D., "Principles of Quantum Mechanics As Applied to Chemistry and Chemical Physics", (Cambridge University Press, New York, 2002).

[15] Rogers, D.W., "Computational Chemistry Using the PC", 3d Edition, (John Wiley & Sons, Inc., Hoboken, New Jersey, 2003).

[16] Reimers, R.J., "Computational Methods for Large Systems: Electronic Structure Approaches for Biotechnology and Nanotechnology", (John Wiley & Sons, Inc., Hoboken, New Jersey, 2011).

[17] Jones, R.O., Reviews of Modern Physics, 87 (2015) 897.

[18] Sahni, V., "Quantal Density Functional Theory II: Approximation Methods and Applications", (Springer Verilog, Berlin, Heidelberg, 2010).

[19] Stephens, P.J., Devlin, F.J., Chabalowski, C.F. and Frisch, M.J., The Journal of Physical Chemistry, 98 (43) (1994) 11624.

[20] Roy, D.D., Todd, A.K. and John, M.M., "Gauss View 5.0.8. Gaussian", (Gaussian, Inc., Wallingford, 2009).

[21] Frisch, M.J., Trucks, G.W., Schlegel, H.B. et al., "Gaussian 09, Revision A.02", (Gaussian, Inc., PA, Wallingford CT, 2009).

[22] Engelberts, J., Havenith, R., Van Lenthe, J., Jenneskens, L. and Fowler, P., Inorg. Chem., 44 (2005) 52266.

[23] Santos, J.C.J., Andres, A., Aizman, P. and Fuentealba, J., Chem. Theory Comput., 1 (2005) 83.

[24] Santos, J.C., Tiznado, W., Contreras, R. and Fuentealba, P., J. Chem. Phys., 120 (2004) 1670.

[25] Nagarajan, V. and Chandiramouli, R., International Journal of Chem. Tech. Research, 6 (1) (2014) 21.

[26] Zarkadoula, E.N., Sharma, S., Dewhurst, J.K., Gross, E.K.U. and Lathiotakis, N.N., Physical Review A, 85 (2012) 1.

[27] Zhuo, L.G., Liao, W. and Yu, Z.X., Asian Journal of Organic Chemistry, 1 (2012) 336.

[28] Zhan, C., Nichols, J.A. and Dixon, D.A., Journal of Physics and Chemistry A, 107 (2003) 4184.

[29] Karzazi, Y., Belghiti1, M.E., El-Hajjaji, F. and Hammouti, B., Journal Mater. Environ. Sci., 7 (10) (2016) 3916.

[30] Hinchliffe, A., "Molecular Modelling", (John Wiley & Sons, Ltd., England, 2003).

[31] Mueller, M., “Fundamentals of Quantum Chemistry: Molecular Spectroscopy and Modern Electronic Structure Computations”, (Kluwer Academic/ Plenum Publishers, New York, 2001).

[32] Abel Kolawole, O. and Banjo, S., Analytical & Bioanalytical Electrochemistry, 10 (1) (2018) 136.

[33] Reyes, R.V. and Aria, A., Journal Ecl. Quim., Sao Paulo, 33 (3) (2008) 69.

[34] Cramer, C.J., “Essentials of Computational Chemistry”, (John Wiley & Sons, Ltd., USA, 2004).

[35] Sadasivam, K. and Kumaresan, R., Computational and Theoretical Chemistry, 963 (2011) 227.

Volume 14, Number 3, 2021. pp. 231-238

Jordan Journal of Physics

ARTICLE

Pressure and Temperature Effects on the Magnetic Properties of Donor Impurities in a GaAs/AlGaAs Quantum Heterostructure Subjected to a Magnetic Field

Samah F. Abu Zaid, Ayham Shaer, Eshtiaq Hjaz, Mahmoud Ali and **Mohammad K. Elsaid**

Department of Physics, Faculty of Science, An-Najah National University, Nablus, West Bank, Palestine.

Doi: **https://doi.org/10.47011/14.3.5**

Received on: 09/06/2020; Accepted on: 30/8/2020

Abstract: The exact diagonalization method has been used to solve the effective-mass Hamiltonian of a single electron confined parabolically in the GaAs/AlGaAs quantum heterostructure, in the presence of a donor impurity and under the effect of an applied uniform magnetic field. The donor impurity is located at distance (d) along the growth direction which is perpendicular to the motion of the electron in a two-dimensional heterostructure layer. We have investigated the dependence of the magnetization (M) and magnetic susceptibility (χ) of a GaAs/AlGaAs quantum heterostructure nanomaterial on the magnetic field strength (ω_c), confining frequency (ω_o), donor impurity position (d), pressure (P) and temperature (T).

Keywords: Exact diagonalization, Donor impurity, Magnetic field, Magnetization, Magnetic susceptibility, Pressure and temperature.

1. Introduction

The recent physical and technological research on nanosystems (low-dimension systems), such as quantum well (QW), quantum well wire (QWW) and quantum dot (QD) in theoretical and applied physics, play significant roles in the present quantum electronic nanodevices [1, 2]. The electrical, optical and transport properties of the heterostructures QW, QWW and QD are very sensitive to adding external electrical field, magnetic field and to different parameters, like pressure, temperature, and shallow donor impurities near the heterostructure surface [3, 4]. The study of quantum dots is motivated by their applications in solar cells, quantum computers, single electron transistors and lasers [5].

Furthermore, the donor impurity effects on the properties of the low-dimensional semiconductor heterostructure have been among the interesting problems to study in low-dimensional semiconductors, where adding the donor impurity atoms to low-dimension systems changes the effective charge and mass of them [6]. In addition, the most interesting phenomenon is to investigate the effects of temperature and pressure on the donor impurity binding energy in reduced dimensions [7], where the energy gap of the heterostructure changes because of the binding energy of the impurity and the Columbic interaction between the system charge carriers and the donor impurity [8, 9]. The donor impurity binding energy was investigated for all heterostructure systems, where it depends on the dimensionality of the system, the impurity position, the presence of magnetic or electrical fields, pressure and temperature [1, 10-12].

Corresponding Author: Mohammad K. Elsaid **Email**: mkelsaid@najah.edu

Different methods have been used to solve the system's Hamiltonian with the presence of the donor impurity, like variational and analytical methods under the presence of electric or magnetic fields for different shapes and donor impurity locations [13-18].

The dependence of the photoionization of impurities in infinite-barrier quantum wells on the photon energy had been calculated as a function of quantum well width [19]. In addition, the thermodynamic properties of quantum dots in a magnetic field, such as magnetization, magnetic susceptibility and specific heat, had been computed. For Helium-like confined quantum dots, the thermodynamic properties show sharp peak structure in the susceptibility and the specific heat curves [20]. The pressure and temperature dependence of the diamagnetic susceptibility and the binding energy of the donor impurity had been shown analytically, where the diamagnetic susceptibility increases as the pressure increases and decreases as the temperature increases [21]. Peter in Ref. [22] used the variation method to show the behavior of the binding energy levels of shallow hydrogenic impurities in a parabolic quantum dot with pressure. He found that the ionization energy is purely pressure-dependent. In addition, the binding energy of hydrogenic impurities, in a spherical quantum dot, was calculated using the variational and perturbation approaches as a function of pressure, QD size and impurity position. It was found that the pressure effect is enhancing the binding energy [23]. Using exact diagonalization method, including the pressure and temperature effects, the two electrons QD problem had been solved, where the magnetization and magnetic susceptibility of confined electrons in parabolic quantum dot were investigated in both experimental and theoretical studies [24, 25]. Recently, the electronic, thermodynamic and magnetic properties of two electrons confined in a single quantum dot and coupled quantum dots (CQD) had been also solved [26-34].

The purpose of this work is to investigate the combined effects of pressure, temperature and impurity position on the magnetic properties of GaAs/AlGaAs heterostructure material. The magnetization and magnetic susceptibility of a confined electron presented in a magnetic field are computed and displayed as function of the Hamiltonian system physical parameters. The structure of this paper is organized as follows: First, the Hamiltonian theory, as well as the computation diagonalization technique of a single electron in GAs/AlGaAs heterostructure in the presence of donor impurity located at a finite distance along the growth (z-axis) are discussed. Magnetization and magnetic susceptibility expressions and pressure and temperature material parameters relations used in the present calculations are given in Section 2. The numerical results and discussion are given in Section 3. Final section is devoted to the conclusion.

2. Theory

This section presents the main parts of the donor impurity formalization: i) The effective-mass Hamiltonian (EM) of donor impurities in quantum heterostructure, ii) The exact diagonalization method, iii) The magnetization and the magnetic susceptibility and iv) The effects of pressure and temperature.

A quantum heterostructure is a two-dimensional (2D) system where electrons are confined in the x-y plane with parabolic confinement potential of the form, $\frac{1}{2}m^*\omega_0^2\rho^2$ with confining strength ω_o and bound to off-plane donor impurity located at the z axis. The impurity position vector is (0, 0, d), where d is the distance from the two –dimensional heterostructure plane to the impurity center. A pictorial view of the electron in the xy-plane interacting with the donor impurity at the z axis is given by Alfonso *et al.* in Ref. [35]. This system is subjected to a uniform external magnetic field of strength B directed along the z direction. The magnetic field is given by $\mathbf{B}=\boldsymbol{\nabla}\times\boldsymbol{A}$, where $\mathrm{A}=\frac{B}{2}\,(-y,x)$ is the vector potential.

The Hamiltonian operator of the donor impurity, in effective Bohr radius (a^*) and Rydberg (R^*) units, is given as, [32, 35]:

$$\hat{H} = -\left(\rho^{-1/2}\frac{\partial^2}{\partial\rho^2}\rho^{1/2} + \frac{1}{\rho^2}\left(\frac{\partial^2}{\partial\phi^2}+\frac{1}{4}\right)\right) + \frac{1}{4}\omega^2\rho^2 - i\frac{\omega_c}{2}\frac{\partial}{\partial\phi} - \frac{2}{|\boldsymbol{\rho}-\mathbf{d}|} \qquad (1)$$

The given Hamiltonian ($\hat{\mathrm{H}}$) in Eq.1, given in terms of ρ and φ variables, can be separated into two parts as:

$$\hat{H} = \hat{H}_{\perp} + V(\rho) \qquad (2)$$

where:

$$\hat{H}_\perp = -\left(\rho^{-1/2}\frac{\partial^2}{\partial\rho^2}\rho^{1/2} + \frac{1}{\rho^2}\left(\frac{\partial^2}{\partial\phi^2}+\frac{1}{4}\right)\right) + \frac{1}{4}\omega^2\rho^2 - i\frac{\omega_c}{2}\frac{\partial}{\partial\phi} \tag{3}$$

and

$$V(\rho) = -\frac{2}{|\boldsymbol{\rho}-\mathbf{d}|} = -\frac{2}{\sqrt{\rho^2+d^2}}, \tag{4}$$

where the terms in brackets are due to the kinetic energy operator, the second term is the effective parabolic confining term, the third term is the z-component of the angular momentum and the last term is the attractive Coulomb-type energy. The part $\hat{H}_\perp$is the harmonic oscillator Hamiltonian which has an analytical well-known solution, as shown later in Eqs. 5-7 [32, 35]. The effective confinement frequency ω in $\hat{H}_\perp$-Hamiltonian is a combination of the magnetic field cyclotron frequency ω_c and parabolic confining frequency ω_o, given as: $\omega^2 = \omega_0^2 + \frac{\omega_c^2}{4}$. The potential $V(\rho)$ represents the Coulomb interaction between the electron in the GaAs layer and the donor impurity ion, located at distance d along the z-direction in AlGaAs barrier.

Initially, the donor impurity Hamiltonian given by Eq. (1) will be solved using the exact diagonalization technique, to obtain the eigenenergies as an essential step to study the electronic and magnetic properties of the heterostructure.

If there is no impurity, the Hamiltonian ($\hat{H}_\perp$), in Eq. (1) reduces to harmonic oscillator-type with a well-known eigenstate |n, m> and eigenenergies ($E_{n,m}$). The harmonic oscillator bases (|n, m> $= \psi_{n,m}(\rho,\varphi)$) will be used to diagonalize the full Hamiltonian and to obtain the ground state energy of the impurity system.

The bases wave functions are, [32, 35]:

$$|n,m> = \psi_{n,m}(\rho,\varphi) = \frac{1}{\sqrt{2\pi}}R_{n,m}(\rho)e^{im\varphi} \tag{5}$$

where,

$$R_{n,m}(\rho) = e^{-\frac{1}{2}\rho^2\alpha^2}\rho^{|m|}\alpha^{|m|}\sqrt{\frac{2\alpha^2 n!}{(n+|m|)!}}L_n^{|m|}(\rho^2\alpha^2) \tag{6}$$

and the corresponding eigenenergies:

$$E_{n,m} = (2n+|m|+1)\hbar\omega, \tag{7}$$

where $\mathrm{L}_\mathrm{n}^{|\mathrm{m}|}(\rho^2\alpha^2)$ is the standard associated Laguerre polynomials used in Ref. [35] and α is an inverse length dimension constant which is given by:

$$\alpha = \sqrt{\frac{m^*\omega}{\hbar}} \tag{8}$$

These harmonic oscillator bases $|\mathrm{n},\mathrm{m}>$ will be used to calculate the energy matrix elements of the full donor impurity Hamiltonian in Eq. (1), $\langle R_{n,m}(\rho)|\hat{H}|R_{\acute{n},m}(\rho)\rangle$.

The magnetic properties, such as magnetization (*M*) the magnetic susceptibility (χ) of the donor impurity in a heterostructure, are calculated from the computed energies of the donor impurity system.

The magnetization of the donor impurity in a heterostructure is evaluated as the magnetic field derivative of the energy of the donor impurity [26, 28].

$$M = -\frac{\partial \mathrm{E}(\omega_c,\omega_o,d)}{\partial \mathrm{B}} \tag{9}$$

The magnetic susceptibility is evaluated as the magnetic field derivative of the magnetization of the donor impurity in a heterostructure as [26, 28]:

$$\chi = \frac{\partial \mathrm{M}}{\partial \mathrm{B}} \tag{10}$$

or

$$\chi = -\frac{\partial^2 \mathrm{E}(\omega_c,\omega_o,d)}{\partial \mathrm{B}^2} \tag{11}$$

We investigated the dependence of the computed magnetic properties, M and χ, of the donor impurity in a heterostructure on the system's physical parameters: magnetic field ω_c, confining frequency ω_o and impurity position d.

The effective Bohr radius and Rydberg constant will be defined in terms of pressure and temperature, to study their effects on M and χ of the donor impurity in a heterostructure.

The effective Bohr radius, $a_B^*(P,T)$, is given as, [12, 27, 32]:

$$a_B^*(P,T) = \frac{\epsilon(P,T)\hbar^2}{m^*(P,T)e^2} \tag{12}$$

The effective Rydberg constant can be written as, [12, 27, 32]:

$$R_y^*(P,T) = \frac{e^4 m^*(P,T)}{2\left(\epsilon(P,T)\right)^2\hbar^2} \tag{13}$$

The effects of the pressure and the temperature on the energy, magnetization and susceptibility of the ground state will be studied using the effective mass approximation method (EMA).

The material parameters, such as: electron effective mass, $m^*(P,T)$ and dielectric constant $\epsilon_r(P,T)$, are now used in the impurity Hamiltonian as shown below:

$$\hat{H}(\rho) = \frac{1}{2m^*(P,T)}\left[\vec{p}(\rho) + \frac{e}{c}\vec{A}(\rho)\right]^2 + \frac{1}{2}m^*(P,T)\omega_0^2\rho^2 - \frac{e^2}{\epsilon_r(P,T)\sqrt{\rho^2+d^2}} \qquad (14)$$

For quantum heterostructure made of GaAs, the dielectric constant $\epsilon_r(P,T)$ and the electron effective mass $m^*(P,T)$ are presented by [12, 27, 32]:

$$\in_r(P,T) = \begin{cases} 12.74\exp(-1.73\times10^{-3}P) \\ \exp[9.4\times10^{-5}(T-75.6)] \\ \quad \text{for T} < 200\text{ K} \\ 13.18\exp(-1.73\times10^{-3}P) \\ \exp[20.4\times10^{-5}(T-300)] \\ \quad \text{forT} \geq 200\text{ K} \end{cases} \qquad (15)$$

$$m^*(P,T) = \left[1 + 7.51\times\left(\frac{2}{E_g^{\Gamma}(P,T)} + \frac{1}{E_g^{\Gamma}(P,T)+0.341}\right)\right]^{-1} m_0 \qquad (16)$$

$$E_g^{\Gamma}(P,T) = \left[1.519 - 5.405\times10^{-4}\frac{T^2}{T+204}\right] + bP + cP^2 \qquad (17)$$

where $m_0$is the free electron mass, $E_g^{\Gamma}(P,T)$ is the pressure- and temperature-dependent energy band gap for GaAs quantum heterostructure at Γ point, b = $1.26\times10^{-1}\text{eV GPa}^{-1}$ and c = -3.77$\times 10^{-3}\text{eV GPa}^{-2}$.

For heterostructure systems made from GaAs, the numerical values of the material parameters are: effective Rydberg $R^* = 5.926\, meV$, dielectric constant $\epsilon = 12.4$ and the effective mass of an electron $m^* = 0.067\, m_e$ at ambient zero temperature and pressure.

3. Results and Discussion

Initially, we will show the donor impurity energy dependence. The ground state eigenenergy (where m = 0) for the donor impurity of GaAs/AlGaAs heterostructure is computed as a function of the magnetic field strength ω_c, impurity located at the origin (d=0) and for two specific values of the confinement frequency strength, $\omega_0 = 5.412\, R^*$ and $\omega_0 = 3.044\, R^*$.

First, we will verify the convergency of the computed eigenstates. Fig. 1 shows the computed ground state energies (E) of the donor impurity against the number of basis (n) from 1 up to 38 for $\omega_0 = 3.044\, R^*$, impurity distance 0.5 a^* and magnetic field strength $\omega_c = 2\, R^*$. The figure shows a very good numerical stability in the computed energies.

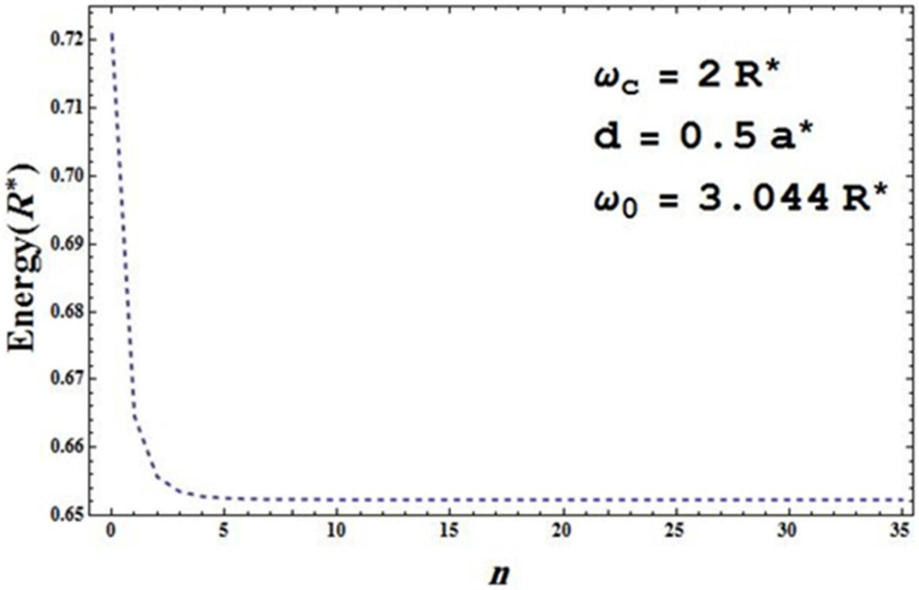

FIG. 1. The ground state energy of the quantum heterostructure for fixed values of magnetic field strength $(\omega_c) = 2\, R^*$and parabolic confinment strength $\omega_0 = 3.044R^*$ against the number of basis (n) for donor impurity at (d = 0.5 a^*).

The ground-state eigenenergies (E) for two specific values of confinement frequency ($\omega_0 = 3.044\ \mathrm{R}^*$, dashed line and $\omega_0 = 5.412\ R^*$, *solid line*) are computed as a function of the magnetic strength ω_c and for impurity distance d = $0.5\,a^*$, as shown in Fig. 2. We can clearly notice that as the magnetic field strength ω_c increases, the energy also increases. Moreover, the curves of energies of higher parabolic confinement effect, $\omega_0 = 5.412\ R^*$, have larger values than those for $\omega_0 = 3.044\ \mathrm{R}^*$. This is because the parabolic effective frequency ($\omega^2 = \omega_0^2 + \frac{\omega_c^2}{4}$) increases also as ω_0 increases, which leads to the enhancement of the electron energy due to the parabolic confinement term of the donor impurity Hamiltonian, $\frac{1}{4}\omega^2\rho^2$.

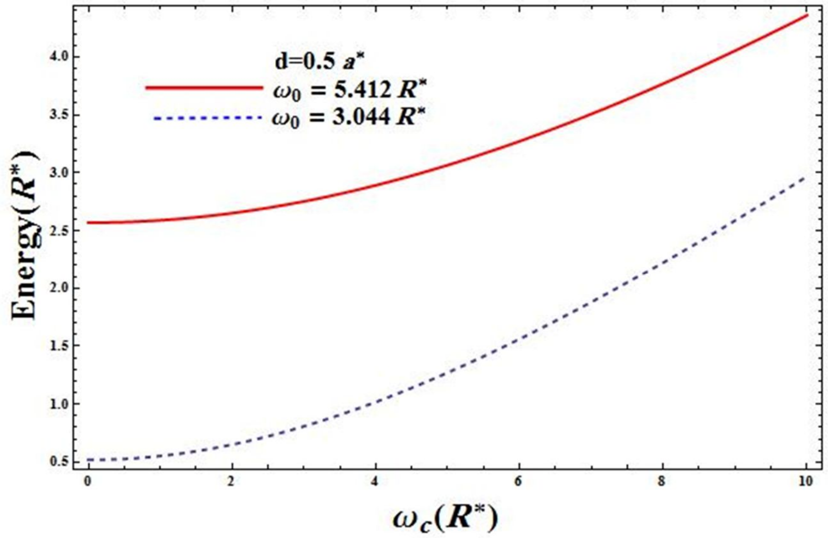

FIG. 2. The variation of the ground state energy against the magnetic field strength ω_c for $\omega_0 = 3.044\ \mathrm{R}^*$(dashed line), $\omega_0 = 5.412\ R^*$ (solid line) and d = $0.5\ a^*$.

We have also studied the temperature and pressure effects on the magnetization and the magnetic susceptibility. The plots of the magnetic quantities are shown as a function of the magnetic field strength. The results for M of GaAs/AlGaAs quantum heterostructure doped with donor impurity at d = $0.5a^*$ are presented in Fig. 3. The curve of M against ω_c is calculated at $\omega_0 = 3.044\ R^*$, $\mathrm{d} = 0.5a^*$, at various temperatures ($T = 5K, 100K, 200K$) and a fixed value of P = 10 kbar. It is clear that the ground state magnetization curves decline as ω_c increases. The material parameters m^* *and* ϵ_r are pressure- and temperature-dependent: effective mass $m^*(P,T)$ and dielectric constant $\epsilon_r(P,T)$. For a fixed value of P, m^* decreases and ϵ_r increases as the temperature increases, which leads to the increase in the values of $|M|$.

Fig. 4 displays the dependence of the magnetic susceptibility (χ) on the temperature for a fixed value of P = 10 kbar, $d = 0.5\ a^*$ and $\omega_0 = 3.044\ R^*$. The plots clearly show that the absolute value of the magnetic susceptibility $|\chi|$, at a fixed value of temperature, enhances as the cyclotron frequency, ω_c, increases. However, the curves show a small decrease in $|\chi|$-values as the temperature increases, for particular values of magnetic strength. Moreover, we can notice that the sign of χ is negative ($\chi < 0$), which indicates that the material is of a diamagnetic type.

The effect of the pressure on the donor magnetization as a function of the magnetic field strength is studied in Fig. 5. The values of M are computed at fixed temperature T = 20 K, $\omega_0 = 3.044\ \mathrm{R}^*$, impurity position d = $0.5a^*$ and various pressures: P = 0, 10 and 20 kbar. The magnetization plots, at various pressure values, decline as ω_c increases. Furthermore, for a fixed value of T, m^* increases and ϵ_r decreases as the pressure increases, which leads to the decrease in the values of $|M|$.

Fig. 6 displays the variation of the magnetic susceptibility as a function of the magnetic field strength at T = 20K, $\omega_0 = 3.044R^*$ and different pressure values: (0, 10 and 20 kbar).

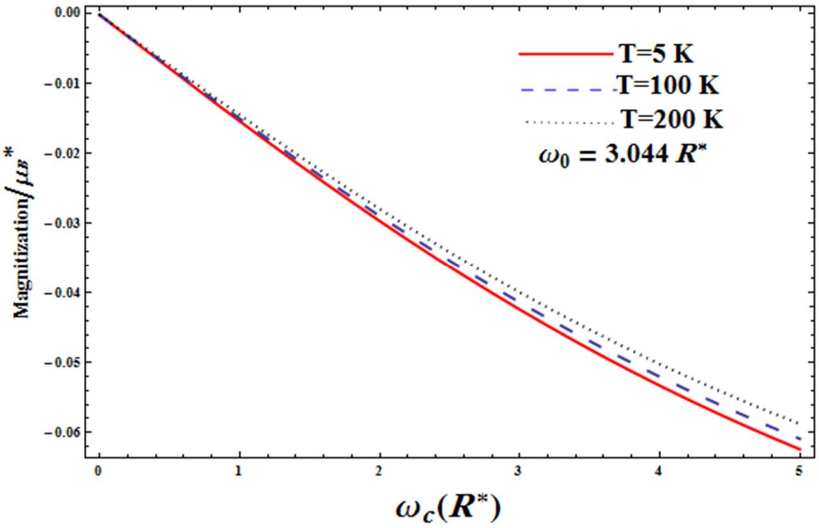

FIG. 3. The magnetization for d = 0.5a^* and $\omega_0 = 3.044\,R^*$ at constant pressure (P = 10 kbar) as a function of ω_c for three temperatures (5K, 100K and 200K).

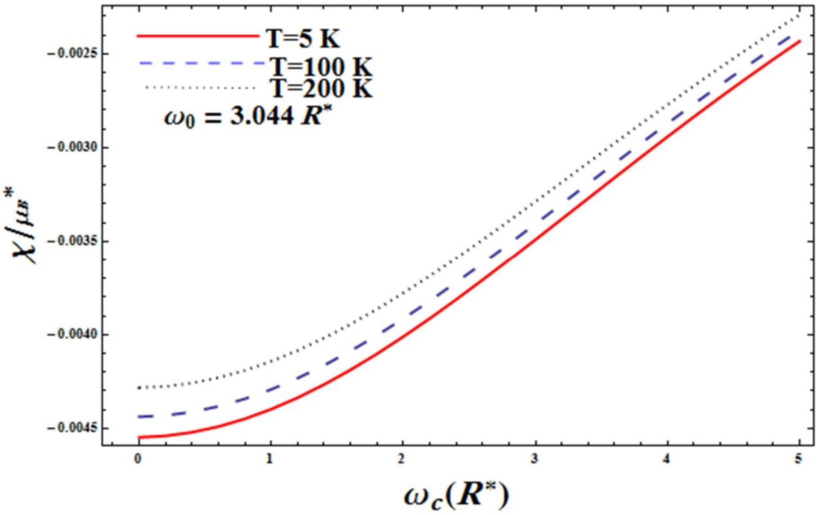

FIG. 4. The magnetic susceptibility for d = 0.5a^* at constant pressure (P = 10 kbar) as a function of ω_c for three temperatures (5K, 100K and 200K); for $\omega_0 = 3.044\,R^*$.

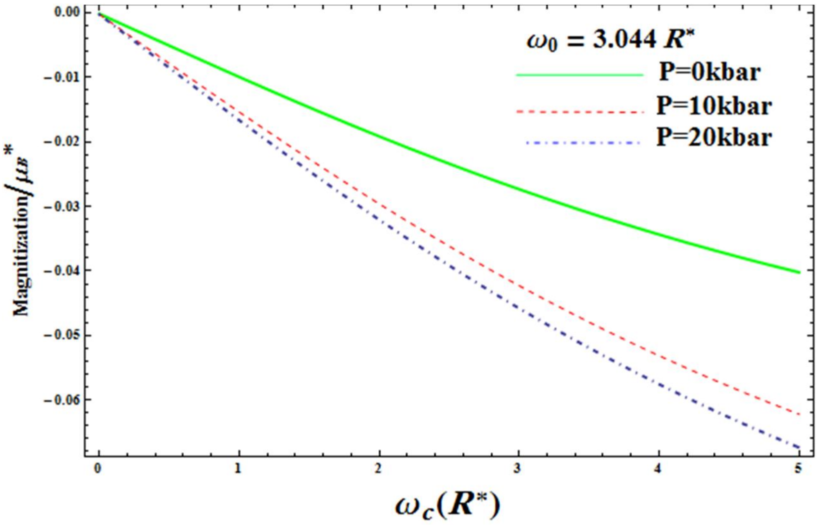

FIG. 5. The magnetization for d = 0.5a^* against ω_c at a fixed temperature (20K) for three pressure values (0, 10 and 20 kbar); for $\omega_0 = 3.044\,R^*$.

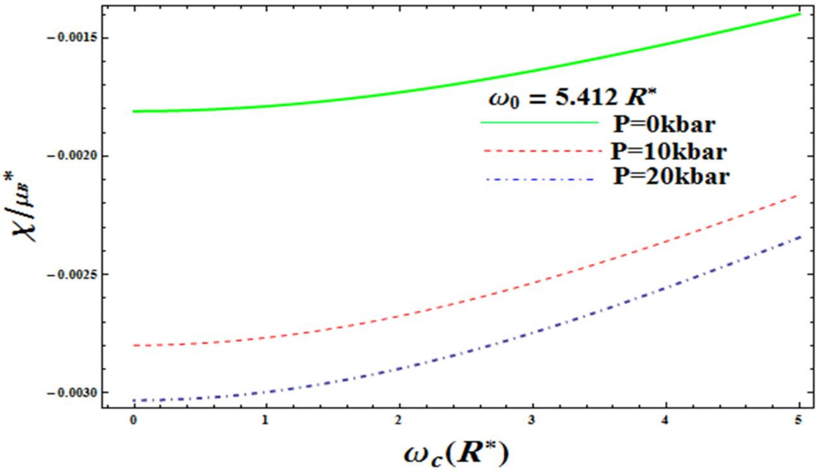

FIG. 6. The magnetic susceptibility for d = 0.5$a^*$and $\omega_0 = 3.044\ R^*b$ against ω_c at a fixed temperature (20 K) for three pressure values (0, 10 and 20 kbar).

Furthermore, we have investigated, in Figs. 7a and 7b, the effects of varying the impurity position, d, on the magnetic susceptibility, χ, against the cyclotron frequency,ω_c, for d = 0.1 a^* and d = 0.5 a^*, calculated at various confinements: $\omega_0 = 3.044\ R^*$ and $\omega_0 = 5.412\ R^*$, respectively. The plots show that the absolute value of susceptibility, $|\chi|$ enhances as we increase the donor impurity position, d, which is located along the z-axis, perpendicular to the plane of the heterostructure. This result is attributed to the reduction in the attractive Coulomb energy, $-\frac{2}{\sqrt{\rho^2+d^2}}$, between the electron confined in the heterostructure plane and the impurity located at distance, d, along the z-direction.

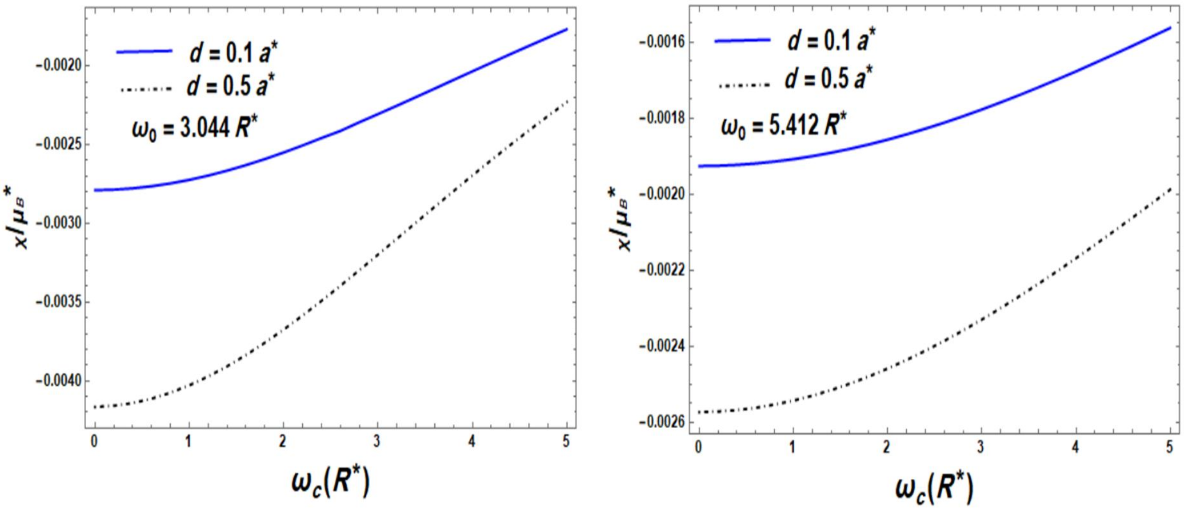

a **b**

FIG. 7. The dependence of the magnetic susceptibility on the position impurity (d) for a) $\omega_0 = 3.044\ R^*$ and b) $\omega_0 = 5.412\ R^*$.

Conclusion

In conclusion, the effective-mass (EM) Hamiltonian of donor impurity in GaAs/AlGaAs heterostructure had been solved using the exact diagonalization method. The effect of temperature and pressure on magnetization (M) and magnetic susceptibility (χ) had been investigated. The curves of the magnetic properties had been plotted as functions of magnetic field strength, parabolic confinement, impurity position, temperature and pressure. The results show that, at a fixed value of P, the values of $|M|$ and $|\chi|$ increase as the temperature increases. In contrast, at a fixed value of T, the values of $|M|$ and $|\chi|$ decrease as the pressure increases.

References

[1] Bastard, G., Physical Review B, 24 (8) (1981) 4714.

[2] Porras-Montenegro, N. and Pe, S.T., Physical Review B, 46 (15) (1992) 9780.

[3] Porras-Montenegro, N., Pérez-Merchancano, S.T. and Latge, A., Journal of Applied Physics, 74 (12) (1993) 7624.

[4] Ciftja, O., Physica Scripta, 88 (5) (2013) 058302.

[5] Bimberg, D. and Pohl, U.W., Materials Today, 14 (9) (2011) 388.

[6] Liang, S.J. and Xie, W.F., The European Physical Journal B, 81 (1) (2011) 79.

[7] Bahramiyan, H. and Khordad, R., Optical and Quantum Electronics, 46 (5) (2014) 719.

[8] Holtz, O. and Zhao, Q.X., "Impurities Confined in Quantum Structures", Vol. 77, (Springer Science & Business Media, 2004).

[9] Dingle, R., Störmer, H.L., Gossard, A.C. and Wiegmann, W., Applied Physics Letters, 33 (7) (1978) 665.

[10] Zhu, J.-L., Physical Review B, 39 (12) (1989) 8780.

[11] Yuan, J.-H. and Liu, C., Physica E: Low-dimensional Systems and Nanostructures, 41 (1) (2008) 41.

[12] Rezaei, G. and Kish, S.S., Physica E: Low-dimensional Systems and Nanostructures, 45 (2012) 56.

[13] Zhu, J.-L., Cheng, Y. and Xiong, J.-J., Physics Letters A, 145 (6-7) (1990) 358.

[14] Mmadi, A., Rahmani, K., Zorkani, I. and Jorio, A., Superlattices and Microstructures, 57 (2013) 27.

[15] Miller, D.A.B., Chemla, D.S. and Schmitt-Rink, S., Physical Review B, 33 (10) (1986) 6976.

[16] Chen, H., Li, X. and Zhou, S., Physical Review B, 44 (12) (1991) 6220.

[17] Chuu, D.S., Hsiao, C.M. and Mei, W.N., Physical Review B, 46 (7) (1992) 3898.

[18] Zhu, K.-D. and Gu, S.-W., Physics Letters A, 172 (4) (1993) 296.

[19] Ilaiwi, K.F. and El-Said, M., Physica Status Solidi (B), 187 (1) (1995) 93.

[20] De Groote, J.-J.S., Hornos, J.E.M. and Chaplik, A.V., Physical Review B, 46 (19) (1992) 12773.

[21] Khordad, R. and Fathizadeh, N., Physica B: Condensed Matter, 407 (8) (2012) 1301.

[22] Peter, A.J., Solid State Communications, 147 (7-8) (2008) 296.

[23] Perez-Merchancano, S.T., Paredes-Gutierrez, H. and Silva-Valencia, J., Journal of Physics: Condensed Matter, 19 (2) (2006) 026225.

[24] Bzour, F., Shaer, A. and Elsaid, M.K., Journal of Taibah University for Science, 11 (6) (2017) 1122.

[25] Schwarz, M.P., Grundler, D., Wilde, M., Heyn, C. and Heitmann, D., Journal of Applied Physics, 91 (10) (2002) 6875.

[26] Hjaz, E., Elsaid, M.K. and Elhasan, M., Journal of Computational and Theoretical Nanoscience, 14 (4) (2017) 1700.

[27] Bzour, F., Elsaid, M.K. and Ilaiwi, K.F., Journal of King Saud University-Science, 30 (1) (2018) 83.

[28] Elsaid, M.K. and Hijaz, E., Acta Physica Polonica A, 131 (6) (2017) 1491.

[29] Nammas, F.S., Physica A: Statistical Mechanics and Its Applications, 508 (2018) 187.

[30] Shaer, A., Elsaid, M. and Elhasan, M., Turkish Journal of Physics, 40 (3) (2016) 209.

[31] Shaer, A., Elsaid, M.K. and Elhasan, M., Chinese Journal of Physics, 54 (3) (2016) 391.

[32] Abuzaid, S., Shaer, A. and Elsaid, M., International Journal of Nano Dimension, 10 (4) (2019) 375.

[33] Shaer, A., Elsaid, M.K. and Elhasan, M., J. Phys. Sci. Appl., 6 (2) (2016) 39.

[34] Elsaid, M.K., Abu Alia, A. and Shaer, A., Chinese Journal of Physics, 66 (2020) 335.

[35] Bruno-Alfonso, A.,Candido, L. and Hai, G.O., J. Phys. Condens. Matter, 22 (2010) 125801.

Volume 14, Number 3, 2021. pp. 239-247

Jordan Journal of Physics

ARTICLE

Second Virial Coefficient of Low-density Lithium-7 (^{7}Li) Gas in the Temperature Range 1 K–40000 K and Beyond

Mustafa M. Hawamdeh

Department of Physics, Faculty of Science, Al-Balqa Applied University, Al- Salt, Jordan.

Doi: **https://doi.org/10.47011/14.3.6**

Received on: 09/06/2020; Accepted on: 21/8/2020

Abstract: The second virial coefficient B for low-dense ^{7}Lithium (^{7}Li) gas is calculated over a wide temperature range 1 K–40000 K. In the 'high'-T limit (600 K–45000 K), the classical coefficient, B_{cl}, and the contribution of the first quantum-mechanical correction, B_{qc}, are computed from standard expressions, using a suitable binary potential. The classical coefficient, B_{cl}, together with the Boyle temperature, T_B, are determined and their values are in good agreement with previous results. In addition, the interface between the classical and quantum regimes is systematically investigated. Furthermore, the calculation of the quantum-mechanical second virial coefficient, B_q, is evaluated using the Beth-Uhlenbeck formula in the temperature range 1 K–500 K. A positive value of B_q indicates that the net interaction energy is repulsive, implying that the short-range repulsive forces dominate the long-range attractive forces. However, quite the opposite occurs for negative values of B_q, which are indicative of net attractive interaction. The general behavior of B_q is similar to the potential energy itself, such that the long-range attractive and the short-range repulsive potentials can be deduced from the measurements of B_q.

Keywords: Second virial coefficient, Low-density Lithium-7 Gas, Short-range repulsive forces, Long-range attractive forces.

PACS: 51.30.+i.

1. Introduction

This paper is a theoretical study of the second virial coefficient B over a wide temperature range (1 K–40000 K). In the high temperature limit (600 K–40000 K and beyond), B is most likely to behave classically. Therefore, we focus on the classical second virial coefficient (B_{cl}) and the contribution of the first quantum correction (B_{qc}). In the low temperature limit (1 K–100 K), we focus on the quantum second virial coefficient (B_q). To investigate the boundary line between the classical and quantum regimes, we focus on the intermediate temperature range from (100 K–500 K).

The temperature-dependent second virial coefficient B(T) is a basic thermodynamic parameter and is important for representing the equation of state of the system P-V-T (pressure–volume–temperature), describing the behavior of real, low-density gases. In general, it is characteristic of the interaction potential between the particles. It represents the non-ideality of gas behavior arising due to the two-body interactions between atoms. Also, the sign of the second virial coefficient reflects how much the contribution of the attractive and repulsive parts of the potentials [1-4]. The intermolecular potential can be developed from experimental measurements of B [5], as there are many methods like static light scattering (SLS) [6]. B acts as an indicator of the classical-quantum borderline in a nonideal gas [4]. Moreover, it provides the connection between the microscopic and macroscopic properties, such as how the binary interactions affect the thermodynamic properties of a physical system. Most interestingly, B_q can provide information about

Corresponding Author: Mustafa M. Hawamdeh **Email**: mus.haw@bau.edu.jo

the possibility of the formation of small clusters [7].

Quite a number of studies calculated the second virial coefficients of all the alkali vapors over a wide range of temperatures using different potentials. For example, Sannigrahi *et al.* [8] used the Morse and Rydberg potentials for the ground singlet state and their anti-Morse potential for the triplet state. Nieto de Castro *et al.* [9] used the two-body interaction potential energy functions for the ground singlet state and excited triplet states of the alkali atoms proposed by Varandas *et al.* [10]. Mies and Julienne [11] used an electronic-rotational potential and Moncef [12] used the Rydberg-Klein-Rees interatomic singlet and triplet potentials.

The main input in calculating B is the interaction potential. In this work, we have used the singlet $X\,^1\Sigma$+g and triplet $a\,^3\Sigma$+u interatomic potentials as constructed for different three potentials; namely, Morse, Rydberg and the modified Morse potentials. A brief description of them is presented in Section 2 which is specified for the theoretical framework. In Section 3, the results are presented and discussed thoroughly with suitable comparisons. In Section 4, the paper ends with a short conclusion.

2. Theoretical Formalism

2.1 Classical Virial Coefficient

The simple classical expressions of the second virial coefficient and its quantum correction as functions of temperature *T*, are given by [13, 14]:

$$B_{cl}(T) = 2\pi \int_0^{\infty} \left[1 - e^{-\beta V(r)}\right] r^2 dr; \qquad (1)$$

$$B_{qc}(T) = \frac{\pi \hbar^2 \beta^3}{6m} \int_0^{\infty} \left[e^{-\beta V(r)}\right] (V'(r))^2 r^2 dr \qquad (2)$$

where $\hbar, \beta, m$ denote the reduced Planck's constant, the inverse temperature parameter $(k_B T)^{-1}$, k_B Boltzmann's constant, and the mass of the ^{7}Li atom, respectively. T is the temperature in Kelvin, $V(r)$ is the pair interatomic potential and $V'(r)$ is its first derivative with respect to the argument r.

The total second virial coefficient for a gas of atoms which interact via singlet and triplet potentials was given by Sinanoglu and Pitzer [15] and reads:

$$B = \frac{1}{4} B_2^{(s)} + \frac{3}{4} B_2^{(t)}, \qquad (3)$$

$B_2^{(s)}$ and $B_2^{(t)}$ being the the virial coefficients obtained from the interaction potential energy function for the different singlet and triplet-spin energy states, respectively. The first two potentials used are the Morse $U_M{}^s(r)$ and Rydberg $U_R{}^s(r)$ potentials for singlet states, which are given by:

$$U_M{}^s(r) = U_e\left[e^{-2ax} - 2e^{-ax}\right] \qquad (4a)$$

$$U_R{}^s(r) = U_e\left[e^{-bx}\right](1 + bx) \qquad (4b)$$

where $a = r_e(\kappa_e/2U_e)^{1/2}$, $x = \frac{r}{r_e} - 1$, $b = \sqrt{2a}$ and κ_e is the vibrational force constant of the diatomic alkali metal molecules. Here, the U_e, r_e, k_e are constants and are listed in Table 1. The anti-Morse potential $U^t(r)$ was proposed by [8] for the triplet state and is given by:

$$U^t(r) = 0.4427\, U_e\left[e^{-2ax} + 0.092\, e^{-ax}\right]. \qquad (5)$$

The anti-Morse function is a repulsive potential and goes to zero at infinite distance. Eq. (5) expresses the triplet-state potential in terms of ground-state potential parameters.

TABLE 1. Parameters of the Morse and anti-Morse potentials.

Parameter	Value
U_e	1.06 eV
r_e	2.65
κ_e	0.254

The third potential used is the modified Morse potential (HH-potential) [16]. It depends on the two-body Li atom interactions and is taken in the present work as the HH-hybrid potential for the singlet and triplet states [16-18]. The HH-potential is given by [16]:

$$V^*(r^*) = \varepsilon' \left\{ \begin{matrix} \exp\left[-2a\left(\frac{r^*}{d} - 1\right);\right] \\ -2\exp\left[-a\left(\frac{r^*}{d} - 1\right)\right] \\ +\beta\left(\frac{r^*}{d} - 1\right)^3 \times \\ \left[1 + \gamma\left(\frac{r^*}{d} - 1\right)\right]\exp\left[-2a\left(\frac{r^*}{d} - 1\right)\right] \end{matrix} \right\}; \qquad (6)$$

where $V^* = \frac{v}{\varepsilon'}$; $r^* = \frac{r}{\sigma}$; $d = \frac{r_e}{\sigma}$; $\sigma = 3.24$Å; $a = \frac{\omega_e}{2\sqrt{\beta_e \varepsilon'}}$; $\beta = ca^3$; $\gamma = ba$; $c = 1 + a_1\sqrt{\frac{\varepsilon'}{a_\circ}}$; $b = 2\text{-}\frac{\frac{7}{12} - \varepsilon'\frac{a_2}{a_\circ}}{c}$; $a_0 = \frac{{\omega_e}^2}{4\beta_e}$; $a_1 = -1 - \frac{\alpha_e \omega_e}{6\beta_e^2}$; $a_2 = \frac{5}{4}a_1^2 - \frac{2\omega_e \chi_e}{3\beta_e}$, ε' being the well depth in cm^{-1}.

This potential depends on the spectroscopic constants, the well depth ε', the fundamental vibration frequency ω_e, the anharmonicity constant $\omega_e \chi_e$, the rotational constant β_e, the vibration-rotation coupling constant α_e and the equilibrium internuclear separation r_e of the atoms in the dimer. The latter are listed for the singlet and triplet states of Li in Table 2 [16-18]. The Li-Li potentials for the singlet $x^1\Sigma_g^+$ and triplet $x^3\Sigma_u^+$ states are plotted as shown in Fig.1.

TABLE 2. HH parameters for the states $x^1\Sigma_g^+$ and $a^3\Sigma_u^+$ of Li, as obtained from the spectroscopic constants.

Parameter	$x^1\Sigma_g^+$ [16]	$a^3\Sigma_u^+$ [17, 18]
ε'	8614 (cm^{-1})	338.71(cm^{-1})
ω_e	351.43 (cm^{-1})	64.88 (cm^{-1})
$\omega_e\chi_e$	2.61 (cm^{-1})	3.41 (cm^{-1})
β_e	0.67264 (cm^{-1})	0.279 (cm^{-1})
α_e	0.00704 (cm^{-1})	0.0187 (cm^{-1})
r_e	2.6729 Å	4.154 Å

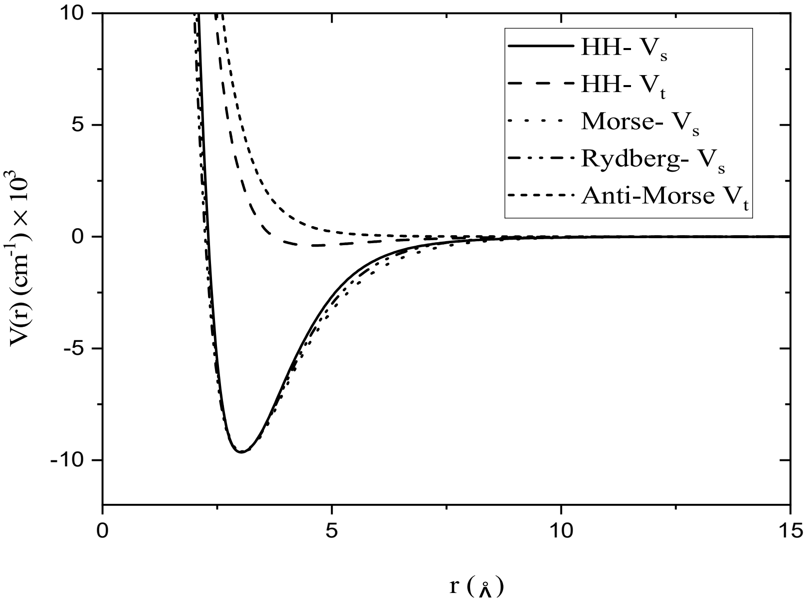

FIG. 1. Li-Li potentials for the singlet $x^1\Sigma_g^+$ and triplet $x^3\Sigma_u^+$ states, the HH-potential and Morse and Rydberg potentials.

2.2 Quantum Second Virial Coefficient, B_q

The Uhlenbeck and Beth formula for the quantum second virial coefficient at low temperatures is given by [19, 20]:

$$B_q(T) = -\frac{\lambda^3}{2^{5/2}} - 2^{3/2}\lambda^3 \sum_{E_B}\left(e^{-\beta E_B} - 1\right) - \frac{2^{3/2}\lambda^5}{\pi^2}\int_0^\infty dk\, k \sum_l{}'(2l+1)\delta_l(k) e^{-\beta E(k)} \quad (7)$$

Eq. (7) contains three terms: B_{ideal}, B_{bound} and B_{phase}. B_{ideal} is the quantum ideal-gas term. This is dominant in the low-temperature region; it goes to zero at large T. B_{bound} is the term consisting of the discrete energy spectrum made possible by the two-body interaction, where E_B are the bound-state energies. The latter is ignored for the Lithium system, since it is unbounded in the T-range of this study. Finally, B_{phase} denotes the contribution of the scattering-state continuum, where $\delta_\ell(k)$ stands for the scattering phase of the l^{th} partial wave of wavenumber k that arises because of the pair interaction V(r). The factor $(2l+1)$ for the degenerate state comes from the magnetic quantum number m and the primed summation $\sum_l{}'$ goes over even ℓ values in the case of bosons. The bound state term (discrete-state contribution) can be neglected, because it is quite small. Therefore, the two contributions to the overall value of B_q are the quantum ideal-gas term and the scattering term (continuum-state contribution).

The phase-shifts $\delta_\ell(k)$ can be obtained numerically from the solution of the Lippmann-Schwinger (LS) integral equation which describes momentum space scattering in terms of the T-matrix, using a matrix-inversion technique. The LS formalism is well-described elsewhere [21-23]. The basic input in computing is the interatomic potential.

Throughout our work, we used natural units such that $\hbar, m, k_B$ are exactly equal to 1 and applied the conversion factor $\frac{\hbar^2}{\text{m}} = 6.919\ \text{K}.\text{Å}^2$. In this system, all physical quantities can be expressed in terms of [length, L]. One can easily go back to SI units through the conversion factor quoted.

3. Results and Discussion

3.1 Classical Second Virial Coefficient with First Quantum Correction, B_{qc}

Our results for the classical second virial coefficient B_{cl} and the first quantum correction B_{qc} are shown in Tables 3-7 and Fig. 2. Table 3 shows B_{cl}, B_{qc} and B_{total} in the T-range 600 K to 45000 K for the singlet (Morse and Rydberg potentials) and anti-Morse potential for the triplet state. B_{total} is calculated by adding B_{qc} to B_{cl}. It is found that B_{total} is negative, but it increases (i.e., its absolute value decreases) as T rises. The negative sign means that the interaction is attractive. At a certain $T \equiv T_B$ (*Boyle's temperature*), B_{total} = zero. This occurs when the attractive forces balance exactly the repulsive forces. In Table 4, the present results for the Boyle temperature T_B are compared to previous results [8] displaying good agreement. By increasing T ($T > T_B$), B_{total} becomes positive because of the repulsive forces. For the HH potential, B_{total} equals zero at T = 126852 K. It is very high compared to the previous calculated value from the Morse and Rydberg potentials.

TABLE 3. The classical second virial coefficient B_{cl} (cm^3/mole) and first quantum correction B_{qc} (cm^3/mole), at different temperatures T [K] for singlet (Morse and Rydberg potentials) and triplet state (using anti-Morse potential).

T[K]	Morse		Rydberg		Anti-Morse		B_{total} [cm^3/mole]	
	B^s_{cl} [cm^3/mole]	B^s_{qc} [cm^3/mole]	B^s_{cl} [m^3/mole]	B^s_{qc} [cm^3/mole]	B^t_{cl} [cm^3/mole]	B^t_{qc} [cm^3/mole]	Morse	Rydberg
600	-1.02×10^{10}	2.78×10^{8}	-1.02×10^{10}	2.78×10^{8}	134.7	0.0825	-2.50×10^{9}	-2.49×10^{9}
700	-6.02×10^{8}	1.18×10^{7}	-5.98×10^{8}	1.18×10^{7}	125.7	0.06768	-1.47×10^{8}	-1.47×10^{8}
800	-7.24×10^{7}	1.07×10^{6}	-7.20×10^{7}	1.07×10^{6}	118.4	0.05694	-1.78×10^{7}	-1.77×10^{7}
900	-1.41×10^{7}	1.6×10^{5}	-1.40×10^{7}	1.61×10^{5}	112.2	0.04885	-3.48×10^{6}	-3.46×10^{6}
1000	-3.84×10^{6}	3.50×10^{5}	-3.81×10^{6}	3.50×10^{5}	106.9	0.04255	-9.51×10^{5}	-9.43×10^{5}
1200	-5.58×10^{5}	3401	-5.52×10^{5}	3.40×10^{3}	98.19	0.03346	-1.39×10^{5}	-1.37×10^{5}
1400	-1.44×10^{5}	619.1	-1.42×10^{5}	618.43	91.31	0.02726	-3.58×10^{4}	-3.53×10^{4}
1600	-8.44×10^{4}	167.5	-5.23×10^{4}	167.30	85.68	0.02279	-2.10×10^{3}	-1.29×10^{4}
1800	-2.49×10^{4}	59.22	-2.43×10^{4}	59.12	80.95	0.01945	-6.14×10^{3}	-6.01×10^{3}
2000	-1.37×10^{4}	25.29	-1.34×10^{4}	25.24	76.9029	0.0168544	-3.37×10^{3}	-3.28×10^{3}
2400	-5.77×10^{3}	6.76	-5.57×10^{3}	6.744	70.29	0.013132	-1.39×10^{3}	-1.34×10^{3}
2800	-3.17×10^{3}	2.527	-3.03×10^{3}	2.516	65.06	0.01061	-743	-709
3000	-2.51×10^{3}	1.681	-2.39×10^{3}	1.673	62.82	0.009640	-579	-549
3500	-1.57×10^{3}	0.7223	-1.48×10^{3}	0.7177	58.04	0.007767	-349	-327
4000	-1.12×10^{3}	0.3706	-1.04×10^{3}	0.3675	54.14	0.006430	-237	-219
5000	-674.5	0.1359	-624.4	0.1343	48.08	0.004671	-133	-120
6000	-476.1	0.06533	-437.2	0.06427	43.54	0.003583	-86.4	-76.6
10000	-212.1	0.01149	-191.6	---	32.57	0.00167	-28.6	-23.5
15000	-123.1	0.003676	-110.2	---	25.50	0.000888	-11.7	-8.43
20000	-86.01	0.001789	-76.65	---	21.25	0.000558	-5.56	-3.22
25000	-65.76	0.001062	-58.44	---	18.35	0.000385	-2.68	-0.845
28000	-57.52	0.001022	-51.05	---	17.00	0.000324	-1.63	-0.00089
29000	-55.19	0.000932	-48.97	---	16.60	0.000301	-1.35	0.210
30000	-53.0	0.000707	-47.05	---	16.22	0.000282	-1.09	0.405
35000	-44.34	0.000506	-39.27	---	14.58	0.000215	-0.152	1.11
36000	-42.92	0.000476	-38.00	---	14.29	0.0002047	-0.0114	1.22
37000	-41.58	0.000449	-36.81	---	14.02	0.000195	0.117	1.31
40000	-38.01	0.00038	-33.63	---	13.26	0.000169	0.442	1.54
45000	-33.21	0.000297	-29.36	---	12.18	0.000137	0.831	1.79

TABLE 4. Boyle temperatures T_B [K] compared to previous results [8].

T_B [K]			
Present results		[8]	
Morse	Rydberg	Morse	Rydberg
36086	28039	31244	23799

Fig. 2 displays B_{total} in the T-range 500 K–30000 K. B_{total} continues to increase with increasing T, but it changes relatively slowly at the higher T values. It is expected that B_{total} flattens out while dropping slowly toward zero at significantly higher temperatures. It is noted that the second virial coefficient is positive or negative depending on the temperature. The explanation for this T-behavior of B_{cl} is as follows: the negative values of B are indicative of a net attractive interaction between the particles; conversely, a positive value is an indication that the net interaction energy is repulsive. If B equals zero, then no interactions are present and the virial equation reduces to the equation of state for the ideal gas. The figure shows that at low temperatures, B is largely negative, but above a certain temperature, it becomes positive and less dependent on temperature. At low T, the weak attractive part of the potential dominates the low kinetic energy of Li atoms, leading to a negative B_{cl}. As temperature increases, atoms become more energetic, increasing the contribution of short-range repulsive forces and causing B to become less negative. In contrast, at high T, the large kinetic energy of the Li atoms leads to a net repulsive interaction among them, yielding thereby a positive B. At high T, B increases slowly with temperature.

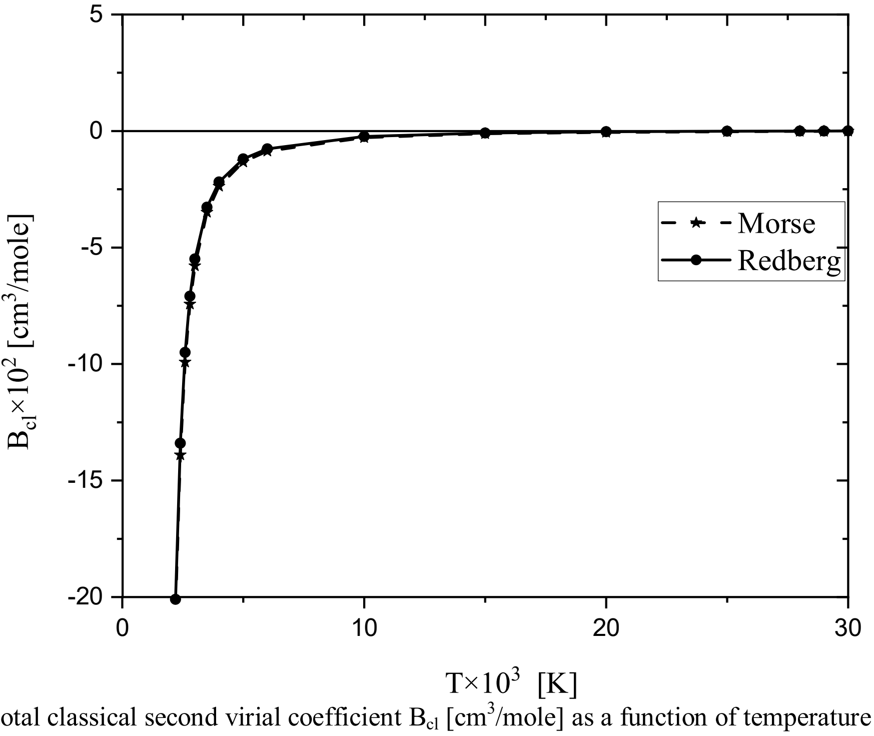

FIG. 2. The total classical second virial coefficient B_{cl} [cm^3/mole] as a function of temperature T [K] using Morse and Rydberg potentials.

In order to test the reliability of the present calculation, we have used a third potential; namely the modified Morse potential (HH-potential). In Tables 5 and 6, the present results for B_{total} are compared to previous results in [8, 9, 11, 16, 24]. It is noted that the present results are of the same order of magnitude as the previous results. The values of the first quantum correction B_{qc} from 600 K to 45000 K are positive and decrease to zero at T= 6000 K, as shown in Table 6. In Table 7, B_{cl}, B_{qc} (for singlet and triplet states) and B_{total} are calculated in the T-range (100 K–500 K). It is noted that B^s_{qc} plays a significant role in this T-range and the quantum effects cannot be ignored in this range. It is clear that it becomes greater than $|B_{cl}|$ at T ≤ 100 K, Therefore, the classical expression fails; so that B_q must be used instead.

TABLE 5. The total classical second virial coefficient B_{total} [cm^3/mole] at different temperatures T. Previous results [8] are included for comparison purposes.

T [K]	B_{total} [cm^3/mol]			
	Present results		[8]	
	Morse	Rydberg	Morse	Rydberg
2460.253	-1244	-1201.9	-1225.3	-1201.5
4100.422	-220.8	-204.2	-218.6	-276.6
6150.632	-81.6	-72.3	-80.7	-203.4
8200.843	-43.6	-37.1	-42.9	-71.4
12301.26	-18.3	-14.3	-17.6	-36.2
16401.69	-9.4	-6.5	-8.9	-13.3
24602.53	-2.8	-0.98	-2.5	-5.2

TABLE 6. Comparison between the present results for B_{cl} and B_{qc} and previous results.

T[K]	B_{total} [m^3/mol] Present result	B_{total} [m^3/mol] [9]	B_{total} [m^3/mol] [11]	B_{total} [m^3/mol] [16]*	B_{total} [m^3/mol] [24]
500	-1.624 x 10^5	---	-1.073 x 10^5	-1.167 x 10^6	---
600	-2923	---	-2060	-6551	---
700	-167.9	---	-124.2	-575.1	---
800	-19.93	-14.93	-15.28	-69.83	---
900	-3.831	-2.963	-3.023	-10.85	-9.647
1000	-1.032	-0.8191	-0.8335	-2.059	-2.370
1200	-0.1472	-0.1213	-0.1229	-0.1155	-0.2941
1400	-0.0374	-0.03164	-0.03197	-0.03996	-0.06746
1600	-0.01361	-0.01174	-0.01184	-0.01681	-0.02265
1800	-0.00629	-0.005509	-0.005538	-0.007809	-0.00977
2000	-0.00344	-0.003039	-0.003048	-0.003962	-0.00502
2200	-0.00212	----	-0.001885	-0.002130	-0.00289
2400	-0.00143	----	-0.00127	-0.001219	-0.00182
2500	-0.0012	-0.001071	-0.001069	-0.001037	-0.00146
3000	-0.00061	-0.000544	-0.000541	-0.000557	----
3500	-0.00031	----	-0.000333	-0.000329	----
4000	-0.00026	----	-0.00023	-0.000228	----
4500	-0.00019	----	-0.000172	-0.000172	----
5000	-0.00017	----	-0.000135	-0.000133	----
5500	-0.00013	----	-0.00011	-0.000109	----
6000	-0.00011	----	-0.0000915	-0.000092	----

*The result of Holand *et al.* [16] is published in their work as a ratio from Mise and Julienne [11].

TABLE 7. B_{cl}, B_{qc} (for singlet and triplet states) and B_{total} in the T-range (100–500 K).

T[K]	B^s_{cl} [m^3/mol]	B^s_{qc} [m^3/mol]	B^t_{cl} [m^3/mol]	B^t_{qc} [m^3/mol]	B_{total} [m^3/mol]
100	-3.359×10^{54}	3.538×10^{54}	-11587.1	289.7	4.475×10^{52}
200	-5.582×10^{27}	1.526×10^{27}	-1520.5	8.315	-1.014×10^{27}
300	-7.739×10^{18}	8.857×10^{17}	-709.1	1.910	-1.713×10^{18}
400	-2.948×10^{14}	1.876×10^{13}	-447.2	0.8020	-6.901×10^{13}
500	-6.770×10^{11}	2.725×10^{10}	-320.7	0.4419	-1.624×10^{11}

3.2 Quantum Second Virial Coefficient, B_q

Our results for B_q are given in Table 8 and Fig. 3 for the T-range (1–500 K) in the zero-density limit. In this regime, the system is considered to be in the vapor phase. At very low T, B_q is positive indicating that the repulsive part of the potential is dominant. As T is increased, the attractive part becomes more dominant. The negativity of B_q rises with increasing T until it approaches a minimum at T_{min}. For $T > T_{min}$, B_q becomes less negative with increasing T, going to zero in the high limit of T. This behavior is an evidence of quantum effects. The overall behavior of B_q is the same as that of the potential itself. In the Morse and Rydberg potentials, B_q changes sign at T = 80 K and T= 90 K, respectively, from positive to negative, but for the HH-potential, B_q changes sign at T=7 K from positive to negative. This means the HH potential is more attractive than the two other potentials, since the triplet part in the Morse and Rydberg potentials is completely repulsive.

The general behavior of B_q (Fig. 3) is the same as that of the Li-Li potential V(r) itself (Fig. 1). This behavior reflects that the short-range repulsive component and the long-range attractive component with the minimum in between represent equilibrium [1]. Moreover, it is concluded that the HH-potential is the most attractive potential. The behavior of B_q must be quantum-mechanical in origin. The classical calculation of B yields a large and negative value at low temperatures in the presence of an attractive well. This behavior occurs because of the uncertainty principle. At these low temperatures, the thermal de Broglie wavelength of Li is several tens of Ångstroms, which is probably enough to “wash out” the potential energy bottom, thereby resulting in an overall repulsive interaction.

TABLE 8. The quantum second virial coefficient B_q [m^3/mole] as a function of temperature T [K] using Morse, Rydberg and HH potentials.

	$B_q[m^3/mol]$		
T [K]	Morse potential	Rydberg potential	HH potential
1	992.5	531.1	1418.4
2	531.2	235.4	495.3
4	274.8	164.6	78.53
6	180.7	133.6	7.331
7	151.1	118.8	-3.392
8	127.7	105.0	-8.781
10	93.40	81.52	-12.89
30	10.38	10.91	-8.948
50	2.251	2.679	-6.532
70	0.3642	0.5211	-5.463
90	-0.2945	-0.3277	-4.790
100	-0.4742	-0.5728	-4.520
200	-1.160	-1.399	-2.756
300	-1.347	-1.515	-1.777
400	-1.345	-1.458	-1.226
500	-1.267	-1.345	-0.9168

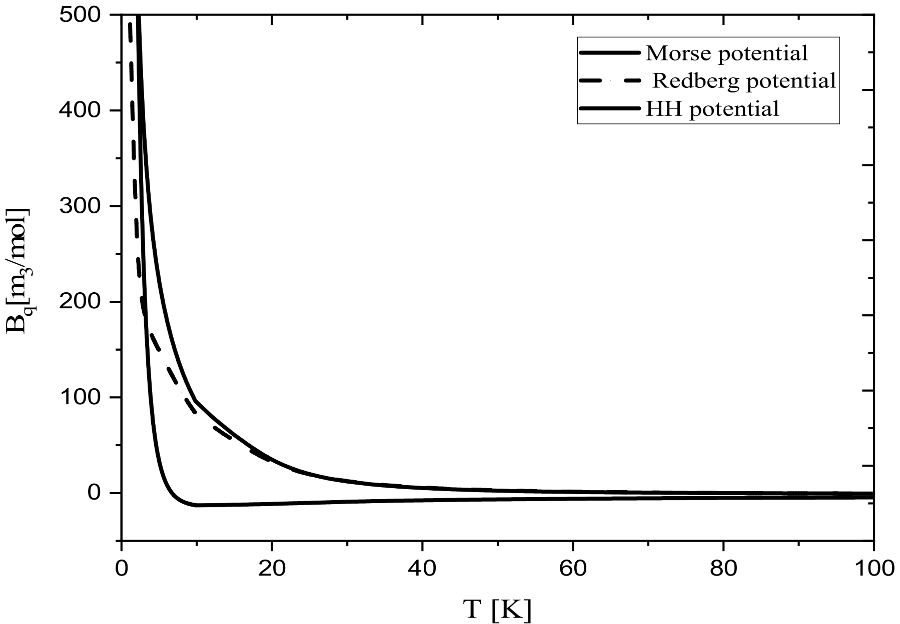

FIG. 3. The quantum second virial coefficient B_q [cm^3/mole] as a function of temperature T [K] using Morse, Rydberg and HH potentials.

4. Conclusion

This work has addressed the second virial coefficient B of low-density ^{7}Li vapor, using the Morse, Redberg and HH-potentials, in the temperature-range 1 K–45000 K and beyond. This range spans the quantum as well as classical regimes. Accordingly, the centerpiece of this work includes the calculation of the classical coefficient B_{cl} together with the first quantum correction B_{qc} and the quantum coefficient B_q. Also, the interface between the classical and quantum regimes is systematically investigated.

The main objectives of this work were to calculate the classical second virial coefficient B_{cl}, the first quantum correction B_{qc} to this coefficient in the T-range 100 K–40000 K and beyond and to determine the quantum counterpart B_q in the T-range 1 K–500 K. A positive value of B_q indicates that the net interaction energy is repulsive implying an overall repulsive effective interaction; whereas the negative values of B_q are indicative of a net attractive interaction.

It has been found that the general behavior of B_q is the same as that of the potential itself, such that the short-range repulsive and long-range attractive potentials could be deduced from the result of B_q. There seems to be an almost one-to-one correspondence between the respective repulsive, attractive and ‘minimum’ regions. Thus, information about diatomic interactions is contained in B.

In conclusion, the results show that B is a sharp indicator of the demarcation between the classical and quantum regimes. In the high-T limit, B is expected to behave classically; whereas it should behave quantum-mechanically at ‘low’ T. There are some problems that one can pursue starting with the present work. One problem is using the present formalism for exploring the gas of Lithium isotope (^{6}Li) which is a Fermi system. It would be interesting to observe the similarities and differences. Another problem is the calculation of the second virial coefficient for other atomic gases, such as Na and K.

References:

[1] Al-Obeidat, O.T., Sandouqa, A.S., Joudeh, B.R., Ghassib, H.B. and Hawamdeh, M.M., Can. J. Phys., 95 (12) (2017) 1208.

[2] Mosameh, S.M., Sandouqa, A.S., Ghassib, H.B. and Joudeh, B. R., J. Low Temp. Phys., 175 (2014) 523.

[3] Van Rijssel, J., Peters, V.F.D., Meeldijk, J.D., Kortschot, R.J., van Dijk-Moes, R.J.A., Petukhov, A.V., Erné, B.H. and Philips, A.P., J. Phys. Chem. B, 118 (2014) 11000.

[4] Ghassib, H.B., Sandouqa, A.S., Joudeh, B.R. and Mosameh, S.M., Can. J. Phys., 92 (9) (2014) 997.

[5] Laurendeau, N.M., "Statistical Thermodynamics: Fundamentals and Applications". (Cambridge University Press, 2005).

[6] Velev, O.D., Kaler, E.W. et al., Biophys. J., 75 (6) (1998) 2682.

[7] Sandouqa, A.S., Chem. Phys. Lett., 703 (2018) 29.

[8] Sannigrahi, A.B., Noor Mohammad, S. and Mookherjee, D.C., The Journal of Chemical Physics, 63 (1975) 12; Sannigrahi, A.B. and Noor Mohammad, S., Molecular Physics, 31 (3) (1976) 963.

[9] Nieto de Castro, C.A., Fareleira, J.M.N.A., Matias, P.M., Ramires, M.L.V., Pais, A.A.C.C. and Varandas, A.J.C., Ber. Bunsenges. Phys. Chem., 94 (1990) 53.

[10] Varandas, A.J.C., J. Chem. SOC. Faraday Trans., 11 (76) (1980) 129; Varandas, A.J.C. and Brandgo, J., Mol. Phys., 45 (1982) 857.

[11] Mies, F.H. and Julienne, P.S., J. Chem. Phys., 77(12) (1982) 15 Dec.

[12] Moncef, B., J. Plasma Fusion Res. Series, 7 (2006) 217.

[13] Mello, E.V.L., Rehr, J.J. and Vilches, O.E., Phys. Rev. B, 28 (7) (1983) 3759.

[14] Pack, R.T., J. Chem. Phys., 78 (1983) 7217.

[15] Sinanoglu, O. and Pitzer, K.S., J. Chem. Phys., 31 (1960) 960.

[16] Holland, P.M., Biolsi, L. and Rainwater, J.C., J. Chem. Phys., 85 (1986) 4011.

[17] Halls, M.D., Schlegel, H.B., DeWitt, M.J. and Drake, G.W.F., Chem. Phys. Lett., 339 (2001) 427.

[18] Shi, D.H., Sun, J.F., Zhu, Z.L. and Liu, Y.F., Chin. Phys. Soc., 16 (9) (2007) 2701.

[19] Uhlenbeck, G.E. and Beth, E., Physica, 3 (8) (1936) 729.

[20] Beth, E. and Uhlenbeck, G.E., Physica, 4 (10) (1937) 915.

[21] Bishop, R.F., Ghassib, H.B. and Strayer, M.R., J. Low Temp. Phys., 26 (1977) 669.

[22] Ghassib, H.B., Bishop, R.F. and Strayer, M.R., J. Low Temp. Phys., 23 (1976) 393.

[23] Bishop, R.F., Ghassib, H.B. and Strayer, M.R., Phys. Rev. A, 13 (1976) 1570.

[24] Ghatee, M.H. and Sanchooli, M., Fluid Phase Equilibria, 189 (2001) 63.

Volume 14, Number 3, 2021. pp. 249-253

Jordan Journal of Physics

ARTICLE

Optical and Electrical Analyses of Thallium Sulphide Thin Films

Q. A. Adeniji[a], **Kola Odunaike**[b], **D. A. Leshi**[b], **A. T. Talabi**[b], **A. T. Adeleke**[b], **A. O. Abe**[a], **R. E. Momoh**[c] and **F. B. Musah**[d]

[a] *Department of Physics, Federal University of Kashere, Gombe State. Nigeria.*
[b] *Department of Physics, Olabisi Onabanjo University, Ago-Iwoye, Nigeria.*
[c] *Department of Chemical Sciences, Federal University of Kashere, Gombe State. Nigeria.*
[d] *Department of Computer Science, Emmanuel Alayande College of Education, Oyo, Nigeria.*

Doi: **https://doi.org/10.47011/14.3.7**

Received on: 25/06/2020; *Accepted on: 15/9/2020*

Abstract: In this paper, suitability of thallium sulphide films were investigated as an alternative to conventional silicon and germanium that were used as window layers in solar cells. Thin films were deposited on soda lime glass (SLG) substrates in a chemical bath containing Thallium Chloride ($TlCl_2$) and Thiourea $(NH_2)_2CS$ which was conditioned at 80 °C for about 5 hours to deposit the films. Effects of annealing on the film samples at 300 °C and 350 °C were studied respectively by use of UV-VIS Avantes electrophotometer and Four-Point-Probe (FPP) machine in the light region with wavelength range from 200 nm to 1000 nm. The results obtained suggest that the thin films obtained are good materials for optoelectronics. The absorption spectra exhibited a relatively high energy band-gap. Materials of this nature are good for window layers which serve as passage to the absorber layer where needed charge carriers are produced.

Keywords: Thin film, Thallium Sulphide, Window layer, Optoelectronics, Solar cells.

Introduction

The group-III elements contain thallium which forms compounds, such as TISe (tetragonal, Eg = 0.75eV), T1S (tetragonal, Eg = 1.37eV), $T1_2S$ (tetragonal, blue-black), $T1_2S_3$ (amorphous, black), $CuTlS_2$ (chalcopyrite, Eg = l.39eV, estimated), $TlBiS_2$ (rhombohedral, Eg = 0.40eV), $TlSbS_2$ (Eg = 1.42 eV) … etc. Thus, thallium could be at (+3), (+1) or mixed oxidation states, offering also the possibility of transforming oxidation states during solid state reactions. One may note that thallium sulphide as a photoconductor and photovoltaic material has been known since the 1930s, but the use of thallium compounds has been almost eliminated in subsequent years [1]. However, an attraction which thallium may still offer as a Group-III heavy-element is its price. In bulk metal form of 99% purity, it costs in commercial quantities about US $ 100 per kilogram; typically one twentieth as that of indium. The strategy to utilize thallium to replace some amount of indium and gallium in solar cell technology might relieve the pressure on the availability of these two elements indispensable in optoelectronic device technologies. Thin films have a number of applications in various fields, ranging from coatings, interference filters, polarizers, narrow band filters, solar cells, photoconductors, IR detectors, waveguide coatings, magnetic and superconducting films and microelectronic devices [2, 3]. Ternary compounds of thallium, which include $TlSbS_2$, have reported optical band gaps (Eg) of 1.7eV [4] and 1.85eV. Generally, optical band gap in the range between 1.00eV and 2.00eV suggests possible application as absorber materials in

Corresponding Author: Q. A. Adeniji **Email**: qadeniji@yahoo.com

solar cells. Estrella *et al.* [4] deposited thallium antimony sulphide and thallium bismuth sulphide thin films produced by heating chemically deposited multi-layers. They reported the formation of these materials in thin film form by heating in nitrogen of chemically deposited $Sb_2S_3 + Tl_2S$ and $Bi_2S_3 + Tl_2S$ thin films [5]. The study was motivated by their success in producing Cu_3BiS_3, $CuSbS_2$ and $InSbS_3$ thin films by heating chemically deposited Bi_2S_3–CuS, Sb_2S_3–CuS and Sb_2S_3–In (indium by thermal evaporation) thin film coatings at temperatures of 250°C - 400°C in a nitrogen atmosphere. They felt that the very fine crystalline grains (of <5nm in diameter) inherent in chemically deposited semiconductor thin films promote interfacial diffusion of the atoms and lead to the formation of compounds at a temperature lower than what is required for their formation by sintering stoichiometric elemental mixtures. Given the fact that the films are of low band gaps and show poor transmission of visible light, they could find potential applications as solar cell absorbers [5]. These processes require the use of sophisticated machines and lots of time consumed. Bearing these potentials in mind, there are increasing demands for renewable energy as the alternative to present epileptic power supply for economic growth. Solar cells have been made majorly from Germanium and Indium. The idea of seeking alternative base materials to give room for the vast demand for optoelectronic devices has been considered. This work is also propelled to focus on an alternative technique to produce a good-quality solar absorber that is eco-friendly. That informs the need to investigate thallium sulphide for suitability as an optoelectronic material for solar applications.

Materials and Methods

The CBD bath for Thallium Sulphide film deposition was obtained by using Trisodium citrate (TSC) ($Na_3C_6H_5O_7$) as a complexing agent for thallium chloride ($TlCl_2$) which served as precursor for Tl^{2+} and Thiourea $(NH_2)_2CS$ which served as precursor for S^{2-}. 20 ml of 0.5M Thiourea, 10 ml of 1.0 M thallium chloride ($TlCl_2$) solution and 1ml of 0.5M Trisodium citrate were added into a 100 ml beaker. Then, 40 ml of distilled water was added to the solution and then gently stirred at room temperature to obtain a homogenous solution. 2ml of 0.3M Ammonia (NH3) was added in drops till an alkaline solution with pH of 8.0 was attained, as measured with Mettler Toledo AG 8603 pH meter. The mixture was immersed into a heated water bath with continuous stirring. Well prepared glass slides (3 pieces) were introduced into the mixture at 80 °C and film deposition allowed for 5 hours. After the deposition, the substrates were removed, rinsed with distilled water and allowed to dry in air. Two samples were labelled A and B for annealing at 300°C and 350°C, respectively, to study the effect of annealing on the deposited films, while the third sample served as the control referred to as *deposited* subsequently.

Results and Discussion

Optical Characteristics of Thallium Sulphide Films

As obtained from Avantes UV-VIS spectrophotometer in the range 200-1000 nm, reflectance graphs of TlS thin films are shown in Fig. 1 for the films deposited, annealed at 300 °C and at 350 °C, respectively. They were found to vary from 7 % to 15 % at initial state. Average reflectance was found to be below 30% for all films. The film for TlS annealed at 350°C had the lowest reflectance of about 28 % compared to the deposited film which has 30 %. The reflectance spectra show that the presence of heat in TlS thin films reduces reflectance of the films in the visible range, showing that annealing at higher temperature reduces the reflectance characteristics. This is in consonance with Wanjala *et al.* [6], who reported ZnS:Sn thin films for use in solar cells.

The transmittances of the films vary between 80 % and 90 % with a reduction in transmittance as the annealing temperature increases. Fig. 2 shows the transmittance spectra which indicate average transmittances of 80 % at λ=800 nm. This reveals that some states have been created in the Fermi-level between the conduction band and the valence band. This can also be attributed to the increase in fundamental absorption as photon striking increases with increase in carrier concentration [7]. This fairly high value suggests the suitability of the films for window layers in solar cells.

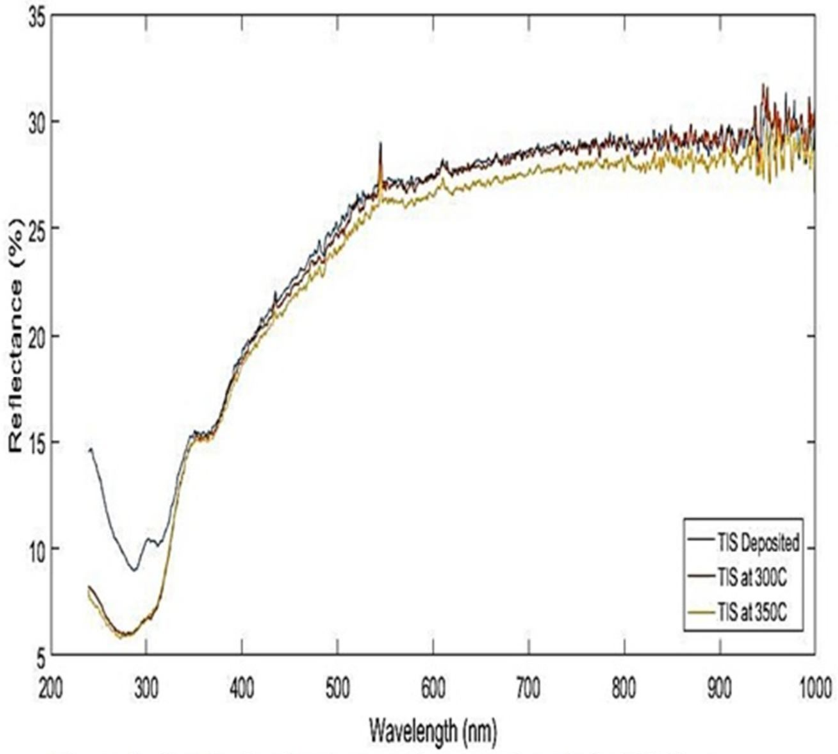

FIG. 1. Graph of reflectance against wavelength for TIS films.

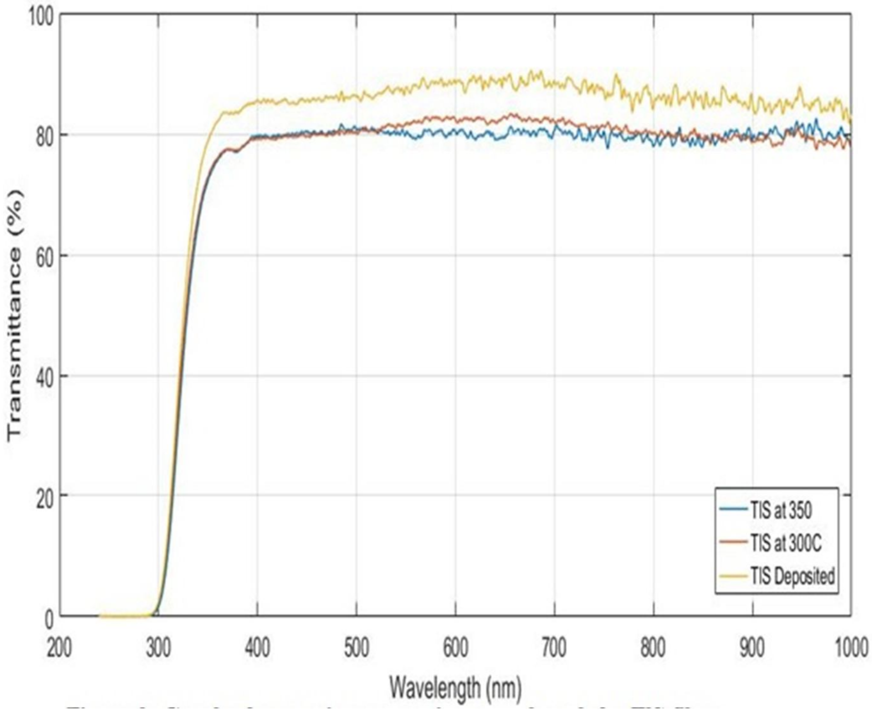

FIG. 2. Graph of transmittance against wavelength for TIS films.

In Fig. 3, it is obvious that TlS thin films have good absorbance in the short wavelength region. Records of about 3.25 %, 3.28 % and 3.3 % were obtained for films deposited, annealed at 300 °C and annealed at 350 °C, respectively [8]. The absorbance values for all the films were calculated from transmittance and reflectance data using the expression [9]:

$$T + R + A = 11$$

So that $A = 1 - [T + R]$

where;

$T = percentage\ transmittance,$

$R = percentage\ reflectance\ and$

$A = absorbance.$

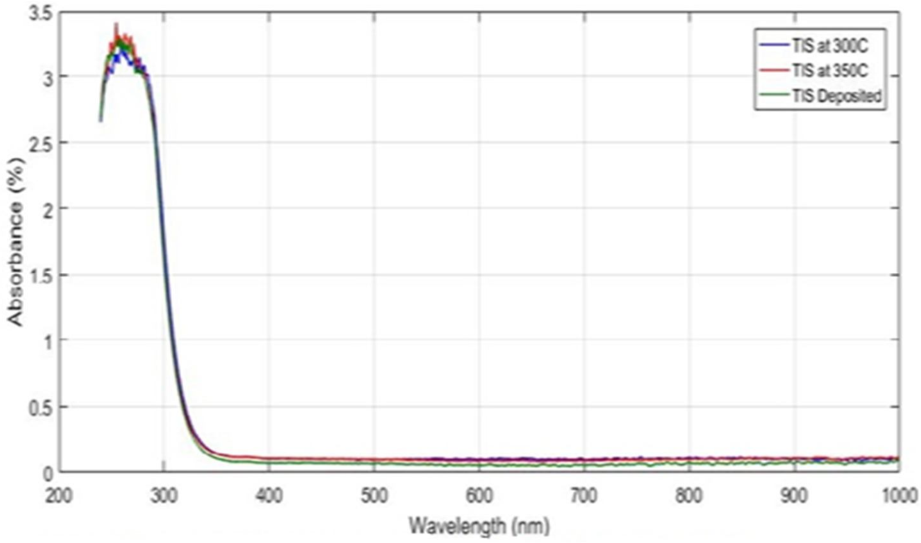

FIG. 3. Graph of absorbance against wavelength for TIS films.

The absorption decreased with increasing wavelength of solar radiation. Increase in absorption occurs when the photon energy reaches the value of the energy gap where electron transfers occur between the valence band and the conduction band. The lowest absorbance of 0.2 % was recorded for TlS deposited film, while the highest of 0.25 % was recorded for TlS film annealed at 350 °C at a wavelength of 900 nm.

The energy band-gaps of the films were relatively high. The values obtained were 3.9 eV, 3.92 eV and 3.94 eV, respectively for films deposited, annealed at 300° C and annealed at 350° C. These band-gap values speak in the same direction as the results of [10] obtained in the determination of optical properties of ZnS thin films which were in the range from 3.64 eV to 4.00 eV. Band gaps were obtained by plotting $(\alpha hv)^2$ against (*hv*) and extrapolating the linear part. By extrapolating the linear portions of the plots of $(\alpha hv)^2$ against (hv) to where $(\alpha hv)^2 = 0$, the value where the extrapolated line cuts energy (hv) axis indicates the band gap [11]. The band gap of the window layer should be as high as possible and the layer should be as thin as possible to maintain low-series resistance [12]. That condition certifies the need for window layer which should not absorb any of the incident light but allows maximum photon energy to reach the absorber layer where the energy is needed for generation of electrons. Fig. 4 shows the energy band-gap graphs for TlS films deposited and annealed samples at 300 °C and 350 °C, respectively.

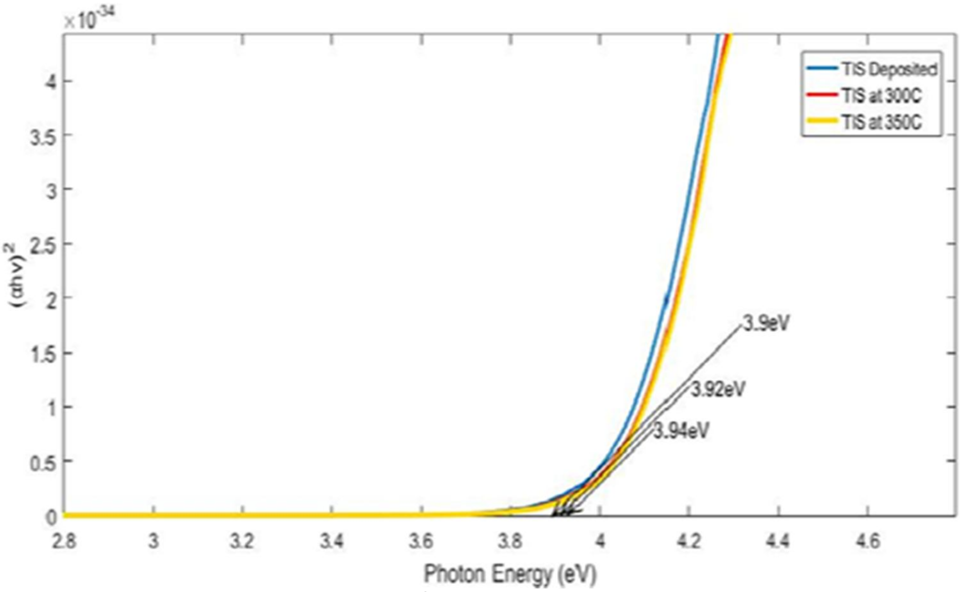

FIG. 4. Graph of $(\alpha hv)^2$ against wavelength for TIS films.

Electrical Properties of TlS Thin Films

The TlS samples were examined with the four point probe (FPP) machine for measurement of film current and voltage. The values for the sheet resistance (R_s), resistivity (ρ) and conductivity (σ) are presented in Table 1. The resistivity reduces from 2.003×10^6 Ωm to 0.34×10^6 Ωm for deposited and annealed at 350 °C samples as the annealing temperature increases. The corresponding conductivity increased from 4.99×10^{-7} Sm^{-1} to 2.92×10^{-6} Sm^{-1}. This enhances the electrical property of the film and makes it useful material for solar applications [13].

TABLE 1. Electrical properties of TlS

Sample	Voltage (V)	Current (A)	Sheet Resistance, Rs (Ωm^{-2})	Resistivity (Ωm)	Conductivity (Sm^{-1})
Deposited	1.32×10^{-1}	5.86×10^{-8}	1.001×10^{7}	2.003×10^{6}	4.99×10^{-07}
Annealed at 300 ° C	3.04×10^{-1}	4.81×10^{-8}	2.87×10^{7}	5.74×10^{6}	1.74×10^{-07}
Annealed at 350 ° C	2.79×10^{-1}	7.41×10^{-7}	1.71×10^{6}	0.34×10^{6}	2.92×10^{-06}

Conclusion

Thallium sulphide thin films have been successfully deposited by CBD in the laboratory. The transmittances of the films vary between 80 % and 90 % with a reduction in transmittance as the annealing temperature increases. This is an indication that good solar materials could be obtained at low temperatures. The film for TlS annealed at 350 ° C had the lowest reflectance of about 28 % compared to the deposited one which has 30 %, showing that annealing at higher temperature reduces the reflectance characteristics. The energy band gaps of the films were relatively high. The values obtained were 3.9 eV, 3.92 eV and 3.94 eV, respectively as annealing temperature increased. This implies that the films will be good materials for window layers in solar applications. The resistivity reduces from 2.003×10^6 Ωm to 0.34×10^6 Ωm as the annealing temperature increases, while the corresponding conductivity increased from 4.99×10^{-7} Sm^{-1} to 2.92×10^{-6} Sm^{-1}. This enhances the electrical property of the film and makes it useful as a material for solar applications.

It is hereby recommended that further investigations be done on the effect of concentration of the deposition bath on the quality of the films obtained for enhanced performance.

References

[1] Estrella, V., Mejia, R., Nair, M.T.S. and Nair, P.K., Modern Physics Letters B, 15 (17 n19) (2001) 737.

[2] Mane, R.S., Sankapal, B.R. and Lokhande, C.D., Mater. Chem. Phys., 65, 60 (2) (2000) 196.

[3] Janickis, V., Ancutienė, I., Bružaitė, I. and Jasulaitienė, V., Material Science, 10 (3) (2004) 231.

[4] Estrella, V., Nair, M.T.S. and Nair, P.K., Thin Solid Films, 414 (2002) 289.

[5] Afolayan, O.A. and Adeniji, Q.A., International Journal of Science and Research (IJSR), 7 (11) (2018) 1453.

[6] Wanjala, K.S., Njoroge, W.K. and Ngaruiya, J.M., International Journal of Energy Engineering, 6 (1) (2016) 1.

[7] Kumar, T. and Sankaranarayanan, S., Chalcogenide Letters, 6 (2009) 555.

[8] Ned Haluzan. http://solarword.blogspot.fi/2012/11/explaining-working-principle-of.html. (2012).

[9] Adeniji, Q.A., Ph.D. Thesis, Olabisi Onabanjo University, Ago-Iwoye, Nigeria, (2018).

[10] Rahdar, A., Arbabi, V. and Ghanbari, H., World Academy of Science, Engineering and Technology, 61 (2012) 657.

[11] Leshi, D.A., M.Sc. Dissertation, Olabisi Onabanjo University, Ago-Iwoye, Nigeria, (2019).

[12] Babatunde, R.A., M.Sc. Dissertation, Olabisi Onabanjo University, Ago-Iwoye, Nigeria, (2017).

[13] Adeniji, Q.A., Odunaike, K., Fowodu, T.O. and Talabi, A.T., NanoWorld J., 5 (4) (2020) 49.

Volume 14, Number 3, 2021. pp. 255-265

Jordan Journal of Physics

ARTICLE

Effect of Sr - Transition Metal Substitution on Electronic and Mechanical Properties of Mg_2Si: A DFT Study

A. S. Olayinka[a], **O. E. Odeyemi**[b] and **T. C. Olayinka**[c]

[a] *Department of Physics, Edo State University, Uzairue, Edo State, Nigeria.*

[b] *Department of SLT, Federal College of Animal Health and Production Technology, Ibadan, Nigeria.*

[c] *Department of Mathematical & Physical Sciences, Samuel Adegboyega University, Ogwa, Nigeria.*

Doi: **https://doi.org/10.47011/14.3.8**

Received on: 02/07/2020; *Accepted on: 6/10/2020*

Abstract: Recently, magnesium alloys have attracted scientific interest due to their technological importance in thermoelectric, piezoelectric, photo-voltaic and infrared photonics applications. The electronic and elastic properties of MgXSi (X = Mg, Sr) compounds were investigated in this work, using the density functional theory (DFT) with pseudo-potential plane-waves (PPW) approach as implemented in Quantum Espresso code. The results of the elastic constants of Mg_2Si are in agreement with the previous theoretical results and favourably compared with experimental data. The electronic band structures of these semiconductors were calculated to give narrow indirect and direct band gaps of Mg_2Si and MgSrSi, respectively. Our results show that the two compounds are mechanically stable. The Pugh's ratio, B/G, indicated that Mg_2Si and MgSrSi are brittle and ductile in nature. The estimated anisotropy parameter, A, shows that Mg_2Si has a higher degree of elastic isotropy in comparison to MgSrSi. Three-dimensional (3D) projection of Young's modulus and area modulus of the compounds was presented.

Keywords: Electronic structure**,** Elastic constants, Mechanical properties, Mg_2Si, MgSrSi.

PACS: 31.15.A-, 62.20.F-, 71.55.-i, 71.20.Be.

Introduction

Magnesium has recently become an important engineering material due to its abundance in the earth, less toxicity and cost-effectiveness compared to other competing materials for various technological applications [1, 2]. This has led to continuous and significant studies of magnesium-based alloys and compounds in the recent years due to their potentials for use in several technological applications, such as; thermoelectric, piezoelectric, photo-voltaic and infrared photonics [2, 3, 4]. Magnesium also possesses many other attractive properties, such as high damping capacity, electromagnetic shielding, thermal conductivity, good machinability and high recycling potential [2]. Moreover, Mg-based alloys are of great interest due to its low density (~1.74 g/cm^3) and high specific strength and stiffness compared to many other engineering materials, like steel, aluminium and polymer-based composites [5]. Magnesium alloys have been known to be among the lightest structural materials and have applications in several areas, like aerospace manufacturing and automobile industry [6, 7]. All these aforementioned attributes and features are our motivation to study these alloys.

Corresponding Author: A. S. Olayinka **Email**: akinola.olayinka@edouniversity.edu.ng

Several studies have been carried out on the mechanical alloy of tin (Sn) into magnesium silicide (Mg_2Si) to display better-detailed properties and thermoelectric properties than Mg_2Si. Difficulties encountered during the experimental set up include variations in temperature of the constituent elements and contamination in material processing [8, 9]. Magnesium silicide is one of the prominent silicides in solid-state application due to its compatibility with silicon, which is a based material for solid-state devices and electronics. This material has high thermal stability as well as desirable oxidization resistance properties, which makes it fit as a green material for semiconductor applications. This material is also known as a semiconductor with a narrow band gap, which has been used at a wavelength range of 1.2 to 1.8 micrometers as an infrared detector [8-10]. Doping and alloying have been used to enhance properties of semiconductors for optimum applications in optoelectronics and energy generation [11-13]. Elastic properties of the Mg_2Si structure under pressure have been reported by Zhang et al. (2018). Their calculated elastic constants are stable at a minimal pressure range of 0 to 7 GPa under Born's stability conditions at low pressures [9]. Hao et al. (2009) reported the experimental measurement of the compressive-to-phase transformation characteristics of Mg_2Si at room temperature [14]. Some works of literature only report elastic constants and Young's modulus, leaving out other elastic properties in their work. In this work, we present first-principle calculations of structural, mechanical and elastic properties of MgXSi (X = Mg, Sr) in antifluorite face-centered cubic (FCC) structure. The elastic constants, bulk modulus B, Young's modulus E, shear modulus G, Poisson's ratio, Zener's anisotropy A and Pugh's ratio B/G of Mg_2Si and MgSrSi are computed and discussed. The results are compared with available experimental and theoretical results.

Computational Details

Our calculations were carried out using plane-wave density functional theory (DFT) [15] using the Projected Augmented Wave (PAW) PBE functional which defines the exchange-correction energy. A projected augmented wave (PAW) type of pseudopotentials was employed. The pseudo-potentials used in the modeling of these materials are Mg.pbe-spn-kjpaw_ps l.1.0.0.UPF, Si.pbe-n-kjpaw_ps l.1.0.0.UPF and Sr.pbe-spn-kjpaw_ps l.1.0.0.UPF. The calculation of the pseudopotential involves *Mg:* $2p^6\ 3s^2$ *and Si:* $3s^2\ 3p^2$ *and Sr:* $4p^6 5s^2$ orbitals. Relaxation of the atomic structures was carried out using the Broyden-Fletcher-Goldfarb-Shanno method [16]. Brillouin zone is sampled using Monkhorst–Pack scheme [17] with a k-point grid of 8 x 8 x 8. The computations were carried out using thermo_pw [18] on the Quantum Espresso (QE) code [19-21]. The elasticity of the compounds was post-processed and analyzed (Self-consistent Elasticity of Multi-phase Aggregates (SC-EMA) code [22-24] and EIAM code [25].

Results and Discussion

Structural and Electronic Properties

The atomic structures of Mg_2Si and MgSrSi intermetallic compounds are known to crystallize in FCC lattice and the space group 225 $Fm\bar{3}m$ of antifluorite structural type. The atom of Si is located at the (0, 0, 0) sites in a primitive cell and two equivalent Mg atoms occupy the (a/4) (1, 1, 1) and (3a/4) (1, 1, 1) sites, where *a,* is the lattice constant [26]. The schematic diagrams of the crystal structures of these alloys are shown in Fig. 2 and their X-ray diffraction patterns are shown in Fig. 3. Interaction of X-rays (a spectrum of electromagnetic wave) with a crystalline substance results in a diffraction pattern which helps in the description of the crystal properties. X-ray diffraction is useful in crystal structure characterization, as well as obtaining useful crystal information, like lattice constants, crystallite size and degree of graphitization [27]. We calculated the electronic band structures of Mg_2Si and MgSrSi compounds at their equilibrium lattice constants, as shown in Figs. 4 and 5, respectively. For both compounds studied, the electronic band structure of Mg_2Si shows an indirect band gap of 0.39eV between Γ - X with the Maximum Valence Band (MVB) observed at gamma point, while the Conduction Band Minimum (CBM) is at the X point of the Brillouin zone (Fig. 4). The electronic band structure of MgSrSi depicts a direct band gap of 0.91eV with respect to the Fermi level and its Maximum Valence Band (MVB) and the Minimum Conduction Band (MCB) occurred at point X of the Brillouin zone (Fig. 5). The two compounds theoretically display semiconducting behaviour due to their narrow band gaps. The electronic band gap was increased with 0.52eV with the substitution of Sr for one atom of Mg from indirect band gap of Mg_2Si (0.39eV) to direct band gap of MgSrSi (0.91eV). The Brillouin zone representation for FCC Mg_2Si and MgSrSi is shown in Fig. 1.

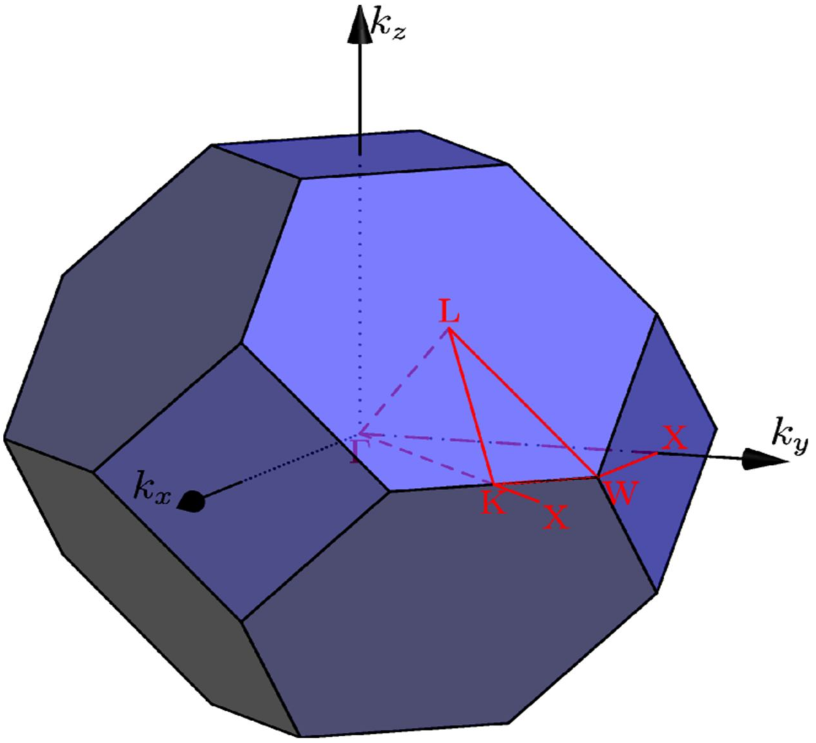

FIG. 1. Brillouin zone for FCC Mg_2Si and MgSrSi.

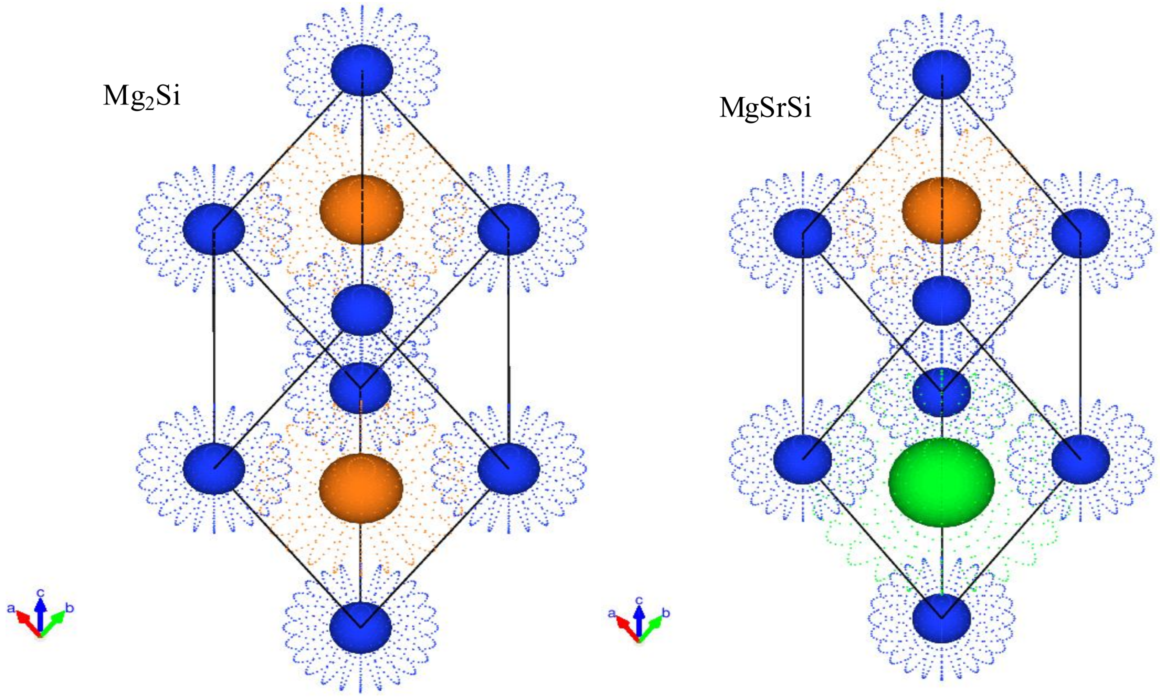

FIG. 2. Crystal structure of Mg_2Si and MgSrSi. Blue ball and gold ball represent Si and Mg, respectively, while green ball represents the substituted Sr atom for Mg.

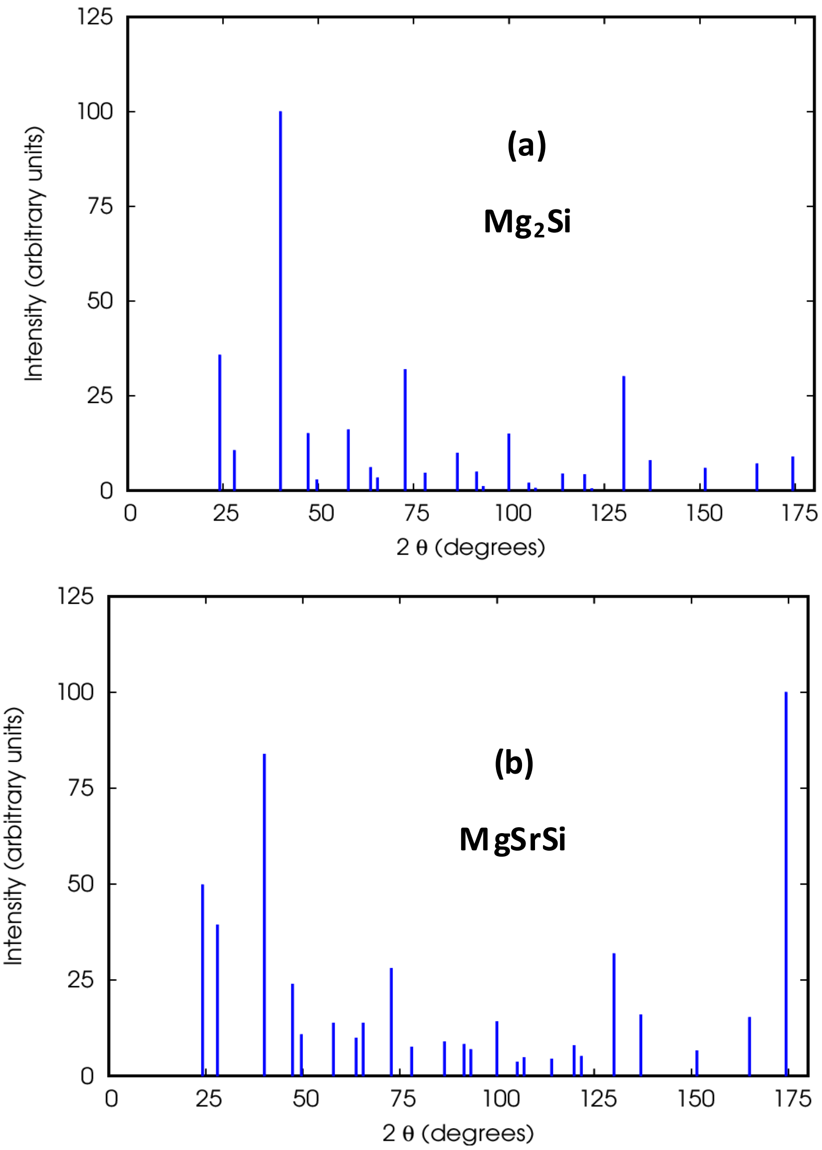

FIG. 3. X-ray diffraction pattern for Mg_2Si and MgSrSi.

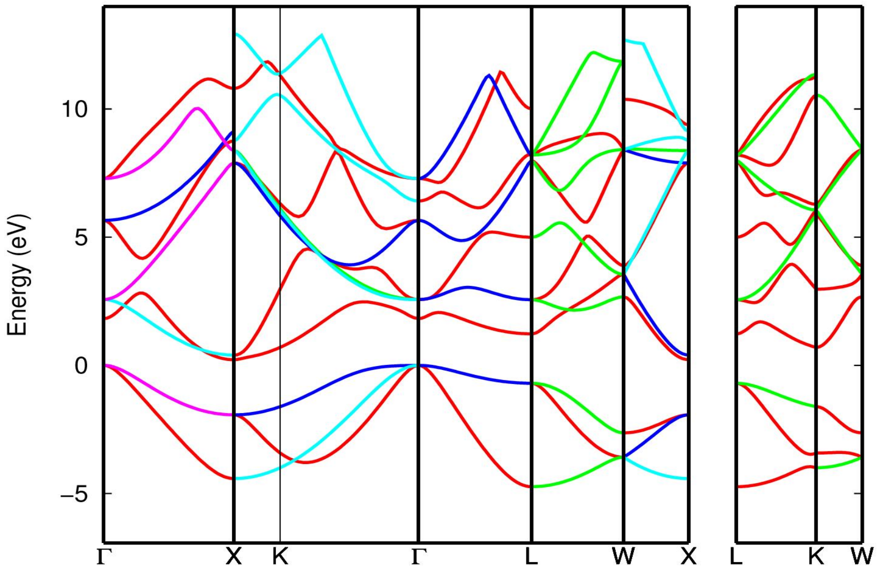

FIG. 4. Electronic band structure for Mg_2Si with an indirect band gap of 0.39eV between Γ and X.

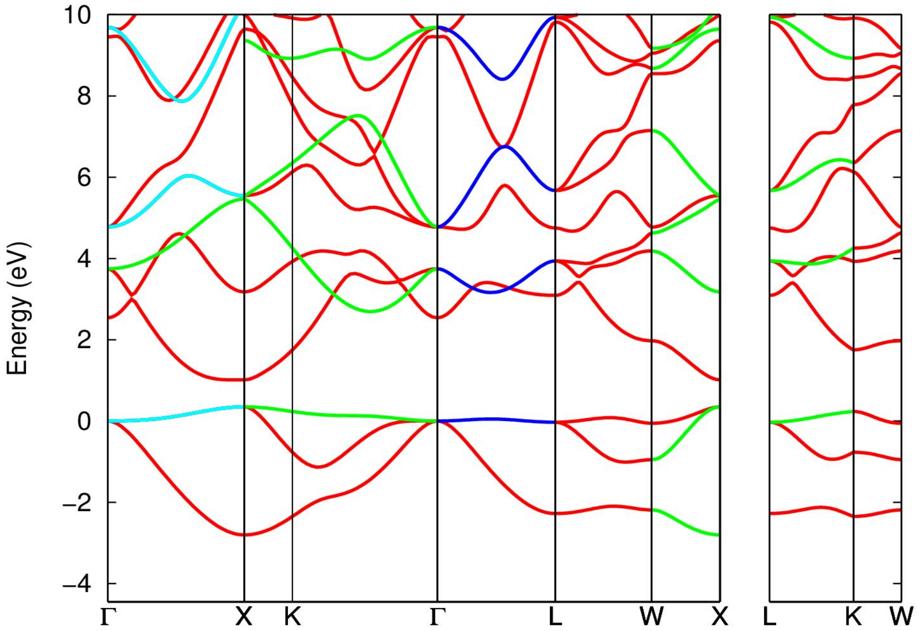

FIG. 5. Electronic band structure for MgSrSi with a direct band gap of 0.91eV at X point.

Elastic and Mechanical Properties

The elastic and mechanical properties of MgXSi (X = Mg, Sr) compounds were calculated and are shown in Table 1. Elastic constants (*Cij*) of any material play an important role in understanding its mechanical properties. C_{ij} are the elastic constants of the crystal and its structure has been fully relaxed under a given set of exchange-correlation potential functions and obtained an equilibrium structure with a minimum total energy. Before a material can be termed a mechanically stable material, the Born's stability conditions of cubic crystal [28] must be satisfied which are: $C_{11} > 0$, $C_{11} - C_{12} > 0$, $C_{44} > 0$, $C_{11} + 2C_{12} > 0$ and $C_{12} < B < C_{11}$. The results of C_{11}, C_{12} and C_{44} obtained as presented in Table 1 clearly show that the studied MgXSi (X=Mg, Sr) compounds are mechanically stable having satisfied the aforementioned conditions. The lattice constant, a = 6.341 Å and elastic parameters, C_{ij} (*GPa*) of Mg_2Si (C_{11} = 116.0 *GPa*, C_{12} = 22.6 *GPa* and C_{44} = 45.2 *GPa*) are in good comparison with the available theoretical [2, 25] and experimental data [29].

As it is well known, elastic properties such as bulk modulus (B) determine the resistance of any material fracture and the shear modulus (G) gives the resistance to plastic deformation. The B/G ratio, which is also described as Pugh's ratio, is used to understand the ductile/brittle behaviour of solids [30]. The critical value is 1.75, where greater than that value, the material is regarded as ductile [30, 31]. In this work, the B/G ratios of the two compounds were found to be 1.18 and 5.89 for Mg_2Si and MgSrSi, respectively. This shows that Mg_2Si alloy indicates brittle behavior, while MgSrSi is ductile in nature, based on their B/G ratios values.

The elastic anisotropy of crystals is an important factor in material science. There are different ways by which elastic anisotropy can be estimated theoretically. The Zener's anisotropy parameter $A = 2C_{44} / (C_{11} - C_{12})$ is usually adopted for this purpose [32, 33] . The degree of deviation of Zener's anisotropy parameter from unity (1) means the degree of elastic anisotropy. Mg_2Si is elastically isotropic with *A* = 0.96 and a little degree of elastic anisotropy is observed in MgSrSi with *A* = 0.42, as presented in Tables 1 and 2.

To calculate the polycrystalline modulus, two approximation methods are employed which are the Voight method and the Reuss method. Using energy considerations, Hill showed that the Voight and Reuss equations stand for upper and lower limits of realistic polycrystalline constants and recommended that a practical estimate of the bulk and shear moduli should be the arithmetic means of the extremes. Elastic properties (such as bulk modulus, shear modulus, Young's modulus and Poisson's ratio) are calculated through Equations (1) – (6) in the Voight-Reuss-Hill approximation and their values are presented in Table 2.

TABLE 1. Calculated elastic properties: The lattice constant *a* (Å), the elastic constants C_{11}, C_{12} and C_{44} (GPa), Young's moduli (*E*, in GPa), shear moduli (*G*, in GPa), Poisson's ratios (*v*), Zener's anisotropy A and the B/G ratio of MgXSi (X=Mg, Sr) compounds compared with other results.

Material	a (Å)	C_{11}	C_{12}	C_{44}	*E*	*G*	*V*	*A*	*B/G*
Mg_2Si	6.341*	116.0*	22.6*	45.0*	106.7*	45.6*	0.17*	0.96*	1.18*
	6.295^a	121.2^a	23.7^a	49.5^a	113.5^a	49.2^a	0.161^a	-	1.14^a
	6.35^b	118.82^b	22.27^b	44.96^b	111.79^b	46.25^b	0.15^b	-	1.18^b
	6.338^c	126.0^c	26.0^c	48.5^c	-	-	-	-	-
MgSrSi	6.361*	166.8*	67.2*	20.9*	48.07*	17.02*	0.42*	0.42*	5.89*

* = This Work a = [36] b = [2] c = [37]

TABLE 2. Calculated mechanical parameters' values of Mg_2Si and MgSrSi using Voight, Ruess and Hill approximations.

	Mg_2Si	**MgSrSi**
A	0.96	0.42
1-A	0.4	0.58
A_G	1.039	2.377
$B_V = B_R = B_H$ (GPa)	53.71	100.3
$\beta_V = \beta_R = \beta_H$ (10^{-3} /GPa)	6.2059	3.3211
G_V (GPa)	45.63	32.493
G_R (GPa)	45.62	27.27
G_H (GPa)	45.63	29.88
E_V (GPa)	106.69	87.985
E_R (GPa)	106.66	75.016
E_H (GPa)	106.67	81.552
ν_V	0.168	0.3539
ν_R	0.169	0.375
ν_H	0.169	0.365
B_V / G_V	1.18	3.087
B_R / G_R	1.18	3.678
B_R / G_R	1.18	3.357

A, anisotropy factor; A_G, anisotropy in shear moduli; B, bulk moduli; β, compressibility; G, shear moduli; E, Young's modulus; v, Poisson's ratio.

$$B = \frac{C_{11} + 2C_{12}}{3} \tag{1}$$

$$G_v = \frac{C_{11} - C_{12} + 3C_{44}}{5} \tag{2}$$

$$G_R = \frac{5(C_{11} - C_{12})C_{44}}{4C_{44} + 3(C_{11} - C_{12})} \tag{3}$$

$$G = \frac{G_v + G_R}{2} \tag{4}$$

where *B*, *G* and C_{ij} (C_{11}, C_{12} and C_{44}) are the bulk moduli, shear moduli and elastic parameters; G_V and G_R are Voigt's and Reuss's shear moduli, respectively. Hence, the Young's modulus *E* and the Zener's anisotropy factor *A* are computed as follows [34]:

$$E = \frac{9GB}{3B + G} \tag{5}$$

$$A = \frac{2C_{44} + 2C_{12}}{C_{11} - C_{12}} \tag{6}$$

Young's modulus, which is the ratio of strain to stress, is used to determine the stiffness of a material. On the other hand, area modulus is the ratio of an equibiaxial stress to the relative area change in the planes in which the stress acts. It is an intermediate elastic property between Young's modulus and bulk modulus, which is computed in isotropic elasticity [35]. The results computed in Table 2 show that Mg_2Si with E_H = (106.66 GPa) is stiffer than MgSrSi (E_H = 75.016 *GPa*). SC-EMA (Self-consistent Elasticity of Multi-phase Aggregates [22-24] and EIAM code [25] were used as post-processor for elasticity of Mg_2Si and MgSrSi to plot the three-dimensional (3D) image of area modulus and Young's modulus, as shown in Figs. 6 – 10. These Young's moduli are more intuitive than the bulk modulus to indicate the anisotropy of the crystals. These three-dimensional projections of Young's moduli indicate the directional dependences of the Young's moduli of the Mg_2Si and MgSrSi crystals. This result is consistent with the anisotropy factor given in

Table 1 with Mg_2Si is isotropic and MgSrSi crystal deviates a bit from isotropic behavior. Figs. 6 and 7 were generated using 200 data points each. Fig. 6 shows the 3D projection of Young's modulus and area modulus for Mg_2Si. The computed homogenized polycrystalline Young's modulus is 102.01 GPa, while the cubic single crystals 001, 110 and 111 planes' area moduli of elasticity were 59.89 GPa, 61.42 GPa and 61.85 GPa, respectively. Fig. 7 shows the 3D projection of Young's modulus and area modulus for MgSrSi. The computed homogenized polycrystalline Young's modulus is 82.81 GPa, while the cubic single crystals 001, 110 and 111 planes' area moduli of elasticity were 91.73 GPa, 53.17 GPa and 47.91 GPa, respectively. Fig. 8 shows the 3D and 2D projections of Poisson's ratio as computed for Mg_2Si and MgSrSi, respectively. Minimum and maximum dimensionless Poisson's ratios of 0.2 and 0.47 were measured for Mg_2Si with corresponding transverse maximum and minimum of (0.71 -0.70 0.00) and (0.00 0.00 -1.00), respectively along x y z. For MgSrSi, minimum and maximum dimensionless Poisson's ratios of 0.11 and 0.15 were recorded with corresponding transverse maximum and minimum of (0.71 -0.70 0.00) and (0.00 0.00 -1.00), respectively along x y z. Fig. 9 shows the 3- and 2- dimensional projections of shear modulus for Mg_2Si and MgSrSi, respectively. Shear modulus is one of the important quantities, as it determines the stiffness of a material. Computed shear moduli for Mg_2Si and MgSrSi were 45.63 GPa and 32.493 GPa, respectively, which compared well with our calculated homogenized polycrystalline shear moduli of 43.81 GPa and 30.53 GPa for Mg_2Si and MgSrSi, respectively using SC-EMA code [22-24]. Fig. 10 shows the 3D and 2D projections of sound velocities for Mg_2Si and MgSrSi, respectively. Minimum and maximum acoustic modes were 22.60 and 35.50 for Mg_2Si and 67.20 and 72.95 for MgSrSi, respectively. The acoustic modes for Mg_2Si and MgSrSi suggest that MgSrSi has a higher potential for acoustic application.

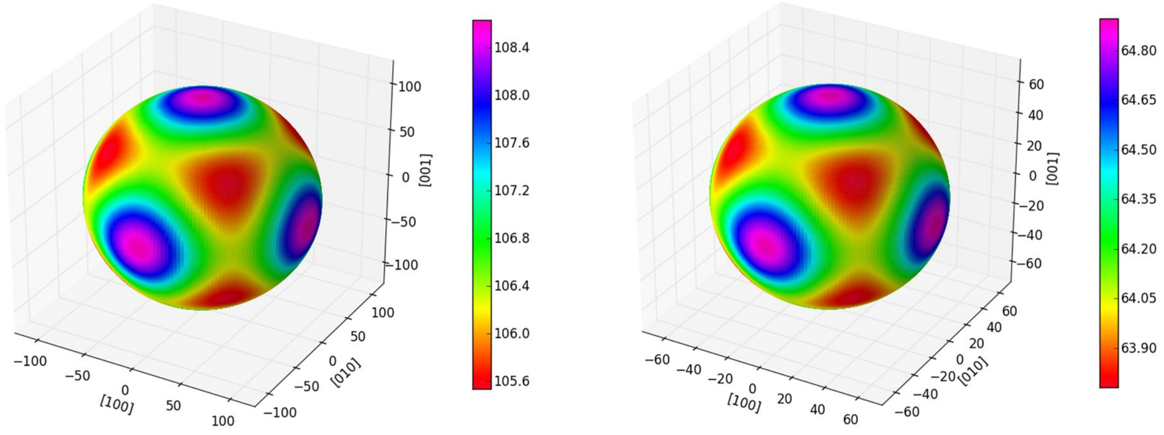

(a) (b)

FIG. 6. 3D projection for (a) Young's modulus and (b) area modulus of Mg_2Si.

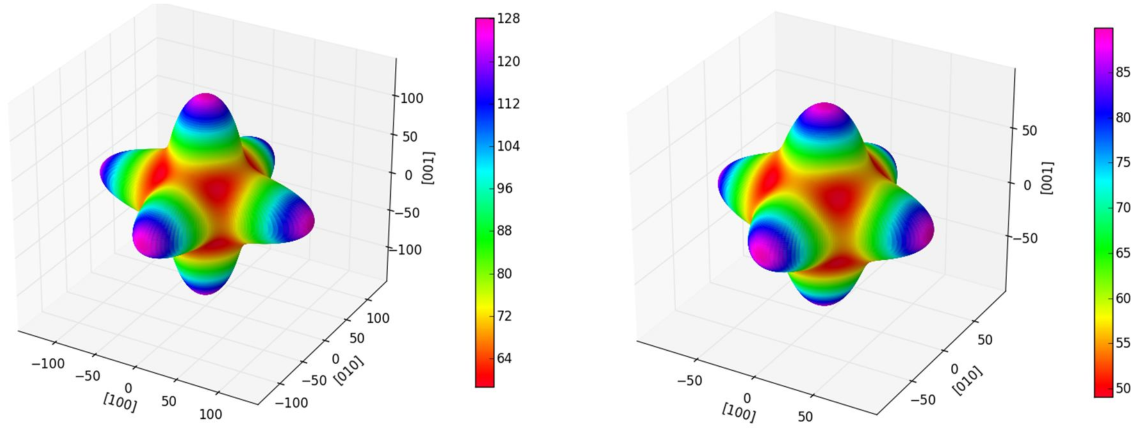

(a) (b)

FIG. 7. 3D projection for (a) Young's modulus and (b) area modulus of MgSrSi.

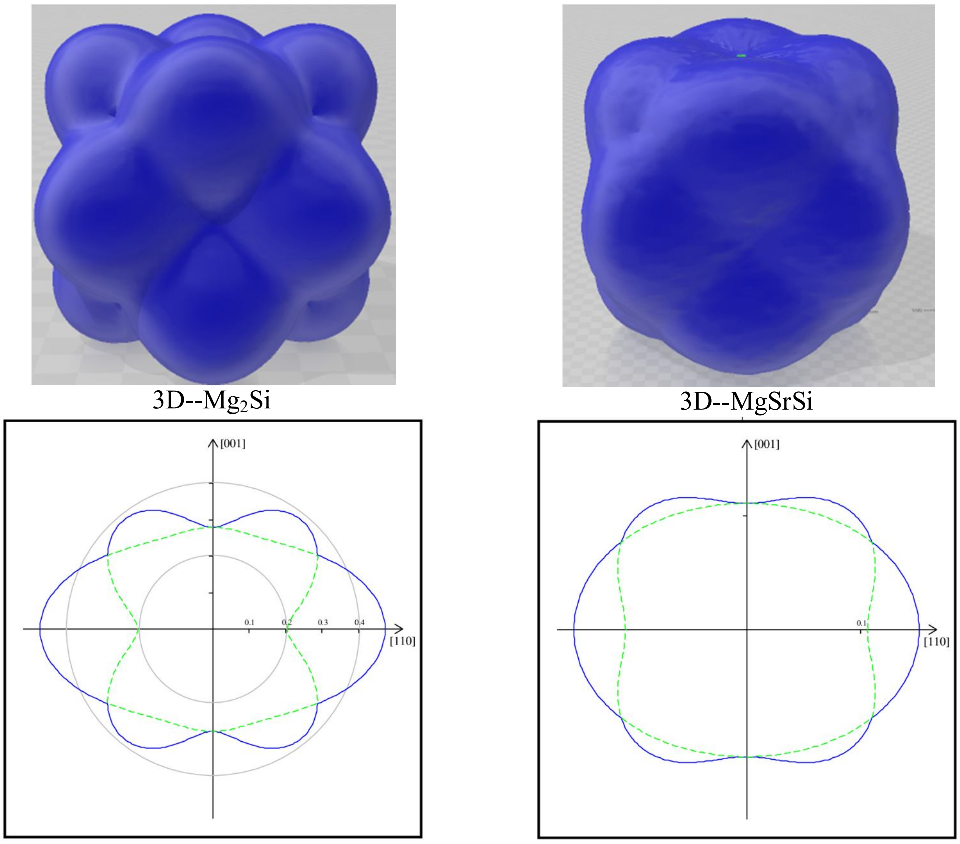

3D--Mg_2Si 3D--MgSrSi

2D--Mg_2Si 2D--MgSrSi

FIG. 8. 3D and 2D projections of Poisson's ratio for Mg_2Si and MgSrSi, respectively.

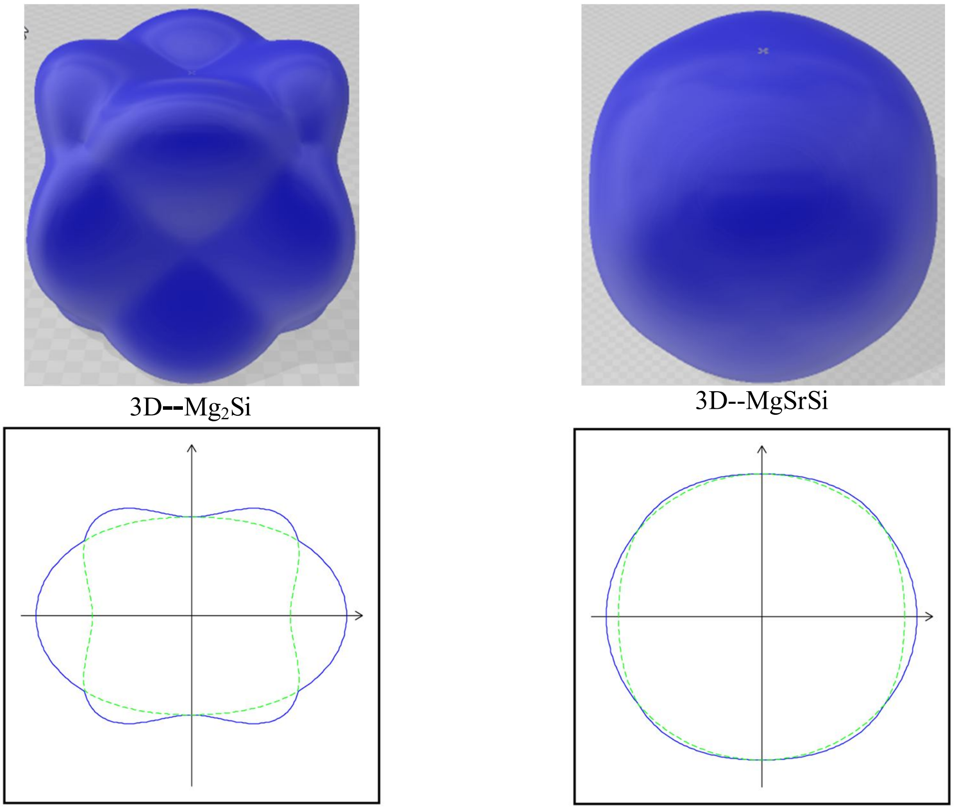

3D--Mg_2Si 3D--MgSrSi

2D--Mg_2Si 2D--MgSrSi

FIG. 9. 3D and 2D projections of shear modulus for Mg_2Si and MgSrSi, respectively.

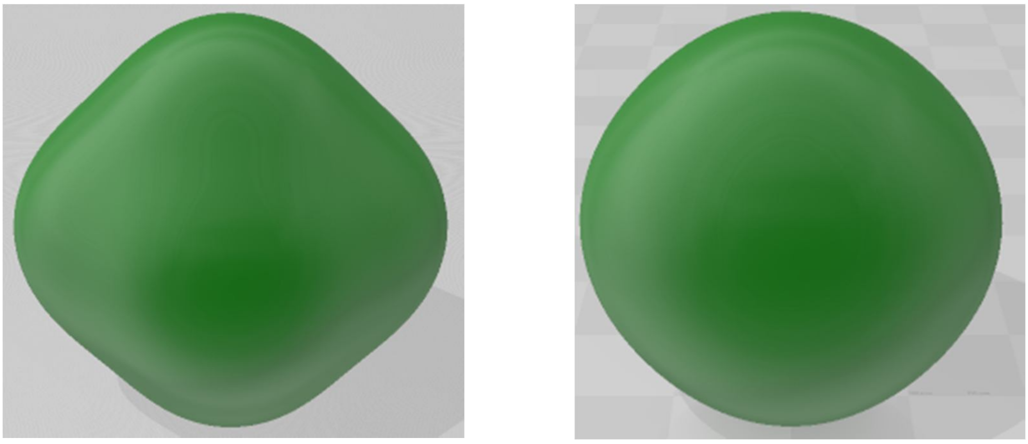

3D--Mg_2Si 3D--MgSrSi

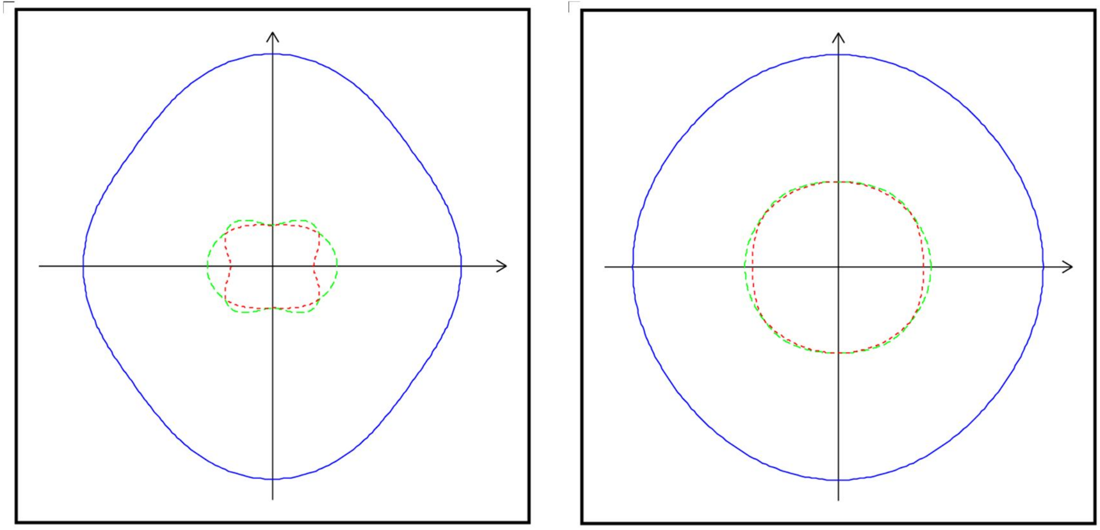

2D--Mg_2Si 2D--MgSrSi

FIG. 10. 3D and 2D projections of sound velocities for Mg_2Si and MgSrSi, respectively.

Conclusion

In the present theoretical study, the structural, elastic and mechanical properties of Mg_2Si and MgSrSi intermetallic compounds have been investigated employing the DFT with pseudo-potential plane-waves (PPW) approach using Projector Augmented Wave (PAW) method for the exchange and correlation potential. The results obtained for the optimized lattice parameter (a) agree with the available theoretical and experimental data. The elastic constants C_{ij} and related polycrystalline mechanical parameters, such as bulk modulus B, Young's modulus E, shear modulus G and Poisson's ratio, were computed. Zener's anisotropy parameter, A, and the B/G ratio were also estimated. From the results, it is concluded that the elastic constants of Mg_2Si are quite in good agreement with theoretical results already recorded on the subject and compare favourably with experimental data. The two compounds studied are mechanically stable having satisfied the elastic stability criteria. The three-dimensional Young's modulus of Mg_2Si also confirmed the computed results obtained by Zener's anisotropy factor A, which are nearly spherical, indicating that the crystal was isotropic. The studied compounds were classified as semiconducting materials having indirect band gap (0.39eV) and direct band gap (0.91eV) for Mg_2Si and MgSrSi, respectively in their electronic band structures.

References

[1] Liu, Y., Hu, W.C., Li, D.J., Zeng, X.Q. and Xu, C.S., Physica Scripta, 88(4) (2013) 045302.

[2] Na-Na, L., Ren-Bo, S. and Da-Wei, D., Chinese Physics B., 18 (5) (2009) 1979.

[3] Noda, Y., Kon, H., Furukawa, Y., Otsuka, N., Nishida, I.A. and Masumoto, K., Materials Transactions, JIM, 33 (9) (1992) 845.

[4] Schilz, J., Riffel, M., Pixius, K. and Meyer, H.J., Powder Technology, 105 (1-3) (1999) 149.

[5] Boucetta, S., Journal of Magnesium and Alloys, 2 (1) (2014) 59.

[6] Dieringa, H. and Kainer, K.U., “Magnesium and magnesium alloys”, In: “Springer Handbook of Materials Data”, 2nd Edn., (Springer, 2018).

[7] Kainer, K.U., “Magnesium: Alloys and Technology”, (Wiley-VCH Verlag GmbH & Co. KGaA, 2003).

[8] Li, S., Li, X., Dong, C. and Jiang, X., Acta Physica Sinica, 59 (6) (2010) 4267.

[9] Zhang, J., Ma, H., Zhao, B., Wei, Q. and Yang, Y., AIP Conference Proceedings, 1971 (2018) 020018.

[10] Saravanan, R. and Robert, M.C., Journal of Alloys and Compounds, 479 (1-2) (2009) 26.

[11] Olayinka, A.S., Adetunji, B.I., Idiodi, J.O.A. and Aghemelon, U., International Journal of Modern Physics B, 33 (06) (2019) 1950036.

[12] Olayinka, A.S., Idiodi, O.A.J. and Nwankwo, W., In: Covenant Journal of Physical & Life Sciences (CJPL), 7 (2) (2019) 2354.

[13] Olayinka, A.S. and Bamidele, O., Journal of Mat., 25625 (6) (2016) 235.

[14] Hao, J., Zou, B., Zhu, P., Gao, C., Li, Y., Liu, D., Wang, K., Lei, W., Cui, Q. and Zou, G., Solid State Communications, 149 (17-18) (2009) 689.

[15] Kohn, W., Becke, A.D. and Parr, R.G., Journal of Physical Chemistry, 100 (31) (1996) 12974.

[16] Fletcher, R., “Practical Methods of Optimization”, (Wiley Online Library, 2000).

[17] Monkhorst, H.J. and Pack, J.D., Physical Review B, 13 (12) (1976) 5188.

[18] Dal Corso, A., Journal of Physics: Condensed Matter, 28 (2016) 075401.

[19] Giannozzi, P., Baroni, S., Bonini, N., Calandra, M., Car, R., Cavazzoni, C., Ceresoli, D., … and Wentzcovitch, R., Journal of Physics: Condensed Matter, 21 (2009) 395502.

[20] Giannozzi, P., Andreussi, O., Brumme, T., Bunau, O., Buongiorno Nardelli, M., Calandra, M., Car, R., … and Baroni, S., Journal of Physics: Condensed Matter, 29 (2017) 465901.

[21] Giannozzi, P. and Cavazzoni, C., Nuovo Cimento Della Societa Italiana Di Fisica C., 32 (2) (2009) 49.

[22] Friák, M., Counts, W.A., Ma, D., Sander, B., Holec, D., Raabe, D. and Neugebauer, J., Materials, 5 (10) (2012) 1853.

[23] Titrian, H., Aydin, U., Friák, M., Ma, D., Raabe, D. and Neugebauer, J., Materials Research Society Symposium Proceedings, 1524 (2013) Mrsf12-1524-rr06-03.

[24] Zhu, L.F., Friák, M., Lymperakis, L., Titrian, H., Aydin, U., Janus, A.M., Fabritius, H.O., Ziegler, A., Nikolov, S., Hemzalová, P., Raabe, D. and Neugebauer, J., Journal of the Mechanical Behavior of Biomedical Materials, 20 (2013) 296.

[25] Marmier, A., Lethbridge, Z.A.D., Walton, R.I., Smith, C.W., Parker, S.C. and Evans, K.E., Computer Physics Communications, 181 (12) (2010) 2102.

[26] Folland, N.O., Physical Review, 158 (1967) 764.

[27] Iwashita, N., Materials Science and Engineering of Carbon, 2016 (2016) 7.

[28] Born, M., Huang, K. and Lax, M., American Journal of Physics, 23 (1955) 474.

[29] Schmidt, R.D., Case, E.D., Giles, J., Ni, J.E. and Hogan, T.P., Journal of Electronic Materials, 41 (2012) 1210.

[30] Pugh, S.F., The London, Edinburgh and Dublin Philosophical Magazine and Journal of Science, 45 (367) (1954) 823.

[31] Bannikov, V.V., Shein, I.R. and Ivanovskii, A.L., Physica Status Solidi - Rapid Research Letters, 1 (3) (2007) 89.

[32] Gschneidner, K., Russell, A., Pecharsky, A., Morris, J., Zhang, Z., Lograsso, T., Hsu, D., Lo, C.H.C., Ye, Y., Slager, A. and Kesse, D., Nature Materials, 2 (2003) 587.

[33] Yang, Y., Lu, H., Yu, C. and Chen, J.M., Journal of Alloys and Compounds, 485 (1-2) (2009) 542.

[34] Zener, C.M. and Siegel, S., Journal of Physical and Colloid Chemistry, 53 (9) (1949) 1468.

[35] Scott, N.H., Journal of Elasticity, 58 (3) (2000) 269.

[36] Tani, J.I. and Kido, H., Computational Materials Science, 42 (3) (2008) 531.

[37] Madelung, O., "Landolt-Börnstein: Numerical Data and Functional Relationships in Science and Technology - New Series", (Group III, Vol. 17e, Springer-Verlag, Berlin, 1983).

Volume 14, Number 3, 2021. pp. 267-274

Jordan Journal of Physics

ARTICLE

Assessment of Natural Radioactivity in Some Soil Samples from Kutha District in Babylon Governorate, Iraq

Mohanad H. Oleiwi

Department of Physics, College of Education for Pure Sciences, University of Babylon, Iraq.

Doi: **https://doi.org/10.47011/14.3.9**

Received on: 09/08/2020; *Accepted on: 14/10/2020*

Abstract: The activity concentrations of natural radionuclides of the elements (^{40}K, ^{238}U and ^{232}Th), collected from Kutha district of Babylon governorate are studied and evaluated. Twenty soil samples with (0-15) cm in depth are collected. Gamma spectrometer NaI (TI) source is used for calibration. The radioactivities of natural isotopes K-40, U-238 and Th-232, were assessed. These studies show that radio activities of isotopes are acceptable according to the standard levels. Also, the activity of radium equivalent, the rate of annual effective dose, average air volume and external risk index are evaluated. The results are found within the internationally tolerable values. The results show that the mean of the radioactivity of ^{238}U is (19.1565)Bq / kg, while it is (54.501) Bq/kg for ^{232}Th and (179.578) Bq/kg for ^{40}K. The study results showed that the average of radiological effects, like the Radium equivalent (Ra_{eq}), the rate of absorbed dose (Dr), the index of external hazard (H_{ex}), the index of internal hazard (H_{in}), the index of representative gamma hazard (I_γ), the Annual Effective Dose Equivalent (AEDE) and the Excess Lifetime Cancer Risk (ELCR) are as follow: 110.920 Bq/kg, 50.1838 nGy/h, 0.29953, 59.1530, 27.996, 0.34 mSv/y and 1.268×10^{-3}, respectively.

Keywords: Natural radioactivity, Absorption, External hazard, Effective annual dose, Excess lifetime cancer risk.

Introduction

As a fact of life, the human lives in a medium of natural radioactive materials, where humans are exposed daily to beta, alpha and gamma radiations. The traces of radioactive materials can be easily found in nature, including water, soils, and plants [1]. A crucial source of natural radioactivity of the materials exists in the crust of the earth [2]. Radiation rays are mainly categorized as natural and artificial radiations [3]. ^{238}U, ^{232}Th and ^{40}K are naturally occurring radionuclides which are considered as the sources of the natural radioactivity present in the soil, easily entering into the human body organs *via* food products, drinking water and forestry products. Almost 90% of human radiation exposure arises from natural sources, such as cosmic radiation, exposure to radon gas and terrestrial radiation [4]. The aim of this investigation is to assess the natural radioactivity of U-238, Th-232 and K-40 in different locations of Kutha district of Babylon. Different studies measured the natural radioactivity in soil and assessed its hazards for different regions around the Kutha district of Babylon as indicated in the references: [5], [6], [7], [8], [9] and [10]. The references mentioned showed different measurements in comparison with Kutha district.

Experimental Method

Twenty soil samples were collected with 15 cm in depth from different locations from Kutha district in Babylon governorate. The group has been guided by the standards recommended by the International Atomic Energy Agency (IAEA). Firstly, the soil samples were cleaned

Corresponding Author: Mohanad H. Oleiwi **Email**: mohanad.holeiwi@yahoo.com

by removing the undesired materials. Then, the samples were sun-dried for ten days. Thereafter, the samples were analyzed for the selection of homogeneous particle size using a cylinder sieve, 300 µm, with a net weight of 750 g. The samples were filled in cubic Marinelli cups with a constant size to ensure the homogenous distribution around the detector. The multivariate analyzer 1024 channel range was used for the surrounding by using ORTEC cylindrical chamber including two parts made of stainless steel and lead with widths of 20 and 5cm, respectively. The energy acquisition was calibrated using a set of radioactive standard source spectrometers, such as ^{60}Co, ^{137}Cs and ^{22}Na. The efficiency of energy was performed in a gamma spectrometer using these sources of calibration in a Marinelli cup applying a power in the range of 511.006 to 2500 keV. The process was followed by placing the calibration source in the detector with an exact geometry consort between the geometric sample and the sample detector. The sample has been placed in the centre of the chamber inside the shield for 4 hours. The equilibrium energy was determined as 1764 keV from gamma power transitions of ^{214}Bi with the probability of 15% and 2614 keV from gamma energy transfer of ^{208}Tl, with the probability of 98%. The activity of ^{40}K was balanced accordingly; however, the activity of ^{40}K was determined using a power of 1460 keV and a gamma-ray line probability of 12% was reported.

TABLE 1. Standard sources with energies and efficiency

No.	Source	Energy (keV)	Efficiency
1	Na-22	511	0.08413
		1274.5	0.04119
2	Cs-137	661.6	0.070137
3	Co-60	1173.24	0.02531
		1332.5	0.0225
		2505.74	0.004107

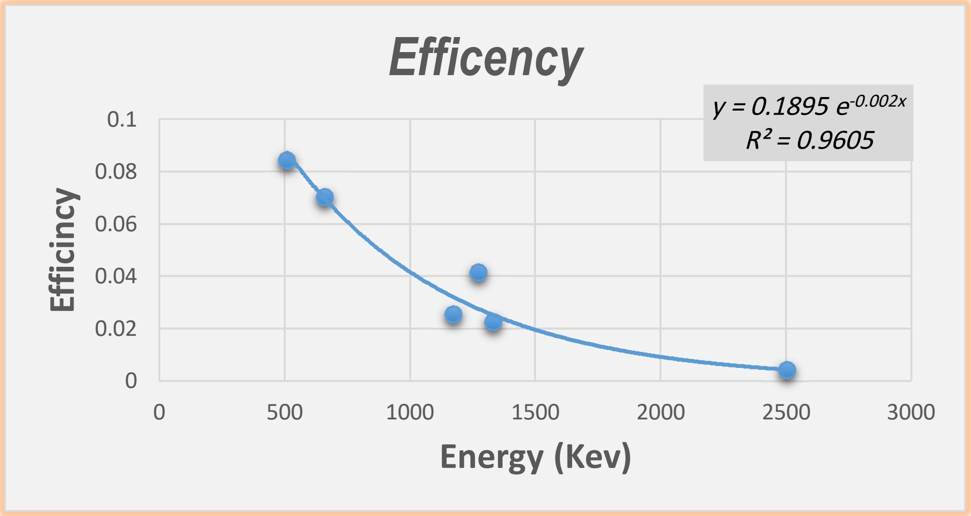

FIG. 1. The relationship between efficiency and energy.

Through the above figure, it is clear that the relationship between efficiency and energy is represented by the following equation:

$$\varepsilon = 0.1895\, e^{-0.002x}$$

where Ɛ is representing the efficiency and E is the energy of radiation source.

Theoretical Calculations

Specific Activity (S_A)

The qualitative (specific) activity (S_A) can be measured by Eq. (1):

$$S_A = \frac{n}{\varepsilon \times m \times I_\gamma \times \tau} \qquad (1)$$

where n is the counts per second of gamma, ε is the detector efficiency, I_γ is the intensity of gamma line in the radionuclides, m is the mass of the sample in kilogram and τ is the lifetime of the collected spectrum measured in seconds [11].

The variation of specific activity with the sample number is shown in Fig. 2, Fig. 3 and Fig. 4 for Potassium-40, Uranium-238 and Thorium-232, respectively.

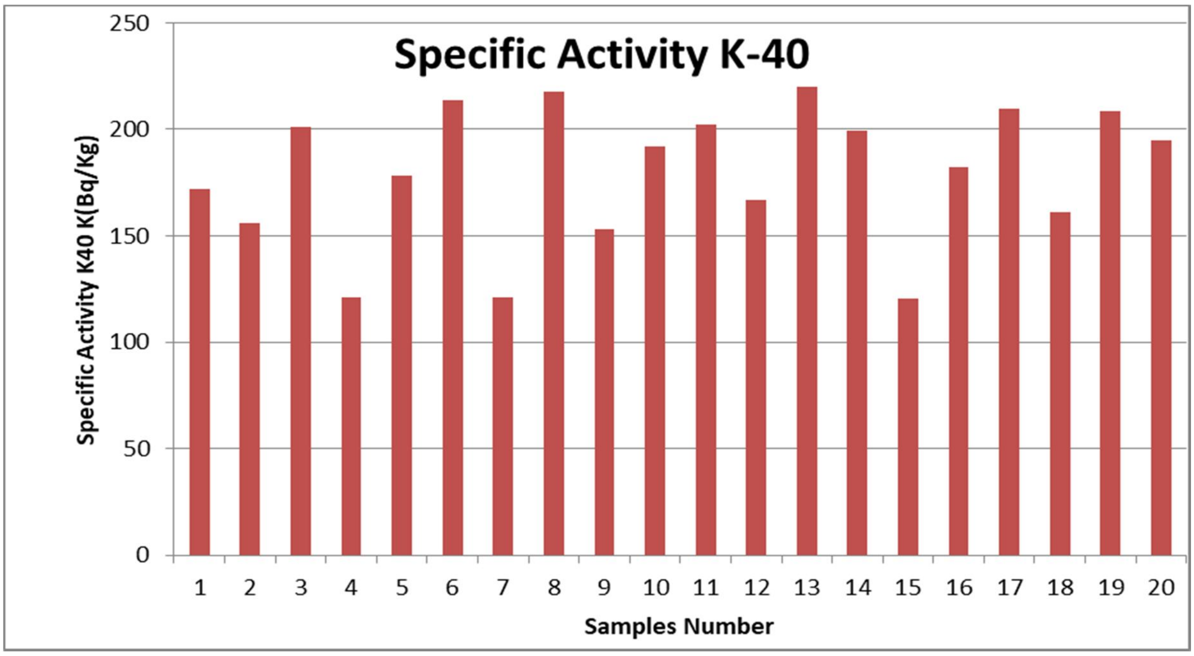

FIG. 2. The variation of specific activity of Potassium-40 with sample number.

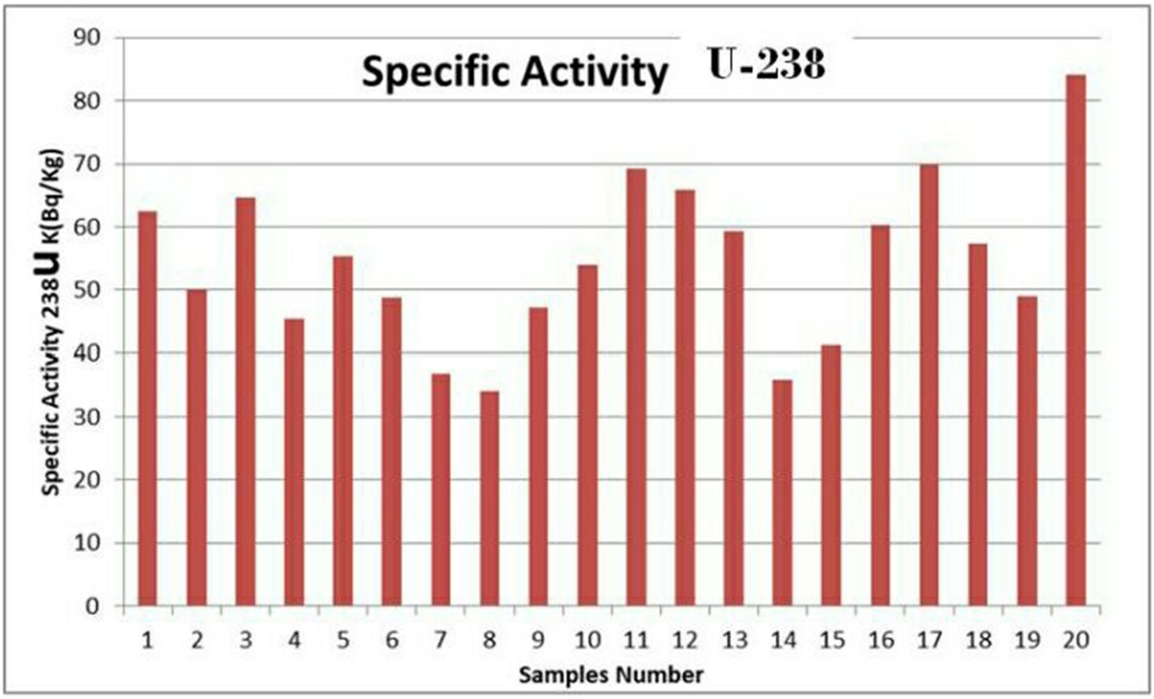

FIG. 3. The variation of specific activity of Uranium-238 with sample number.

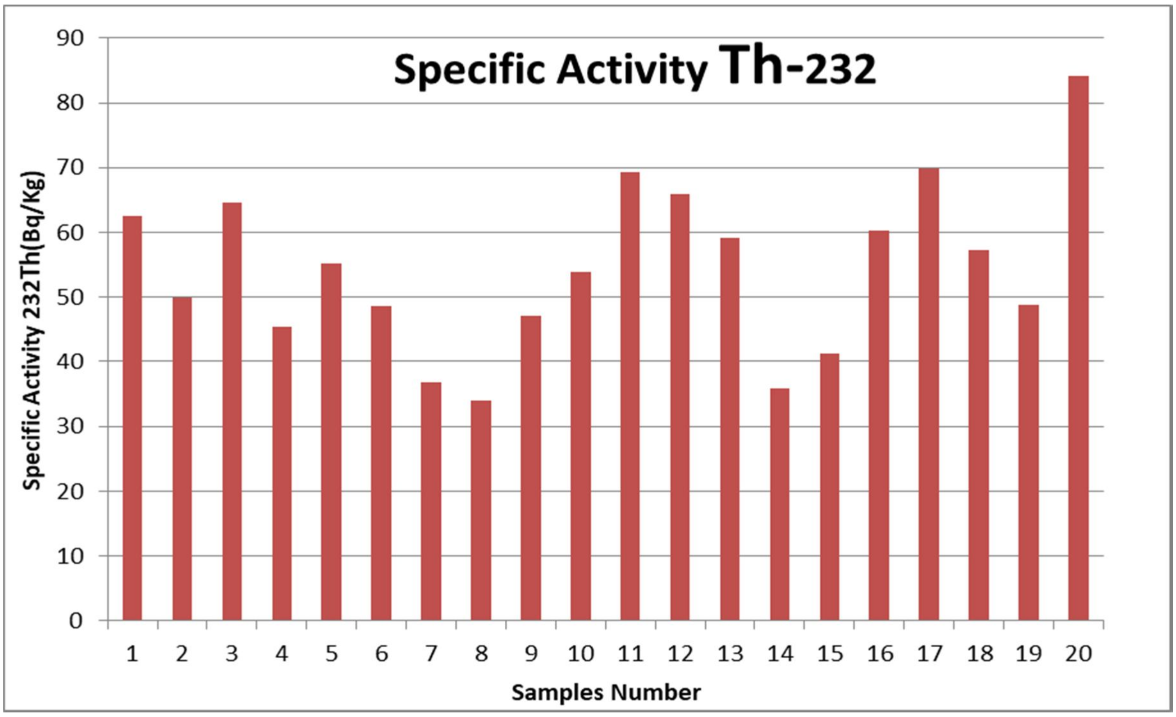

FIG. 4. The variation of specific activity of Thorium-232 with sample number.

Index of External Hazard (H(ex))

Measuring of hazard indices depends on the specific efficacies of Potassium-40, Uranium-238 and Thorium-232. Several risk factors have been measured, including:

The Equivalent of Radium-232 (Ra(eq))

It is used to obtain the sum of the activities of Th-232, U-238 and K-40 in (Bq/kg) unit and assesses hazards associated with materials which contain Th-232, U-238 and K-40 in (Bq/kg) by using the Radium Equivalent Activity that is defined in Eq. (2) [12]:

$$Ra(eq) = 1.43A_{Th} + A_U + 0.077A_K \quad (2)$$

where A_U is the specific efficiency of Uranium, A_{Th} is the specific efficiency of Thorium and A_K is the specific efficiency of Potassium series. In Eq. (2), it is assumed that 10 Bq/kg for Uranium, 7 Bq/kg for Thorium and 130 Bq/kg for potassium produce equal doses of radiation. The highest value of Ra_{eq} must be less than the global limit of 370 Bq/kg [13].

Absorbed Dose Rate in Air (AD)

The total rate of the absorbed air dose (AD) measures in terms of concentrations of terrestrial nuclei by Eq. (3) [14]:

$$AD(nGy/h) = 0.462\, A_U + 0.621\, A_{Th} + 0.0417\, A_K \quad (3)$$

Annual Effective Dose

The effective annual dose has been measured using Eq. (4) and Eq. (5) as follows [15]:

$$AEDE\ Indoor\ (mSv/y) = 0.8 \times 0.7\frac{Sv}{Gy} \times 10^{-6}AD\left(\frac{nGy}{h}\right) \times 8760h \quad (4)$$

$$AEDE\ Outdoor\ (mSv/y) = 0.7\frac{Sv}{Gy} \times 10^{-6}AD\left(\frac{nGy}{h}\right) \times 8760h \times 0.2 \quad (5)$$

The coefficient $0.7\frac{Sv}{Gy}$ is used as a coefficient of conversion from the dose of air absorbed to the annual effective dose received by an adult and 0.8 refers to the period spent inside and 0.2 is the proportion of period spent. 8760 refers to the number of hours in a year and the total average effective annual dose is 0.47 *mSv* [16].

External Hazard Index (H(ex))

The external hazard index is an assessment of the risk of natural gamma radiation, as explained in Eq.(6) [17]:

$$\mathrm{H(ex)} = \frac{A_U}{370} + \frac{A_{Th}}{259} + \frac{A_K}{4810} \quad (6)$$

H(ex) must be less than one. If H(ex) is greater than or equal to one, that indicates radiological hazard [18]. The internal exposures are the result of the inhalation of Radon-232, that can be expressed in terms of the factor of internal risk (H(in)) [19], which is calculated by Eq. (7) [20]:

$$\mathrm{H(in)} = \frac{A_U}{158} + \frac{A_{Th}}{259} + \frac{A_K}{4810} \tag{7}$$

H(in) should be less than one to be within the range of the internationally permissible limits [21].

Index of Activity Concentration (Iγ)

The representative level index (Iγ) of the soil is used to assess the gamma level radiation hazards associated with natural gamma emitters in the sample and can be evaluated using Eq. (8) [22]:

$$I\gamma = \frac{A_U}{150} + \frac{A_{Th}}{100} + \frac{A_K}{1500} \tag{8}$$

Lifetime Cancer Risk (ELCR)

The value of excess lifetime cancer risk can be calculated as in Eq. (9) [15]:

$$ELCR = RF \times AEDE \times DL \tag{9}$$

where ELCR is the excess lifetime cancer risk Sv^{-1}, DL is the average period of life that is estimated at seventy years, RF: risk factor, Sv; i.e., fatal cancer risk per sievert of random effect. ICRP uses an RF of 0.05.

Result and Discussion

Specific Activity

Table 2 displays the results of specific activity for U-238, Th-232 and k-40 radionuclides in samples from the district of Kutha, Babylon governorate. The activity of ^{238}U was (19.1565) Bq/kg as maximum. The activity of ^{232}Th was about (54.501) Bq/kg, and the activity of ^{40}K was (179.578) Bq/kg, while the geochemical composition of the soil was sandy soil. As we note, the activity of Thorium is larger than the activity of Uranium in most of the samples. The radioactivity of Th-232 in a part of the cases is larger than that of U-238 in samples collected from some locations.

It has been observed that radioactivity of K-40 was higher than those of U-238 and Th-232, which is due to the abundance of K-40 in some soil samples. The reason for this is the use of a great deal of potassium-containing fertilizers in the neighbourhood of the sample site. The results in this assessment show that the average radioactivity of the collected samples is lower than the total average values according to UNSCEAR 2017 [23]. The UNSCEAR 2017 has reported radioactivities of 420 for K-40, 33 Bq/kg and 45 Bq/kg for U-238 and Th-232.

TABLE 2. The natural radioactivity results in the centre of Kutha district if Babylon governorate.

Number	Sample symbol	S_A (1 Bq/kg)		
		K- 40	U- 238	Th- 232
1	S1	172.18±1.55	5.87±1.31	62.5±1.57
2	S2	156.18±2.28	7.42±0.72	49.91±2.50
3	S3	201.2±2.18	4.98±1.28	64.62±1.95
4	S4	121.05±2.81	11.12±0.92	45.36±2.88
5	S5	178.05±2.02	14.83±1.34	55.22±1.96
6	S6	213.6±2.77	15.15±0.73	48.72±2.05
7	S7	120.89±2.12	18.35±1.62	36.85±1.40
8	S8	217.67±3.03	16.97±1.07	33.98±2.38
9	S9	153.04±3.11	20.22±0.63	47.11±2.03
10	S10	192.13±3.77	25.13±0.43	53.91±2.11
11	S11	202.05±2.28	19.87±1.32	69.28±1.81
12	S12	167.11±3.31	22.12±0.63	65.88±2.12
13	S13	220.05±3.54	29.11±0.49	59.23±1.14
14	S14	199.17±3.00	23.91±1.9	35.81±2.19
15	S15	120.48±2.69	17.42±0.63	41.25±2.38
16	S16	182.23±3.31	20.71±1.23	60.28±2.01
17	S17	209.87±1.99	27.31±1.02	69.81±2.15
18	S18	161.39±2.88	30.48±1.91	57.23±1.02
19	S19	208.41±3.11	32.93±0.77	48.87±0.08
20	S20	194.81±2.77	19.23±1.99	84.2±1.09
Average ± S.D.		179.578	19.1565	54.501

The Results of Ra(eq), Dr, H(ex), H(in) and Iγ Parameters

Table 3 shows the results of Ra(eq), Dr, H(ex), H(in) and Iγ for the soil samples collected from Kutha city, Babylon governorate. The measured equivalent Ra-232 activity of the samples shows an average of (110.920) Bq/kg. The minimum activity value of 370 Bq/kg has been reported for the analyzed soil samples of Ra-232 [24]. According to UNSCEAR 2000, the rate of absorbed dose for the world's outdoor exposure due to gamma radiation (nG/h) is about 50.1838 nGy/h [23]. Recorded values in the region under study for many samples are necessary for health and the results obtained do not show any premalignant effects on people who live in Kutha. Finally, specific activity was used for detecting of the radioactivity doses and has been delivered externally in the form of γ dose. The index of external risk has been calculated and reported to be 0.29953, while according to the radiation protection report, the average value is less than one [24]. Those radionuclides have an internal exposure of about (27.996) and an index of representative gamma hazard of about (59.153038); so the calculated values are below one according to the radiation protection report [25]. The calculated values of the parameters under study are shown in Table 3. These values are lower than the international values [19-18-24]. The internal, external and total values of the (AEDE) are shown in Table 4. The mean value is (0.34) and the average of 0.459848 mSv/y does not correspond to the global value of 0.34183 mSv/y [25]. The results show an increase in the lifetime risk of cancer in these locations, which is represented in Table 3. These values have an average of 1.267 x 10^{-3}.

TABLE 3. The results of Ra(eq), Dr, H(ex), H(in) and Iγ of the samples from Kutha city, Babylon.

Number	Sample symbol	Ra(eq) (Bq/kg)	Dr (nGy/h)	H(ex)	H(in)	Iγ
1	S1	108.5028	48.7043	0.2929	0.3142	0.7789
2	S2	90.8171	40.9348	0.2452	0.2721	0.6526
3	S3	112.87	50.8198	0.3047	0.3228	0.8135
4	S4	85.3056	38.3537	0.2303	0.2706	0.6084
5	S5	107.5044	48.5677	0.2903	57.2607	27.1015
6	S6	101.2668	46.1615	0.2734	54.3501	25.7192
7	S7	80.3540	36.4026	0.2170	42.9002	20.3035
8	S8	82.3219	38.0185	0.2223	44.6752	21.1354
9	S9	99.3713	44.9787	0.2683	53.0140	25.0906
10	S10	117.0153	53.0999	0.3160	62.5620	29.6079
11	S11	134.4982	60.6283	0.3631	71.5040	33.8444
12	S12	129.1958	58.0994	0.3488	68.5464	32.4460
13	S13	130.7527	59.4067	0.3531	69.9796	33.1175
14	S14	90.4543	41.5898	0.2442	48.9041	23.1381
15	S15	85.6844	38.6883	0.2313	45.6169	21.5907
16	S16	120.9421	54.6008	0.3265	64.3804	30.4717
17	S17	143.2982	64.7208	0.3869	76.3081	36.1168
18	S18	124.7459	56.3515	0.3368	66.4387	31.4455
19	S19	118.8616	54.2526	0.3210	63.8640	30.2205
20	S20	154.6363	69.2960	0.4175	81.8001	38.7224
Average ± S.D.		110.920	50.1838	0.29953	59.153038	27.996

TABLE 4. The results of AEDE $_{indoor}$, AEDE $_{outdoor}$, AEDE and ELCR of samples from Kutha district in Babylon, Iraq.

Number	Sample symbole	AEDE $_{indoor}$ (mSv/y)	AEDE $_{outdoor}$ (mSv/y)	AEDE (mSv/y)	ELCR×10^{-3}
1	S1	0.2389	0.0597	0.2986	0.4778
2	S2	0.2008	0.0502	0.2510	0.4016
3	S3	0.2493	0.0623	0.3116	0.4986
4	S4	0.1881	0.0470	0.2351	0.3762
5	S5	0.1547	0.3308	0.3983	1.3909
6	S6	0.1468	0.3142	0.3779	1.3208
7	S7	0.1159	0.2479	0.2984	1.0422
8	S8	0.1207	0.2585	0.31056	1.0863
9	S9	0.1432	0.3063	0.3687	1.2879
10	S10	0.1690	0.3616	0.4351	1.5200
11	S11	0.1932	0.4130	0.4974	1.7367
12	S12	0.1852	0.3959	0.4769	1.6647
13	S13	0.1891	0.4045	0.4867	1.7003
14	S14	0.1321	0.2829	0.3400	1.1889
15	S15	0.1232	0.2635	0.3173	1.1080
16	S16	0.1739	0.3719	0.4479	1.5638
17	S17	0.2062	0.4409	0.5308	1.8536
18	S18	0.1795	0.3838	0.4622	1.6138
19	S19	0.1725	0.3693	0.4441	1.5521
20	S20	0.1825	0.4693	0.3441	1.2521
Average±S.D.		34..0	0.459848	0.34183	1.268

TABLE 5. The radioactivity of radionuclides in local studies and comparing them to the current study of soil samples from Kutha district in Babylon in Bq/kg units.

Sequence	Specific efficacy concentration (Bq/kg)			Study site	Source
	^{238}U	Th-232	K-40		
1	15.505	15.485	170.206	Iraq-Babylon	[26]
3	49.68±108	55.06±58.1	197.91±183.8	Iraq- (city of Hindia)	[27]
4	30.96±5.86	67.09±2.9	271.2±170	Iraq- Karbala	[28]
5	14.079 ± 0.46	12.326± 0.43	416.655 ± 2.86	Iraq- city of Hilla	[5]

Conclusion

The measurements of the natural radioactivity levels in Kutha district in Babylon governorate show normal concentration levels of radioactivity. The measured ^{40}K levels are within the natural permissible values. The values of Radium equivalent,(Ra$_{eq}$), annual effective dose equivalent and radiation hazard index (H$_{ex}$) refer to normal levels of radio activity.

References

[1] Saeed, Q.R., "Radiation Protection and Pollution", Iraqi Atomic Energy Organization Publication, (Arab House for Printing, 1968).

[2] Mould, R.F., "Century of X-rays and Radioactivity in Medicine, with Emphasis on Photographic Records of the Early Years", (Reprinted with minor corrections.). (Bristol: Inst. of Physics Publ., P. 12, 1995).

[3] L'Annunziata, M., "Handbook of Radioactivity Analysis", (Elsevier Science Publishers; Amsterdam, Netherlands, 2003).

[4] Kilic, A.M. and Aykamis, A.S., Earth and Environmental Science, Bulletin of Engineering Geology and Environment, 68 (3) (2009) 331.

[5] Abojassim, A.A., Oleiwi, M.H. and Hassan, M., Nuclear Physics and Atomic Energy, 17 (2016) 308.

[6] Oleiwi, M.H. and Rasool, W.S., Journal of Engineering and Applied Sciences, 13 (18) (2018) 7745.

[7] Yousif, S.A.R., Abojassim, A.A. and Hayder, A., Nuclear Physics and Atomic Energy, 20 (1) (2019) 60.

[8] Abojassim, A.A. and Rasheed, L.H., Int. J. Energy and Environ., 10 (2019) 143.

[9] Mustafa, R.K. and Oleiwi, M.H., J. Plant Archives, 19 (2) (2019) 3957.

[10] Kadhim, S.H., Zgair, I.A., Dosh, R.J., Rasheed, L.H. and Abojassim, A.A., Indian Journal of Public Health Research & Development,10 (1) (2019) 321.

[11] Cottingham, N. and Greenwood, D., "An Introduction to Nuclear Physics", 2nd edition, (Cambridge University Press, United Kingdom, 2001).

[12] Alaamer, A.S., Turkish Journal of Engineering & Environmental Sciences, 32 (2008) 229.

[13] Jassim, Z., Al-Gazaly, H.H. and Abojassim, A.A., J. of Environmental Science and Pollution Research, 2 (1) (2016) 39.

[14] European Commission (EC), "Radiological Protection Principles Concerning the Natural Radioactivity of Building Materials", (Radiation Protection, No.112, 1999).

[15] Organization for Economic Cooperation and Development, Report by a group of experts of the OECD Nuclear Energy Agency (Paris, France: OECD), (1979).

[16] El-Taher, A. and Makhluf, S., Indian Journal of Pure & Applied Physics, 48 (2010) 697.

[17] Mahur, A.K., Rajesh, K., Mishra, M., Ali, S.A., Sonkawade, R.G., Singh, B.P., Bhardwaj, V.N. and Prasad, R., Indian Journal of Pure & Applied Physics, 48 (2010) 486.

[18] Hussain, H.H., Hussain, R.O., Yousef, R.M. and Shamkhi, Q., J. Radioanalytical and Nuclear Chemistry, 284 (2010) 43.

[19] Michael, P., Leo, M. and Nollet, L., "Radionuclide Concentrations in Food and the Environment", 1st edition, (Taylor & Francis Group, Boca Raton, London, New York, 2007).

[20] Singh, J., Singh, H., Singh, S., Bajwa, B.S. and Sonkawade, R.G., Journal of Environmental Radioactivity, 100 (2009) 94.

[21] L'Annunziata, M., "Handbook of Radioactivity Analysis", (Elsevier Science, USA, 2003).

[22] UNSCEAR, Report to the General Assembly, with Scientific Annexes. New York, United Nations, 1 (2000) 654.

[23] UNSCEAR, "Effects of Ionizing Radiation Exposure from Natural Sources of Radiation", (New York, 2017).

[24] European Commission. Radiation Protection 112, Radiological protection principles concerning the natural radioactivity of building materials, (Brussels, European Commission, 1999).

[25] Karim, M.S., Daroysh, H.H. and Hameed, T.K., Journal of Radiation and Nuclear Applications, 1 (1) (2016) 31.

[26] Abojassim, A.A., Oleiwi, M.H. and Hassan, M., Middle-East Journal of Scientific Research, 24 (7) (2016) 2196.

[27] Oleiwi, M.H. and Rasool, W.S., Journal of Engineering and Applied Sciences, 13 (18) (2018) 7745.

[28] Kadhim, H. and Muttaleb, M.K., International Journal of Chem. Tech. Research, 9 (8) (2016) 228.

المراجع: يجب طباعة المراجع بأسطر مزدوجة ومرقمة حسب تسلسلها في النص. وتكتب المراجع في النص بين قوسين مربعين. ويتم اعتماد اختصارات الدوريات حسب نظام Wordlist of Scientific Reviewers.

الجداول: تعطى الجداول أرقاما متسلسلة يشار إليها في النص. ويجب طباعة كل جدول على صفحة منفصلة مع عنوان فوق الجدول. أما الحواشي التفسيرية، التي يشار إليها بحرف فوقي، فتكتب أسفل الجدول.

الرسوم التوضيحية: يتم ترقيم الأشكال والرسومات والرسومات البيانية (المخططات) والصور، بصورة متسلسلة كما وردت في النص.

تقبل الرسوم التوضيحية المستخرجة من الحاسوب والصور الرقمية ذات النوعية الجيدة بالأبيض والأسود، على ان تكون أصيلة وليست نسخة عنها، وكل منها على ورقة منفصلة ومعرفة برقمها بالمقابل. ويجب تزويد المجلة بالرسومات بحجمها الأصلي بحيث لا تحتاج إلى معالجة لاحقة، وألا تقل الحروف عن الحجم 8 من نوع Times New Roman، وألا تقل سماكة الخطوط عن 0.5 وبكثافة متجانسة. ويجب إزالة جميع الألوان من الرسومات ما عدا تلك التي ستنشر ملونة. وفي حالة إرسال الرسومات بصورة رقمية، يجب أن تتوافق مع متطلبات الحد الأدنى من التمايز (1200 dpi Resolution) لرسومات الأبيض والأسود الخطية، و 600 dpi للرسومات باللون الرمادي، و300 dpi للرسومات الملونة. ويجب تخزين جميع ملفات الرسومات على شكل (jpg)، وأن ترسل الرسوم التوضيحية بالحجم الفعلي الذي سيظهر في المجلة. وسواء أرسل المخطوط بالبريد أو عن طريق الشبكة (Online)، يجب أرسال نسخة ورقية أصلية ذات نوعية جيدة للرسومات التوضيحية.

مواد إضافية: تشجع المجلة الباحثين على إرفاق جميع المواد الإضافية التي يمكن أن تسهل عملية التحكيم. وتشمل المواد الإضافية أي اشتقاقات رياضية مفصلة لا تظهر في المخطوط.

المخطوط المنقح (المعدَل) والأقراص المدمجة: بعد قبول البحث للنشر وإجراء جميع التعديلات المطلوبة، فعلى الباحثين تقديم نسخة أصلية ونسخة أخرى مطابقة للأصلية مطبوعة بأسطر مزدوجة، وكذلك تقديم نسخة إلكترونية تحتوي على المخطوط كاملا مكتوبا على Microsoft Word for Windows 2000 أو ما هو استجد منه. ويجب إرفاق الأشكال الأصلية مع المخطوط النهائي المعدل حتى لو تم تقديم الأشكال إلكترونيا. وتخزن جميع ملفات الرسومات على شكل (jpg)، وتقدم جميع الرسومات التوضيحية بالحجم الحقيقي الذي ستظهر به في المجلة. ويجب إرفاق قائمة ببرامج الحاسوب التي استعملت في كتابة النص، وأسماء الملفات على قرص مدمج، حيث يعلَم القرص بالاسم الأخير للباحث، وبالرقم المرجعي للمخطوط للمراسلة، وعنوان المقالة، والتاريخ. ويحفظ في مغلف واقٍ.

حقوق الطبع

يُشَكِّل تقديم مخطوط البحث للمجلة اعترافاً صريحاً من الباحثين بأنَ مخطوط البحث لم يُنْشَر ولم يُقَدَّم للنشر لدى أي جهَة أخرى كانت وبأي صيغة ورقية أو إلكترونية أو غيرها. ويُشترط على الباحثين ملء أنموذج يَنُصُ على نقْل حقوق الطبع لتُصبح ملكاً لجامعة اليرموك قبل الموافقة على نشر المخطوط. ويقوم رئيس التحرير بتزويد الباحثين بإنموذج نقل حقوق الطبع مع النسخة المُرْسَلَة للتنقيح. كما ويُمنع إعادة إنتاج أيِّ جزء من الأعمال المنشورة في المجلّة من دون إذن خَطِّيٍّ مُسبَق من رئيس التحرير.

إخلاء المسؤولية

إن ما ورد في هذه المجلة يعبر عن آراء المؤلفين، ولا يعكس بالضرورة آراء هيئة التحرير أو الجامعة أو سياسة اللجنة العليا للبحث العلمي أو وزارة التعليم العالي والبحث العلمي. ولا يتحمل ناشر المجلة أي تبعات مادية أو معنوية أو مسؤوليات عن استعمال المعلومات المنشورة في المجلة أو سوء استعمالها.

الفهرسة: المجلة مفهرسة في:

Scopus	ULRICHSWEB™ GLOBAL SERIALS DIRECTORY

معلومات عامة

المجلة الأردنية للفيزياء هي مجلة بحوث علميّة عالمية متخصصة مُحكمة تصدر بدعم من صندوق دعم البحث العلمي، وزارة التعليم العالي والبحث العلمي، عمان، الأردن. وتقوم بنشر المجلة عمادة البحث العلمي والدراسات العليا في جامعة اليرموك، إربد، الأردن. وتنشر البحوث العلمية الأصيلة، إضافة إلى المراسلات القصيرة Short Communications، والملاحظات الفنية Technical Notes، والمقالات الخاصّة Feature Articles، ومقالات المراجعة Review Articles، في مجالات الفيزياء النظرية والتجريبية، باللغتين العربية والإنجليزية.

تقديم مخطوط البحث

تقدم البحوث عن طريق إرسالها إلى البريد الإلكتروني : jjp@yu.edu.jo

تقديم المخطوطات إلكترونيًا: اتبع التعليمات في موقع المجلة على الشبكة العنكبوتية.

ويجري تحكيمُ البحوثِ الأصيلة والمراسلات القصيرة والملاحظات الفنية من جانب مُحكِّمين اثنين في الأقل من ذوي الاختصاص والخبرة. وتُشَجِّع المجلة الباحثين على اقتراح أسماء المحكمين. أما نشر المقالات الخاصّة في المجالات الفيزيائية النَشِطَة، فيتم بدعوة من هيئة التحرير، ويُشار إليها كذلك عند النشر. ويُطْلَب من كاتب المقال الخاص تقديم تقرير واضح يتّسم بالدقة والإيجاز عن مجال البحث تمهيداً للمقال. وتنشر المجلةُ أيضاً مقالات المراجعة في الحقول الفيزيائية النشطة سريعة التغيُر، وتُشَجَع كاتبي مقالات المراجعة أو مُستَكتبيها على إرسال مقترحٍ من صفحتين إلى رئيس التحرير. ويُرفَق مع البحث المكتوب باللغة العربية ملخص (Abstract) وكلمات دالة (Keywords) باللغة الإنجليزية.

ترتيب مخطوط البحث

يجب أن تتم طباعة مخطوط البحث ببنط 12 نوعه Times New Roman، وبسطر مزدوج، على وجه واحد من ورق A4 (21.6 × 27.9 سم) مع حواشي 3.71 سم ، باستخدام معالج كلمات ميكروسوفت وورد 2000 أو ما اسْتَجَد منه. ويجري تنظيم أجزاء المخطوط وفق الترتيب التالي: صفحة العنوان، الملخص، رموز التصنيف (PACS)، المقدّمة، طرق البحث، النتائج، المناقشة، الخلاصة، الشكر والعرفان، المراجع، الجداول، قائمة بدليل الأشكال والصور والإيضاحات، ثَمَّ الأشكال والصور والإيضاحات. وتُكْتَب العناوين الرئيسة بخطٍ **غامق**، بينما تُكْتَب العناوين الفرعية بخطٍ *مائل*.

صفحة العنوان: وتشمل عنوان المقالة، أسماء الباحثين الكاملة وعناوين العمل كاملة. ويكتب الباحث المسؤول عن المراسلات اسمه مشارا إليه بنجمة، والبريد الإلكتروني الخاص به. ويجب أن يكون عنوان المقالة موجزا وواضحا ومعبرا عن فحوى (محتوى) المخطوط، وذلك لأهمية هذا العنوان لأغراض استرجاع المعلومات.

الملخص: المطلوب كتابة فقرة واحدة لا تزيد على مائتي كلمة، موضحة هدف البحث، والمنهج المتبع فيه والنتائج وأهم ما توصل إليه الباحثون.

الكلمات الدالة: يجب أن يلي الملخص قائمة من 4-6 كلمات دالة تعبر عن المحتوى الدقيق للمخطوط لأغراض الفهرسة.

PACS: يجب إرفاق الرموز التصنيفية، وهي متوافرة في الموقع http://www.aip.org/pacs/pacs06/pacs06-toc.html.

المقدمة: يجب أن توضّح الهدف من الدراسة وعلاقتها بالأعمال السابقة في المجال، لا أن تكون مراجعة مكثفة لما نشر (لا تزيد المقدمة عن صفحة ونصف الصفحة مطبوعة).

طرائق البحث (التجريبية / النظرية): يجب أن تكون هذه الطرائق موضحة بتفصيل كاف لإتاحة إعادة إجرائها بكفاءة، ولكن باختصار مناسب، حتى لا تكون تكرارا للطرائق المنشورة سابقا.

النتائج: يستحسن عرض النتائج على صورة جداول وأشكال حيثما أمكن، مع شرح قليل في النص ومن دون مناقشة تفصيلية.

المناقشة: يجب أن تكون موجزة وتركز على تفسير النتائج.

الاستنتاج: يجب أن يكون وصفا موجزا لأهم ما توصلت إليه الدراسة ولا يزيد عن صفحة مطبوعة واحدة.

الشكر والعرفان: الشكر والإشارة إلى مصدر المنح والدعم المالي يكتبان في فقرة واحدة تسبق المراجع مباشرة.

Subscription Form

Jordan Journal of

PHYSICS

An International Peer-Reviewed Research Journal issued by the Support of the Scientific Research Support Fund

Published by the Deanship of Research & Graduate Studies, Yarmouk University, Irbid, Jordan

Name: .... الأسم:
Specialty:...التخصص:
Address: ....العنوان:
P.O. Box:.. صندوق البريد:
City & Postal Code: .... المدينة/الرمز البريدي:
Country: ....الدولة:
Phone: ....رقم الهاتف:
Fax No:.. رقم الفاكس:
E-mail:.. البريد الإلكتروني:
No. of Subscription: .... عدد الإشتراكات:
Method of Payment:.. طريقة الدفع:
Amount Enclosed:.. المبلغ المرفق:
Signature: ....التوقيع:

Cheques should be paid to Deanship of Research and Graduate Studies - Yarmouk University.

I would like to subscribe to the Journal
For

- ☐ One Year
- ☐ Two Years
- ☐ Three Years

One Year Subscription Rates

	Inside Jordan	Outside Jordan
Individuals	JD 8	€ 40
Students	JD 4	€ 20
Institutions	JD 12	€ 60

Correspondence

Subscriptions and Sales:

Prof. Ibrahim O. Abu Al-Jarayesh
Deanship of Research and Graduate Studies
Yarmouk University
Irbid – Jordan
Telephone: 00 962 2 711111 Ext. 2075
Fax No.: 00 962 2 7211121

المملكة الأردنية الهاشمية

جامعة اليرموك

المجلة الأردنية

للفيزياء

مجلة بحوث علمية عالمية متخصصة محكّمة

تصدر بدعم من صندوق دعم البحث العلمي

المجلد (14)، العدد (3)، أيلول 2021م / صفر 1443هـ

المجلة الأردنية

للفيزياء

مجلة بحوث علمية عالمية محكّمة

المجلد (14)، العدد (3)، أيلول 2021م / صفر 1443هـ

المجلة الأردنية للفيزياء: مجلة علمية عالمية متخصصة محكّمة تصدر بدعم من صندوق دعم البحث العلمي، عمان، الأردن، وتصدر عن عمادة البحث العلمي والدراسات العليا، جامعة اليرموك، إربد، الأردن.

ترسل البحوث إلى العنوان التالي:

الأستاذ الدكتور إبراهيم عثمان أبو الجرايش
رئيس تحرير المجلة الأردنية للفيزياء
عمادة البحث العلمي والدراسات العليا، جامعة اليرموك
إربد ، الأردن
هاتف 7211111 2 962 00 **فرعي** 2075
E-mail: *jjp@yu.edu.jo* **Website**: *http://Journals.yu.edu.jo/jjp*